

doi:10.14379/iodp.proc.353.102.2016

Expedition 353 methods¹



S.C. Clemens, W. Kuhnt, L.J. LeVay, P. Anand, T. Ando, M. Bartol, C.T. Bolton, X. Ding, K. Gariboldi, L. Giosan, E.C. Hathorne, Y. Huang, P. Jaiswal, S. Kim, J.B. Kirkpatrick, K. Littler, G. Marino, P. Martinez, D. Naik, A. Peketi, S.C. Phillips, M.M. Robinson, O.E. Romero, N. Sagar, K.B. Taladay, S.N. Taylor, K. Thirumalai, G. Uramoto, Y. Usui, J. Wang, M. Yamamoto, and L. Zhou²

Keywords: International Ocean Discovery Program, IODP, Expedition 353, *JOIDES Resolution*, Site U1443, Site U1444, Site U1445, Site U1446, Site U1447, Site U1448, Indian monsoon, monsoon, Bay of Bengal, Andaman Sea, paleoclimate, paleoceanography, Miocene, Pliocene, Pleistocene, Holocene, Cretaceous, Paleogene, Ninetyeast Ridge, Indian Ocean, salinity, Bengal Fan, orbital, millennial, centennial, abrupt climate change

Contents

- 1 Introduction
- 1 Operations
- 3 Lithostratigraphy
- 7 Biostratigraphy
- 24 Geochemistry
- 27 Paleomagnetism
- 30 Physical properties
- 32 Downhole logging
- 37 Stratigraphic correlation
- 38 References

Introduction

This chapter documents the procedures and methods employed in the various shipboard laboratories of the R/V *JOIDES Resolution* during International Ocean Discovery Program (IODP) Expedition 353. This information applies only to shipboard work described in the Expedition Reports section of the Expedition 353 *Proceedings of the International Ocean Discovery Program* volume. Methods used by investigators for shore-based analyses of Expedition 353 data will be described in separate individual publications.

Authorship of the site chapters

All shipboard scientists contributed to this volume. However, certain sections were written by discipline-based groups of scientists as listed below (authors are listed in alphabetical order; no seniority is implied):

Background and objectives: S. Clemens, W. Kuhnt
Operations: K. Grigar, L. LeVay
Lithostratigraphy: T. Ando, S. Kim, K. Littler, P. Martinez, D.K. Naik, S. Phillips, K. Thirumalai, G. Uramoto, L. Zhou
Biostratigraphy: M. Bartol, C. Bolton, X. Ding, K. Gariboldi, M. Robinson, O. Romero
Geochemistry: E. Hathorne, Y. Huang, J. Kirkpatrick, A. Peketi, N. Sagar, M. Yamamoto
Paleomagnetism: S. Taylor, Y. Usui
Physical properties: P. Anand, P. Jaiswal, K. Taladay, J. Wang
Downhole logging: P. Jaiswal, K. Taladay
Stratigraphic correlation: L. Giosan, G. Marino

Operations

Site locations

GPS coordinates from precruise site surveys were used to position the vessel at all IODP Expedition 353 sites. A Syquest Bathy 2010 CHIRP subbottom profiler was used to monitor the seafloor depth on the approach to each site to reconfirm the depth profiles from precruise surveys. Once the vessel was positioned at a site, the thrusters were lowered and a positioning beacon was dropped to the seafloor. The dynamic positioning control of the vessel used navigational input from the GPS system and triangulation to the seafloor beacon, weighted by the estimated positional accuracy. The final position for each hole of a given site was the mean position calculated from the GPS data collected over a significant portion of the time that the hole was occupied.

Coring and drilling operations

The advanced piston corer (APC), half-length advanced piston corer (HLAPC), and extended core barrel (XCB) systems were used during Expedition 353. At IODP Sites U1443 and U1445–U1448, multiple holes were drilled to build a composite depth scale and a stratigraphic splice for continuous subsampling after the cruise (see [Sample depth calculations](#) and [Stratigraphic correlation](#)).

The APC and HLAPC cut soft-sediment cores with minimal coring disturbance relative to other IODP coring systems. After the APC core barrel is lowered through the drill pipe and lands near the bit, the drill pipe is pressured up until two shear pins that hold the inner barrel attached to the outer barrel fail. The inner barrel then advances into the formation and cuts the core. The driller can de-

¹ Clemens, S.C., Kuhnt, W., LeVay, L.J., Anand, P., Ando, T., Bartol, M., Bolton, C.T., Ding, X., Gariboldi, K., Giosan, L., Hathorne, E.C., Huang, Y., Jaiswal, P., Kim, S., Kirkpatrick, J.B., Littler, K., Marino, G., Martinez, P., Naik, D., Peketi, A., Phillips, S.C., Robinson, M.M., Romero, O.E., Sagar, N., Taladay, K.B., Taylor, S.N., Thirumalai, K., Uramoto, G., Usui, Y., Wang, J., Yamamoto, M., and Zhou, L., 2016. Expedition 353 methods. In Clemens, S.C., Kuhnt, W., LeVay, L.J., and the Expedition 353 Scientists, *Indian Monsoon Rainfall*. Proceedings of the International Ocean Discovery Program, 353. College Station, TX (International Ocean Discovery Program). <http://dx.doi.org/10.14379/iodp.proc.353.102.2016>

² [Expedition 353 Scientists' addresses](#).

tect a successful cut, or “full stroke,” from the pressure gauge on the rig floor.

The depth limit of the APC, often referred to as APC refusal, is indicated in two ways: (1) the piston consistently fails to achieve a complete stroke (as determined from the pump pressure reading) because the formation is too hard and limited core recovery is achieved, or (2) excessive force (>60,000 lb; ~267 kN) is required to pull the core barrel out of the formation. When a full stroke could not be achieved, one or more additional attempts were typically made, and each time the bit was advanced by the length of recovered core. Note that this resulted in a nominal recovery of ~100% based on the assumption that the barrel penetrated the formation by the length of core recovered. During Expedition 353, there were a number of partial strokes that still returned nearly full core liners. In these cases, the partial strokes were not viewed as refusal and additional APC cores were attempted. When a full or partial stroke was achieved but excessive force could not retrieve the barrel, the core barrel was sometimes “drilled over,” meaning that after the inner core barrel was successfully shot into the formation the drill bit was advanced to total depth to free the APC barrel.

The standard APC system contains a 9.5 m long core barrel, and the HLAPC system uses a 4.7 m long core barrel. In most instances, the HLAPC was deployed after the standard APC reached refusal. During use of the HLAPC, the same criteria were applied in terms of refusal as for the full-length APC system. Use of the HLAPC allowed for significantly greater APC sampling depths to be attained than would have otherwise been possible without the existence of this system.

Nonmagnetic core barrels were used during most of the full-length APC deployments, and steel core barrels were used for the HLAPC system. Orientation using the FlexIT tool or Icefield MI-5 tool (see [Paleomagnetism](#)) was used on standard APC cores taken from selected holes at each site. Formation temperature measurements were made to obtain temperature gradients and heat flow estimates using the third-generation advanced piston corer temperature tool (APCT-3) (see [Physical properties](#)).

The XCB system was used to advance the hole when HLAPC refusal occurred before the target depth was reached. The XCB is a rotary system with a small cutting shoe that extends below the large rotary APC/XCB bit. The smaller bit can cut a semi-indurated core with less torque and fluid circulation than the main bit, optimizing recovery. The XCB cutting shoe (bit) extends ~30.5 cm ahead of the main bit in soft sediments but retracts into the main bit when hard formations are encountered. XCB core barrels are 9.5 m long. During Expedition 353 (Site U1445), the XCB was used with 8 m advances to allow extra accommodation space within the core liners in intervals where gas expansion was strong, which significantly reduced the loss of sediment out the top of the barrel while on the rig floor prior to extracting the core liner.

The bottom-hole assembly (BHA) is the lowermost part of the drill string. A typical APC/XCB BHA consists of a drill bit (outer diameter [OD] = 11¹/₁₆ inch), a bit sub, a seal bore drill collar, a landing saver sub, a modified top sub, a modified head sub, a nonmagnetic drill collar (for APC/XCB), a number of 8¹/₄ inch (~20.32 cm) drill collars, a tapered drill collar, six joints (two stands) of 5¹/₂ inch (~13.97 cm) drill pipe, and one crossover sub. A lockable flapper valve was used so that we could collect downhole logs without dropping the bit during APC/XCB coring.

Drilling disturbance

Cores may be significantly disturbed as a result of the drilling process and contain extraneous material as a result of the coring

and core handling process. The uppermost 10–50 cm of each core must therefore be examined critically during description for potential “cave-in.” Common coring-induced deformation includes the concave-downward appearance of originally horizontal bedding. Piston action may result in fluidization (flow-in) at the bottom of APC cores. Retrieval from depth to the surface may result in elastic rebound. Gas that is in solution at depth may become free and drive core segments within the liner apart. When gas content is high, pressure must be relieved for safety reasons before the cores are cut into segments. This is accomplished by drilling holes into the liner, which forces some sediment as well as gas out of the liner. Drilling disturbances are described in the Lithostratigraphy sections in each site chapter and are graphically indicated on the graphic core summary reports.

Core handling and curatorial procedures

Cores recovered during Expedition 353 were extracted from the core barrel in plastic liners. These liners were carried from the rig floor to the core processing area on the catwalk outside the Core Laboratory and cut into ~1.5 m long sections. The exact section length was noted and later entered into the database as “created length” using the Sample Master application. This number was used to calculate recovery. Headspace samples were taken from selected section ends (typically one per core) using a syringe for immediate hydrocarbon analysis as part of the shipboard safety and pollution prevention program. Similarly, void space gas and microbiology samples were taken immediately after the core was sectioned. Whole-round samples for interstitial water, physical properties, and gas hydrates were cut on the catwalk. Core catcher samples were taken for biostratigraphic analysis. When catwalk sampling was complete, liner caps (blue = top; colorless = bottom; yellow = bottom, whole-round cut) were glued with acetone onto liner sections and the sections were placed in core racks in the laboratory for analysis.

The numbering of sites, holes, cores, and samples followed standard IODP procedure. A full curatorial sample identifier consists of the following information: expedition, site, hole, core number, core type, section number, and offset in centimeters measured from the top of a given section. For example, a sample identification of “353-U1443A-1H-2, 10–12 cm” represents a sample taken from the interval between 10 and 12 cm below the top of Section 2 of Core 1 (“H” designates that this core was taken with the APC system) of Hole A of Site U1443 during Expedition 353. The “U” preceding the hole number indicates that the hole was drilled by the *JOIDES Resolution*. Other core types are designated by “F” for cores taken with the HLAPC system and “X” for cores taken by the XCB system.

Shipboard core analysis

Whole-round core sections were immediately run through the Special Task Multisensor Logger (STMSL), also called the “fast track,” or the Whole-Round Multisensor Logger (WRMSL) after being cut on the catwalk. The STMSL measures density and magnetic susceptibility (MS) and the WRMSL measures *P*-wave velocity, density, and MS. Whole-round core sections were also run on the Natural Gamma Radiation Logger (NGRL). For Holes B and/or C at each site, the core sections were run alternatively on the WRMSL and STMSL to produce core data more quickly for stratigraphic correlation (see [Physical properties](#)).

Core sections were run immediately through the WRMSL and STMSL. Core sections were allowed to reach equilibrium with laboratory temperature (after ~4 h) prior to running through the NGRL. Each section from a given core was split lengthwise from bottom to

top into working (W) and archive (A) halves. Investigators should note that older material might have been transported upward on the split face of each section during splitting. The working half of each section was sampled for shipboard analysis (biostratigraphy, paleomagnetism, physical properties, geochemistry, and bulk X-ray diffraction [XRD] mineralogy). The archive half of each section for each core was scanned on the Section Half Imaging Logger (SHIL) and measured for color reflectance and MS on the Section Half Multisensor Logger (SHMSL). At the same time, the archive halves were described macroscopically as well as microscopically by means of smear slides. Finally, the archive halves were run through the cryogenic magnetometer. Both halves of the core were then put into labeled plastic tubes that were sealed and transferred to cold storage space aboard the ship.

At the end of the expedition, all archive and working section halves were transported from the ship to permanent cold storage at the Kochi Core Center in Kochi, Japan.

Sample depth calculations

The primary depth scale types are based on the measurement of the drill string length deployed beneath the rig floor (drilling depth below rig floor [DRF] and drilling depth below seafloor [DSF]), the length of each core recovered (core depth below seafloor [CSF] and core composite depth below seafloor [CCSF]), and the length of the logging wireline deployed (wireline log depth below rig floor [WRF], wireline log depth below seafloor [WSF], and wireline log matched depth below seafloor [WMSF]). All units are in meters. Depths of samples and measurements are calculated at the applicable depth scale either by fixed protocol (e.g., CSF) or by combinations of protocols with user-defined correlations (e.g., CCSF). The user should be aware that the definition of these depth scale types, and the distinction in nomenclature, mean that a nominal depth value at two different depth scale types usually does not refer to exactly the same stratigraphic interval in a hole.

Depths of cored intervals are measured from the drill floor based on the length of drill pipe deployed beneath the rig floor (DRF scale). The depth of the cored interval is referenced to the seafloor (DSF scale) by subtracting the seafloor depth at the time of the first hole from the DRF depth of the interval. In most cases, the seafloor depth is the length of pipe deployed minus the length of the mudline core recovered.

Standard depths of cores in meters below the seafloor (CSF-A scale) are determined based on the assumption that (1) the top depth of a recovered core corresponds to the top depth of its cored interval (at DSF scale) and (2) the recovered material is a contiguous section even if core segments are separated by voids when recovered. Voids in the core are closed by pushing core segments together, if possible, during core handling. This convention is also applied if a core has incomplete recovery, in which case the true position of the core within the cored interval is unknown and should be considered a sample depth uncertainty, up to the length of the core barrel used, when analyzing data associated with the core material. Standard depths of samples and associated measurements (CSF-A scale) are calculated by adding the offset of the sample or measurement from the top of its section, and the lengths of all higher sections in the core, to the top depth of the cored interval.

A soft to semisoft sediment core from less than a few hundred meters below seafloor expands upon recovery (typically a few percent to as much as 15%), so the length of the recovered core exceeds that of the cored interval. Therefore, a stratigraphic interval may not have the same nominal depth at the DSF and CSF scales in the

same hole. When core recovery (the ratio of recovered core to cored interval times 100%) is >100%, the CSF depth of a sample taken from the bottom of a core will be deeper than that of a sample from the top of the subsequent core (i.e., the data associated with the two core intervals overlap at the CSF-A scale).

Core composite depth scales (CCSF) are constructed for sites, whenever feasible, to mitigate the CSF-A core overlap and coring gap problems and to create as continuous a stratigraphic record as possible. Using shipboard core logger-based physical property data, verified with core photos, core depths in adjacent holes at a site are vertically shifted to correlate between cores recovered in adjacent holes. This process produces the CCSF-A depth scale. The correlation process results in affine tables, indicating the vertical shift of cores at the CCSF scale relative to the CSF-A scale. Once the CCSF scale is constructed, a splice can be defined that best represents the stratigraphy of a site by utilizing and splicing the best portions of individual sections and cores from each hole at a site. This process produces the CCSF-D depth scale, which is strictly correct only along the splice. For detailed depth scale definitions, see [Stratigraphic correlation](#).

Lithostratigraphy

The Expedition 353 sedimentologists determined the lithostratigraphy of sediments using the following tools: visual core descriptions (VCDs), smear slide and thin section analyses, digital color imaging, and visual color determination. The methods used were adapted from those used during Integrated Ocean Drilling Program Expedition 342 (Norris, Wilson, Blum, and the Expedition 342 Scientists, 2014).

Digital color image

The SHIL imaged the flat face of the archive half of split cores using a line-scan camera. Prior to imaging, and when necessary, the core face was prepared by scraping across, rather than along, the core section using a stainless steel or glass scraper. Scraping parallel to bedding with a freshly cleaned tool prevented cross-stratigraphic contamination. Post splitting, the archive halves were imaged as soon as possible to capture the core surface prior to drying and/or oxidation. Images were scanned at an interval of 10 lines/mm, with camera height allowing for square pixels. The imaging light was provided by three pairs of advanced illumination high-current-focused LED line lights with fully adjustable angles to the lens axis. Compression of line-scanned images on VCDs or summary figures may result in visual artefacts, primarily lamination that is not present in the actual sections. Red, green, and blue (RGB) data were also generated using the SHIL and used as a primary tool for stratigraphic correlation.

Spectrophotometry and visual color determination

After imaging, spectrophotometry and MS were measured on the archive halves with the SHMSL. Spurious measurements may occur from small cracks, drilling disturbance, or plastic section dividers. These data were further degraded by the inability of the instrument to consistently land the sensors flatly on the core surface, resulting in the leakage of ambient room light into the spectrophotometer readings and reduced MS values. Additional details regarding measurement and interpretation of spectral data can be found in Balsam et al. (1997, 1998), Balsam and Damuth (2000), and Giosan et al. (2002).

Reflectance of visible light from the archive halves of sediment cores was measured using an Ocean Optics USB4000 spectrophotometer mounted on the automated SHMSL. Freshly split cores were covered with clear plastic wrap (Glad Wrap) and placed on the SHMSL. Measurements were taken at 2.5 cm spacing to provide a high-resolution stratigraphic record of color variation for visible wavelengths. Each measurement was recorded in 2 nm wide spectral bands from 400 to 900 nm.

In addition to the digital color image captured by the SHIL, VCDs include a description of sediment color and the corresponding hue, value, and chroma data as determined qualitatively using Munsell soil color charts for each major and minor lithology (Munsell Color Company, 1994).

MS was measured with a Bartington Instruments MS2E point sensor (high-resolution surface scanning sensor) on discrete points along the SHMSL track. Measurements were taken at the same spacing as the reflectance measurements, integrating a volume of 10.5 mm × 3.8 mm × 4 mm, where 10.5 mm is the length perpendicular to the core axis, 3.8 mm is the width in the core axis, and 4 mm is the depth. For conversion of the instrument units stored in the IODP database, a correction factor (67/80) must be employed to correct for the relation of the sensor diameter and sediment thickness.

Visual core descriptions

VCDs of the archive halves provide a visual summary of lithostratigraphic, biostratigraphic, magnetostratigraphic, and physical property data obtained during shipboard analyses, similar to the “barrel sheets” used during the Deep Sea Drilling Project (DSDP), Ocean Drilling Program (ODP), and Integrated Ocean Drilling Program. Lithostratigraphic data for VCDs were entered digitally during description using the DESClogik software (version 8.0.0.0). A spreadsheet template with four tabs was customized for Expedition 353, recording the following information:

- Sedimentological core description,
- Drilling disturbance,
- Core summary (written description of major lithologic information by core), and
- Smear slide description.

DESClogik also includes a graphic display mode of digital images of section halves and physical property data to aid core description.

Volcanic ash abundance in the visual description was characterized with the following categories:

Absent
Trace (<10%)
Moderate (11%–50%)
Common (51%–90%)
Abundant (>90%)

During Expedition 353, the Strater software package was used to compile the VCDs for each core. Site, hole, core number, and a core description summary are provided at the top of the VCD sheet (Figure F1). The written description for each core contains a concise summary of major and minor lithologies, Munsell colors, sedimentary structures, and drilling disturbances resulting from the coring process (Figure F2). Core depth (in meters CSF-A), core length, section breaks, and lithostratigraphic units are indicated along the left side of the digital color image of the core and Graphic lithology column. Columns to the right of the Graphic lithology column include

Drilling disturbance and intensity, Sedimentary structures, Lithologic accessories, Shipboard sampling, and Age. Additional columns show data collected by the WRMSL and SHMSL (see **Physical properties**) that includes gamma ray attenuation (GRA), MS, natural gamma radiation (NGR), and lightness (L^*) and color (a^* and b^*) from color reflectance.

Sediment classification

Lithologic names consist of a principal name based on composition, degree of lithification, and/or texture as determined from visual examination of the cores and smear slide or thin section observations. For a mixture of components, the principal name is preceded by major modifiers (in order of increasing abundance) that refer to components making up ≥25% of the sediment. Minor components that represent between 10% and 25% of the sediment follow the principal name in order of increasing abundance. For example, an unconsolidated sediment containing 40% nannofossils, 35% clay minerals, 15% foraminifers, and 10% diatoms would be described as a clayey nannofossil ooze with foraminifers and diatoms. Naming conventions roughly follow the ODP sediment classification scheme of Mazzullo et al. (1988); however, the mixed sediment class is replaced by a more descriptive set of terms (Figure F3).

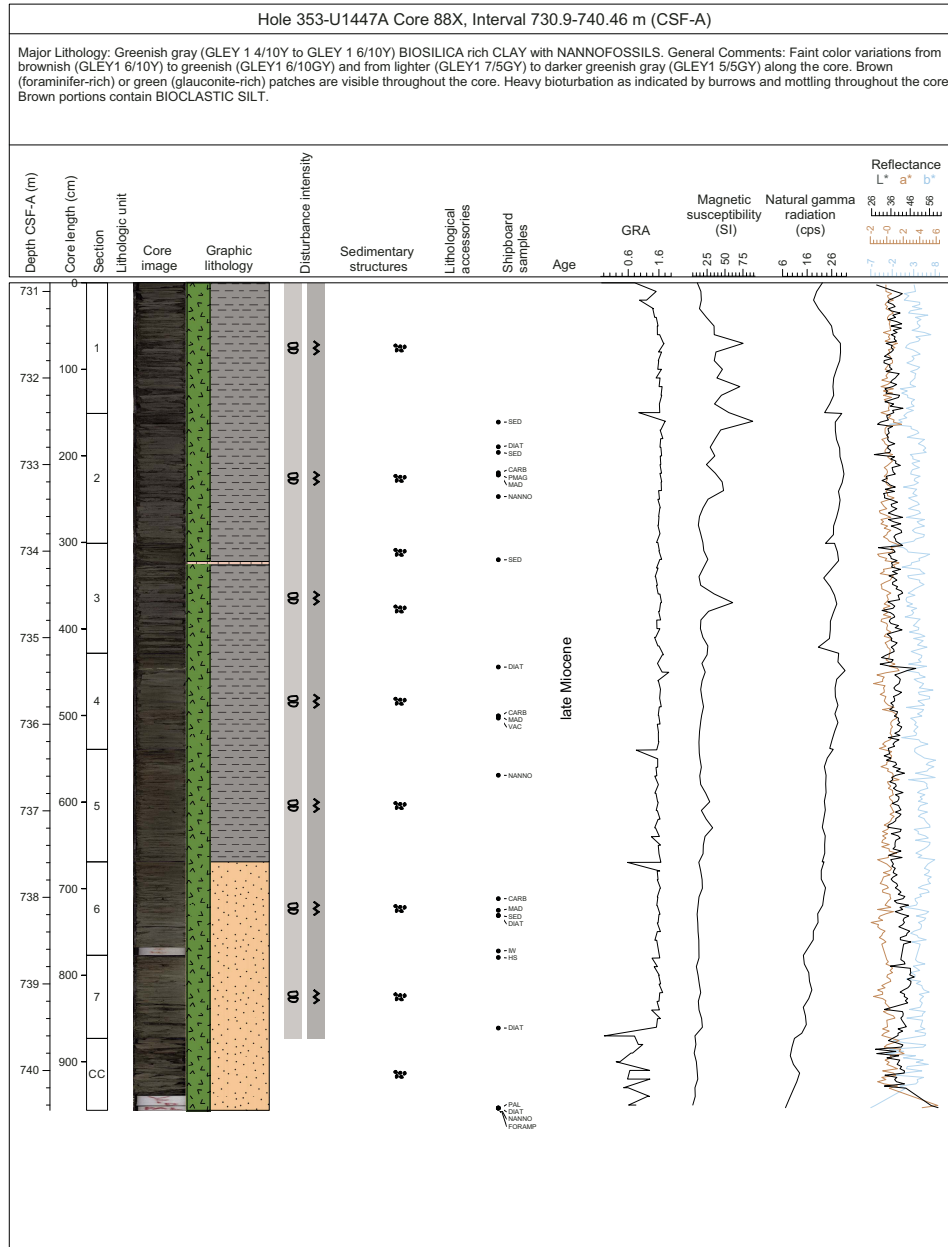
Sediments were divided into lithostratigraphic units on the basis of visual core descriptions, smear slides, thin sections (where sediment was sufficiently lithified), physical property data (see **Physical properties**), shipboard measurements of inorganic carbon content (see **Geochemistry**), and shipboard XRD analyses. The grain size scale used in descriptions is from Wentworth (1922).

Description of lithification is dependent on the dominant composition:

- Sediments derived predominantly from calcareous pelagic organisms (e.g., calcareous nannofossils and foraminifers): the lithification terms “ooze,” “chalk,” and “limestone” reflect whether the sediment can be deformed with a finger (ooze), can be scratched easily by a fingernail (chalk), or cannot be scratched with a fingernail (limestone).
- Sediments derived predominantly from siliceous microfossils (e.g., diatoms): the lithification terms “ooze,” “diatomite,” “porcellanite,” and “chert” reflect whether the sediment can be deformed with a finger (ooze), cannot be easily deformed manually (diatomite), or displays a glassy luster (chert). We use the term “porcellanite” as defined by Keene (1975) to describe a siliceous limestone/claystone that has a dull luster and is less hard and compact than chert. Porcellanite may contain a mix of opal, quartz, clay minerals, and carbonate. Note that the terms “porcellanite” and “chert” do not imply crystallinity of the silica.
- Sediments derived predominantly from siliciclastic material: if the sediment can be deformed easily with a finger, no lithification term is added and the sediment is named for the dominant grain size. For more consolidated material, the lithification suffix “-stone” is appended to the dominant size classification (e.g., “clay” versus “claystone”).
- Consolidated sediments derived from an approximately equal mix of calcareous and fine siliciclastic material were described as “marlstone.”

Each recovered lithology is shown in the Graphic lithology column on the VCD sheet (Figure F1). For intervals composed of more than one lithology, symbols are arranged within the column from left to right in order of their relative abundance. Graphic lithologies are used for all components that comprise 25% or more of the total

Figure F1. Example of graphic VCD summarizing data from macroscopic description, smear slide, core imaging, and physical property measurements. cps = counts per second.



sediment. The width of each pattern in the column approximates the relative abundance of that component. For instance, a “clay nannofossil ooze with foraminifers” would be depicted as the thinner left half of the column showing the “clay” graphic lithology and the thicker right half of the column showing the “nannofossil ooze” graphic lithology.

Sedimentary structures

Sedimentary structures formed by physical and biological processes are represented on the VCD sheet with symbols in the Sedimentary structures column (Figure F2).

When identifiable, ichnofossils such as *Zoophycos* or *Chondrites* burrows were reported in the lithologic description. Sedimentary structure types are indicated on the right side of the Structures col-

umn. All contacts between lithologies are gradational and horizontal unless otherwise specified. All lithology intervals are nongraded unless otherwise specified. Bed thickness is equal to the thickness of the lithology interval unless laminations, turbidites, etc., are observed. Bedding and lamination thickness is classified as

- <0.1 cm = very thin lamination,
- 0.1–0.3 cm = thin lamination,
- >0.3–0.6 cm = medium lamination,
- >0.6–1 cm = thick lamination,
- >1–3 cm = very thin bed,
- >3–10 cm = thin bed,
- >10–30 cm = medium bed,
- >30–100 cm = thick bed,
- >100 cm = very thick bed.

Figure F2. Symbols used for visual core description.

Lithology		
	Clay	
	Sand	
	Silt	
	Volcanic ash	
	Marlstone	
	Nannofossil ooze	
	Nannofossil chalk	
	Calcareous ooze	
	Diatom ooze	
	Bioclastic	

Sedimentary structures	Other sedimentary features
Gas hydrate	Climbing ripple cross stratification
Cross bedding	Wavy strata/Laminations
Interstratification/Parallel lamination	Bigradational bedding
Color banding	Lens/Pod/Patch/Bleb
Tilted bedding	Mud drape
Lenticular bedding/Flaser bedding	Normal grading/Fining upward
Grain orientation layering/Imbrication	Inverse grading/Coarsening upward
Slump fold	Mottling
Burrows	Sharp contact
Curved boundary	
	Sole marks/Flute clast/Tool mark/Bottom cast/Load cast
	Wave ripples
	Liquefaction/Pipe and dish/Fluid escape structures
	Ball and pillow
	Current ripple mark/Ripple
	Convolute bedding
	Flame structure

Lithologic accessories
Shell fragments/Other macrofossils
Cement
Nodule/Concretion

Drilling disturbances
Slightly disturbed
Moderately disturbed
Highly/Severely disturbed
Destroyed
Void
Soupy
Mousselike
Horizontal cracks
Fragmented
Fractured
Biscuit
Fall-in
Gas expansion

Shipboard sampling		
SS Smear slide	MBIO Microbiology	IW Interstitial water
CARB Carbonate	PAL Micropaleontology	IWs Interstitial water, syringe
XRD X-ray diffraction	NANNO Nannofossil	PMAG Paleomagnetic
SED Sedimentology	DIAT Diatom	TS Thin section
HS Headspace	MAD Moisture/Density	

Deposits with scoured bases and normal grading were described as turbidites. If possible, turbidites were classified using Bouma or Stow models (Bouma, 1962; Stow, 1977). Medium-grained Bouma sequences (clay to sand) are noted in some cases by a code (see Shipboard Scientific Party, 1995) that consists of an uppercase T followed by lowercase letters that summarize the order and identity of internal divisions within the Bouma sequence:

- a = massive or graded division.
- b = parallel laminated sand or silt division.
- c = ripple cross-laminated division.
- d = silt parallel laminated division.
- e = essentially homogeneous mud division, possibly graded.

Fine-grained Stowe sequences (clay to silt) can consist of the following:

- T0 = basal lenticular lamination.
- T1 = convolute laminations.
- T2 = wavy lenticular laminations.

- T3 = thin parallel lamination.
- T4 = indistinct laminations.
- T5 = wispy silt laminations.
- T6 = graded clay-silt lenses.
- T7 = ungraded clay.
- T8 = bioturbated clay.

Drilling disturbance

Sediment disturbance resulting from the coring process is illustrated in the Disturbance intensity column on the VCD sheet (e.g., fall-in, flow-in, and biscuits) (Figure F1). If the feature extends over an interval, the symbol appears centered on a vertical line to denote the extent of occurrence. Blank regions indicate an absence of drilling disturbance. Disturbance intensity follows the following subjective scheme:

- Slight
- Moderate
- Severe
- Destroyed

Sediment disturbance resulting from dissociation of gas hydrates is described on the VCDs as having mousselike or soupy textures (Shipboard Scientific Party, 2003).

Age

The age of the sediments, as determined from integrated biostratigraphic and paleomagnetic data, is displayed in the Age column in the VCDs (see [Biostratigraphy](#) and [Paleomagnetism](#)). These data are presented for Hole A at each site only; age information for additional holes should be taken by comparing the spliced depths to Hole A (see [Stratigraphic correlation](#)).

Smear slide descriptions

Smear slide samples were taken by toothpick sampling of the archive halves to define the lithologies. Visual percentage estimates of lithogenic, biogenic, and authigenic minerals, as well as grain size estimates (clay, silt, and sand) were made from each slide. Biogenic components were divided into major microfossil groups (e.g., nannofossils, diatoms, foraminifers, and radiolarians). Basic mineralogies were identified, (e.g., quartz, feldspar, clay, and mica). Authigenic minerals (e.g., carbonates, iron sulfides, and glauconite) were also identified.

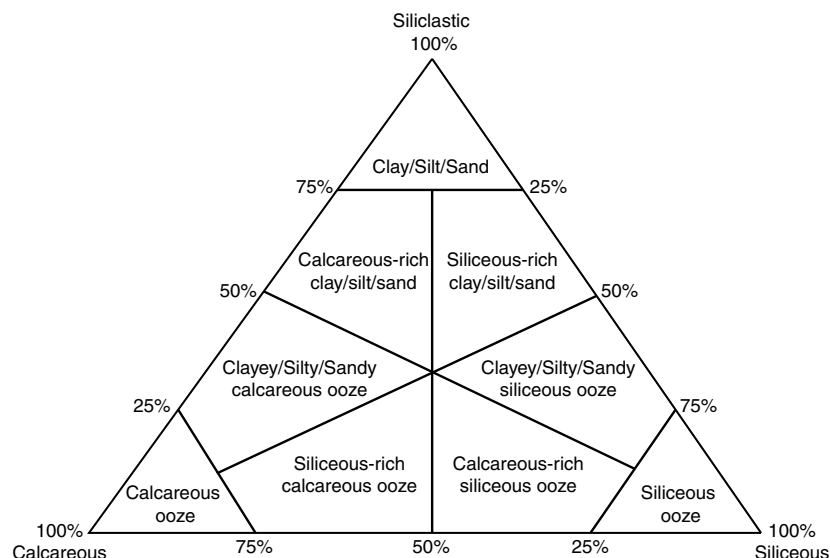
Components observed in the smear slides were quantified using the following categories:

- 0 = absent (0%).
- T = trace (<1%).
- F = few (1%–9%).
- C = common (10%–24%).
- A = abundant (25%–40%).
- V = very abundant (40%–74%).
- D = dominant (>75%).

Shipboard sampling

VCDs display the interval where sample material was taken for shipboard analysis (all whole rounds and all samples taken to aid core description). Whole rounds consist of samples taken for interstitial water and micropaleontology samples. Samples taken to aid core description include toothpick samples that were analyzed for smear slides, thin section billets, and discrete samples for mineralogical XRD analysis (Figure F1). Typically, three smear slides were made per core in Hole A at each site, but more samples were se-

Figure F3. Siliciclastic-calcareous-siliceous ternary diagram used for lithologic classification.



lected where high variability or minor lithologies (e.g., ashes or silt laminae) were present, and fewer samples were generally taken in Holes B and C. Interstitial water samples were taken at designated intervals, and a micropaleontology sample (PAL) was obtained from the core catcher in each core. XRD samples were taken sporadically to better identify mineral components.

X-ray diffraction

Bulk sample XRD analyses were performed using a Bruker D-4 Endeavor X-ray diffractometer with a Vantec detector using Ni-filtered $\text{CuK}\alpha$ radiation (40 kV, 40 mA). Bulk powder samples were analyzed over a 2θ range of 4° – 68° with a step size of $0.01^\circ 2\theta$. Scan speed was $1.2^\circ 2\theta/\text{min}$ with a count time of 0.5 s. Samples analyzed for clay mineralogy were first treated with 10% acetic acid to remove carbonate minerals. The clay-sized fraction ($<2\ \mu\text{m}$) was separated in a 1% sodium hexametaphosphate solution using a sonic dismembrator and centrifuge. The clay-sized suspension was allowed to dry on a glass slide to create an oriented grain mount. An additional split of the sample was treated with ethylene glycol. Oriented clay aggregates were analyzed over a 2θ range of 3° – 30° . All XRD patterns were analyzed using Bruker AXS DIFFRAC.EVA version 3.0.

Biostratigraphy

The primary focus of the shipboard micropaleontological group during Expedition 353 was to provide robust age control of Upper Cretaceous to Quaternary sediments. Preliminary age assignments of core catcher samples were based on biostratigraphic analyses of calcareous nannofossils, planktonic foraminifers, and diatoms. The biostratigraphy is tied to the geomagnetic polarity timescale (GPTS) used for Expedition 353, which is based on the Geologic Timescale 2012 (GTS2012) (Gradstein et al., 2012) (Figure F4). The age of events based on the previous timescales of Gradstein et al. (2004) and Cande and Kent (1995) are also shown in Tables T1, T2, and T3.

Calcareous nannofossil, planktonic foraminifer, and diatom data were collected from core catcher samples. Where required and/or when time permitted, additional split core section samples were

taken to better define datums and zonal boundaries. Sample depths are cited in the text as midpoint depths within the sample interval, where appropriate. Datum and zone boundary levels are cited as the midpoint between the datum level and the nearest sample without the datum taxon. Microfossil preservation, abundance, preliminary assemblage composition, datum level, and zonal assignment data were entered through DESClogik into the Laboratory Information Management System (LIMS) database (<http://web.iodp.tamu.edu/LORE/>). Biostratigraphic analyses focused on Hole A at each site. The biostratigraphic data for each site are presented in datum tables, stratigraphic distribution charts, integrated biozonation figures, age-depth plots, and microfossil group abundance and preservation figures in the Biostratigraphy section of each site chapter. It should be noted that the distribution charts are based on shipboard study only and are, therefore, biased toward age-diagnostic species.

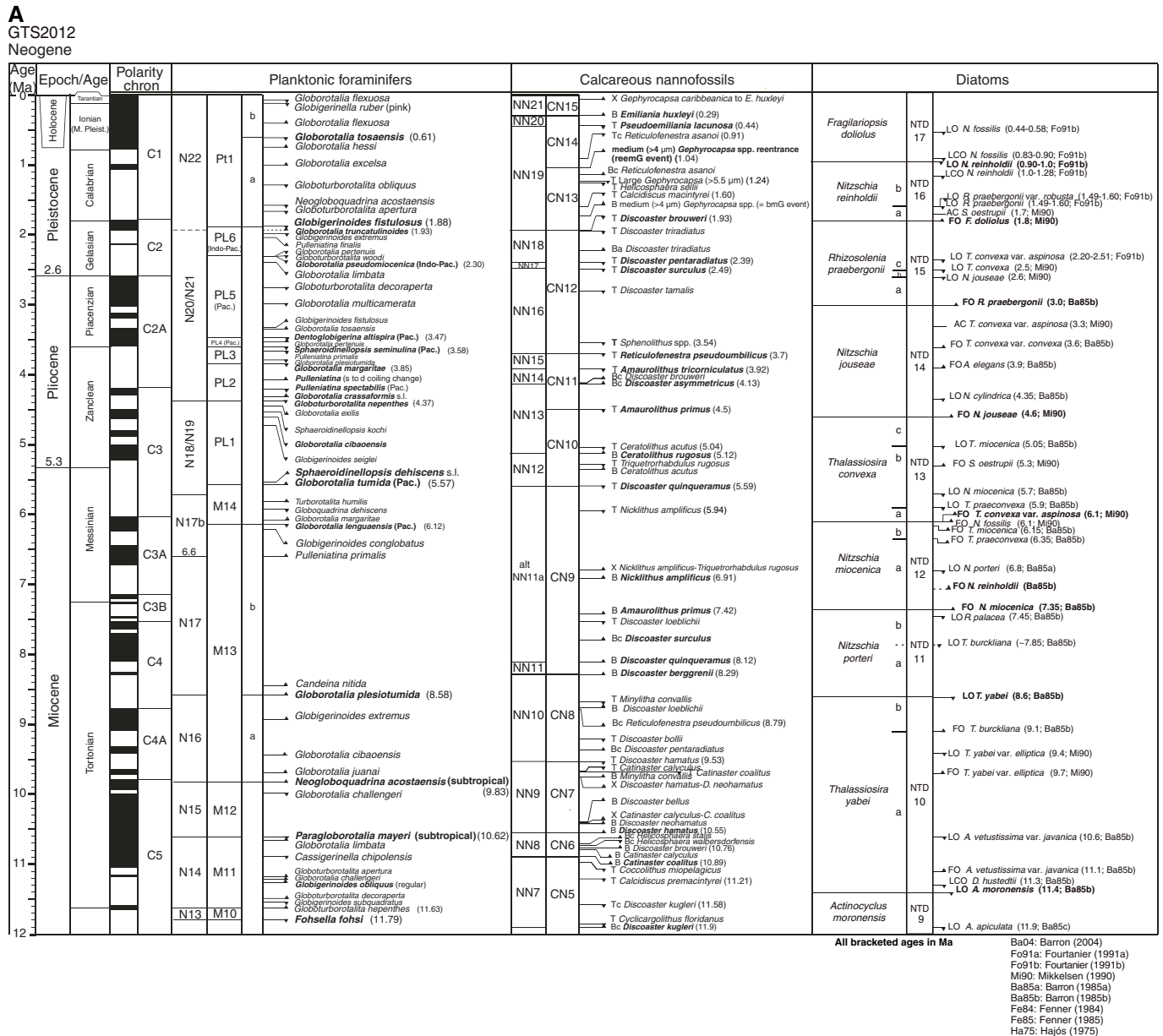
Calcareous nannofossils

Calcareous nannofossil assemblages were examined and described from smear slides made from core catcher material. At all sites, additional samples (usually one per section or one every two sections) were taken from split cores to refine the stratigraphic position of bioevents. Standard smear slides were made using bulk sediment and Norland Optical Adhesive 61 (NOA 61). After curing under UV light, slides were examined with a Zeiss Axiophot light microscope equipped with an oil immersion objective under cross-polarized transmitted light and bright field at $1000\times$ magnification. Photographs were taken using a Spot RTS system with Image Capture and Spot software.

Total calcareous nannofossil abundance within the sediment was recorded using the following criteria:

- D = dominant ($>90\%$ of sediment particles).
- A = abundant (50% – 90% of sediment particles).
- C = common (10% – 50% of sediment particles).
- F = few (1% – 10% of sediment particles).
- R = rare ($<1\%$ of sediment particles).
- B = barren (no specimens).

Figure F4. Timescale used during Expedition 353 with planktonic foraminifer, calcareous nannofossil, and diatom zones and datums through the 0–85 Ma interval. For calcareous nannofossils and foraminifers, B = bottom, T = top, Tc = top common, Bc = bottom common, X = crossover in abundance. For diatoms, FO = first occurrence, LO = last occurrence, LCO = last common occurrence, FCO = first common occurrence, AC = acme. Magnetostratigraphy, stages, and epochs are after the GTS2012 (Gradstein et al., 2012). Bold = biozone boundaries. A. 0–12 Ma. (Continued on next five pages).



Abundance of individual calcareous nannofossil taxa was recorded using the following criteria:

- VA = very abundant (>100 specimens per field of view [FOV] at 1000× magnification).
- A = abundant (10–100 specimens per FOV at 1000× magnification).
- C = common (1–9 specimens per FOV at 1000× magnification).
- F = few (1 specimen per 2–10 FOVs at 1000× magnification).
- R = rare (1 specimen per 11–100 FOVs at 1000× magnification).
- P = present (<1 specimen per 100 FOVs at 1000× magnification).

Preservation of calcareous nannofossils was qualitatively described using the following categories:

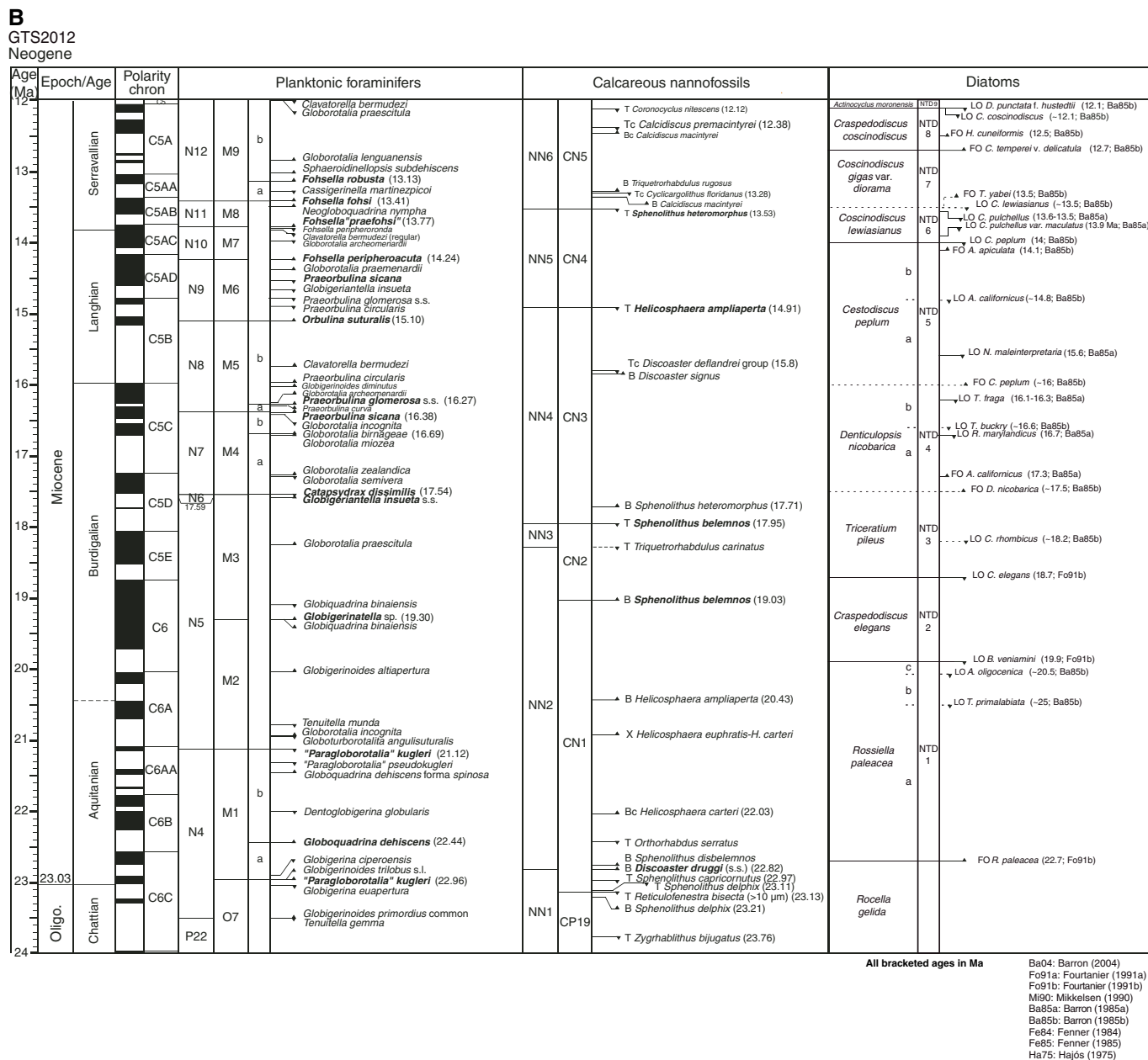
VG = very good (no evidence of dissolution and/or recrystallization, no alteration of primary morphological characteristics, and specimens identifiable to species level).

G = good (little evidence of dissolution and/or recrystallization, primary morphological characteristics only slightly altered, and specimens identifiable to species level).

M = moderate (specimens exhibit some etching and/or recrystallization, primary morphological characteristics somewhat altered, and most specimens identifiable to species level).

P = poor (specimens were severely etched or overgrown, primary morphological characteristics largely destroyed, fragmentation has occurred, and specimens often could not be identified to species and/or generic level).

Figure F4 (continued). B. 12–24 Ma. (Continued on next page.)



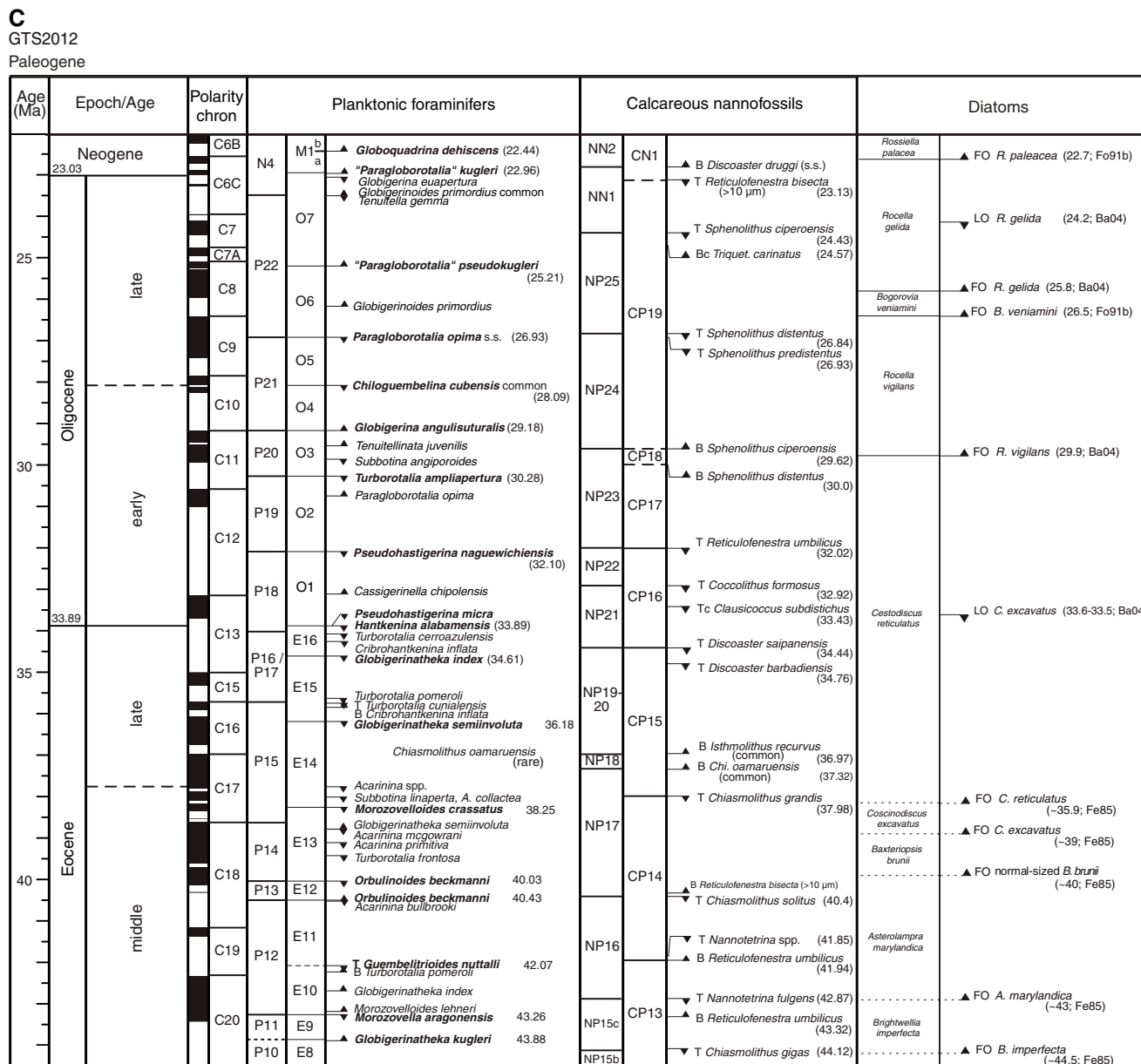
Nannofossil taxonomy followed that of Bown (1998, 2005), Perch-Nielsen (1985a, 1985b), and Nannotax3 (<http://ina.tsm-soc.org/Nannotax3>); full taxonomic lists can be found in these references. The zonal schemes of Martini (1971; Codes NN and NP) and Okada and Bukry (1980; Codes CN and CP) were used for Cenozoic calcareous nannofossil biostratigraphy. For Cretaceous calcareous nannofossil biostratigraphy, the global Upper Cretaceous biozonation of Burnett (1998; Code UC) was used in combination with the older biozonation schemes of Sissingh (1977; Code CC) and Roth (1978; Code NC). These zonations represent a general framework for the biostratigraphic classification of middle- to low-latitude nannofossil assemblages and were correlated to the Gradstein et al. (2012) GTS2012 (Figure F4; Table T1).

Foraminifers

Planktonic foraminifer zonal scheme and taxonomy

Planktonic foraminifer zones of Robaszynski and Caron (1995), Bralower et al. (1995), and Premoli Silva and Sliter (1999) as revised by Petrizzo et al. (2011) were used for the Upper Cretaceous. The zonal scheme of Berggren and Pearson (2005) as modified by Wade et al. (2011) and Luciani and Giusberty (2014) was used for the Paleogene (zonal Codes P, E, and O), and Berggren et al. (1995) as modified by Wade et al. (2011) was used for the Quaternary and Neogene (zonal codes M, PL, and PT). The planktonic foraminifer zonal scheme used during Expedition 353 is illustrated in Figure F4. Age estimates for planktonic foraminifer datums follow Gradstein et al. (2012) (Table T2). Planktonic foraminifer taxonomic concepts

Figure F4 (continued). C. 24–44 Ma. (Continued on next page.)



All bracketed ages in Ma
Ba04: Barron (2004)
Fo91a: Fourtanier (1991a)
Fo91b: Fourtanier (1991b)
Mi90: Mikkelsen (1990)
Ba85a: Barron (1985a)
Ba85b: Barron (1985b)
Fe84: Fenner (1984)
Fe85: Fenner (1985)
Ha75: Hajós (1975)

in the Cretaceous follow those of Robaszynski and Caron (1979), Robaszynski et al. (1984), and Hornibrook et al. (1989); taxonomic concepts in the Cenozoic follow those of Jenkins (1971), Blow (1979), Kennett and Srinivasan (1983), Bolli and Saunders (1985), Toumarkine and Luterbacher (1985), Scott et al. (1990), Spezzaferri (1994), Pearson (1995), Chaisson and Pearson (1997), Olsson et al. (1999), and Pearson et al. (2006).

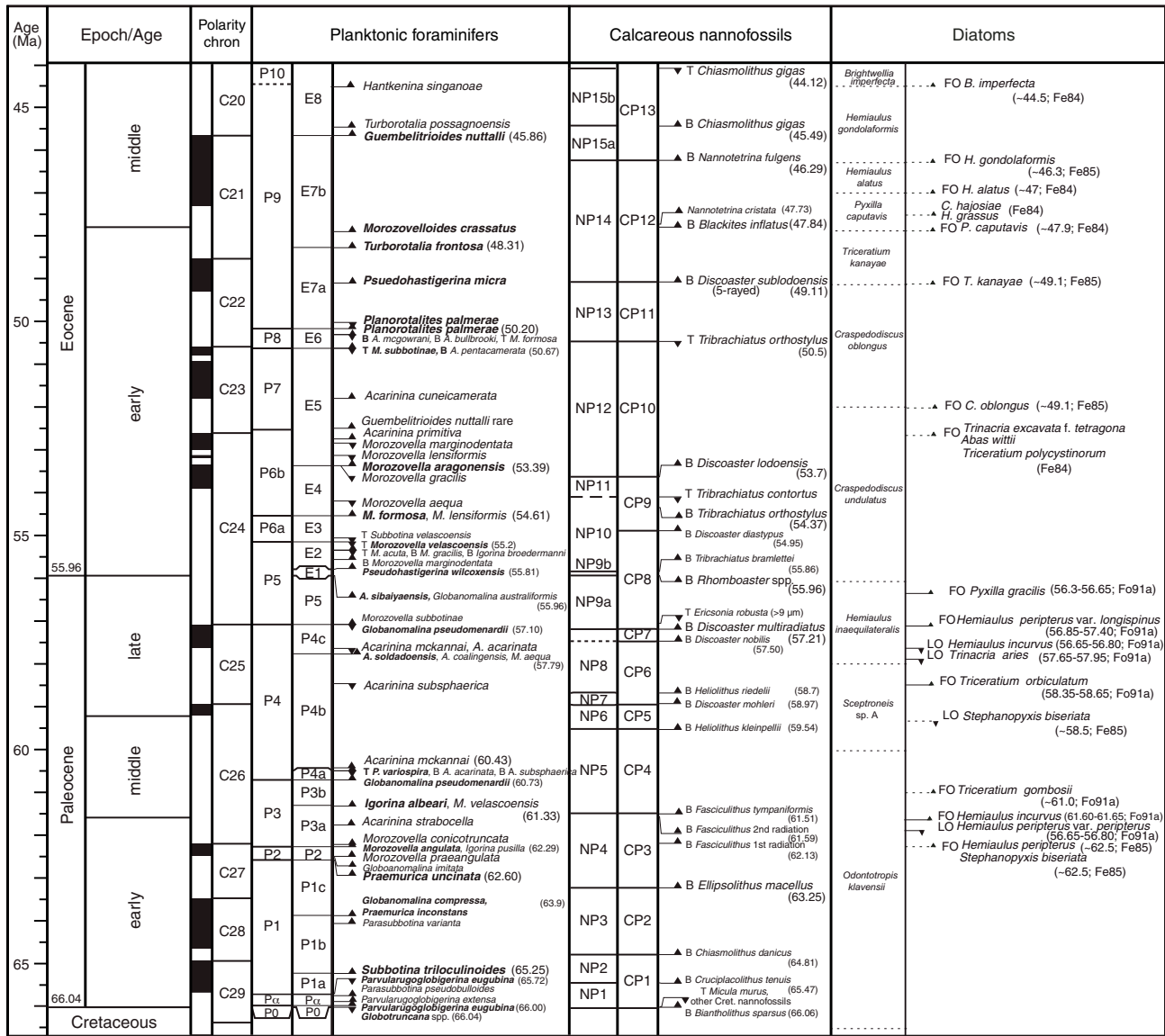
Methods of study for foraminifers

To obtain foraminifers from core catcher samples, a 100 cm³ whole-round sample was soaked in tap water, disaggregated using

sodium metaphosphate solution when necessary, and washed over a 63 µm sieve. Planktonic foraminiferal age determination was initially established using the wet samples in sieves. Subsequently, all samples were dried in sieves or on filter papers in a low-temperature oven (~50°C) and then examined under a binocular light microscope for planktonic foraminiferal assemblages. All sieves were cleaned in an ultrasonic bath and rinsed with a methylene blue solution between successive samples as a precaution against cross contamination. The samples were then divided with a microsplitter into separate aliquots for examination by members of the shipboard micropaleontological team.

Figure F4 (continued). D. 44–67 Ma. (Continued on next page.)

D
GTS2012
Paleogene



All bracketed ages in Ma
Ba04: Barron (2004)
Fo91a: Fourtanier (1991a)
Fo91b: Fourtanier (1991b)
Mf90: Mikkelsen (1990)
Ba85a: Barron (1985a)
Ba85b: Barron (1985b)
Fe84: Fenner (1984)
Fe85: Fenner (1985)
Ha75: Hajós (1975)

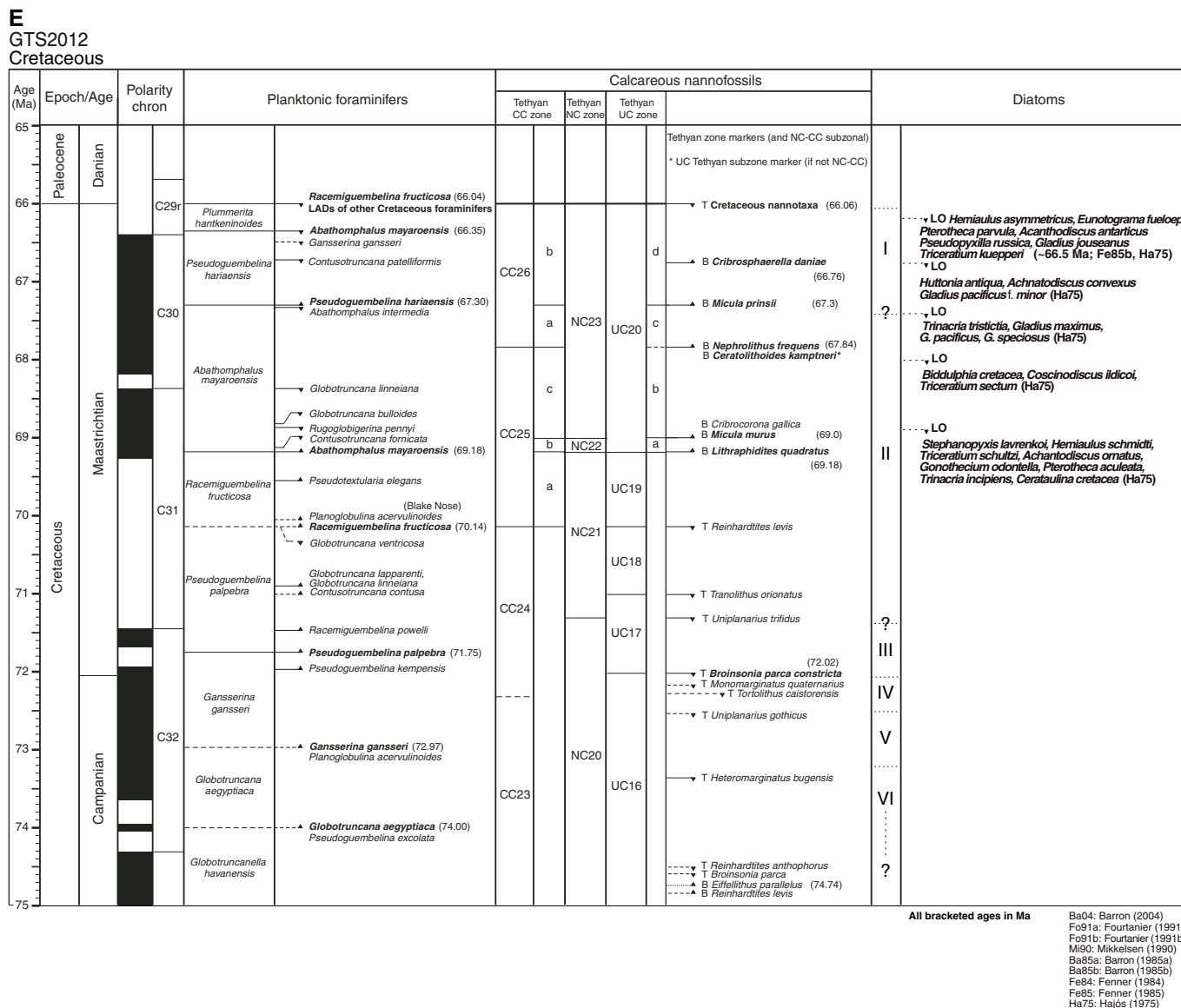
All age-diagnostic species of planktonic foraminifers were picked and mounted onto 60-square faunal slides. As time allowed, other species and types of microfossils were also picked and mounted onto the same slides.

A measure of foraminifers per volume of sediment is necessary to accurately determine the volume of sediment necessary for certain analyses, especially for postexpedition stable isotopic studies of less abundant benthic foraminifers. To aid in future sampling requests, foraminifer density measurements were calculated by counting all foraminifers and all benthic foraminifers per 10 cm³ of sediment, using either the whole sample or a split.

During shipboard examination, abundance of all planktonic foraminifers in the >150 µm grain-size fractions of washed samples was categorized as

- D = dominant (>50% planktonic foraminifers in total residue),
- A = abundant (20%–50% planktonic foraminifers in total residue),
- C = common (5%–20% planktonic foraminifers in total residue),
- F = few (1%–5% planktonic foraminifers in total residue), and
- R = rare (<1% planktonic foraminifers in total residue).

Figure F4 (continued). E. 65–75 Ma. (Continued on next page.)



Relative abundance of individual planktonic foraminifer species was recorded as

- D = dominant (>30% of the planktonic foraminiferal assemblage),
- A = abundant (10%–30% of the planktonic foraminiferal assemblage),
- C = common (5%–10% of the planktonic foraminiferal assemblage),
- F = few (1%–5% of the planktonic foraminiferal assemblage), and
- R = rare (<1% of the planktonic foraminiferal assemblage).

Preservation of planktonic foraminifers was categorized as

- G = good (mostly whole specimens, well-preserved ornamentation and surface ultrastructure, and nearly all specimens identifiable to species level),

- M = moderate (specimens often etched or broken, modified ornamentation and surface ultrastructure, and majority of specimens identifiable to species level), and
- P = poor (most specimens heavily encrusted, recrystallized, diagenetically overgrown, crushed, or broken and most specimens difficult to identify to species level).

Diatoms

Diatom zonal scheme and taxonomy

The diatom zonal scheme used here mainly follows biostratigraphic studies by Strelnikova (1974), Hajós (1975), Fenner (1984, 1985), Barron (1980, 1983, 1985a, 1985b), Harwood (1988), Mikkelsen (1990), Fenner and Mikkelsen (1990), and Fourtanier (1991b). Datums were modified following the updated geologic timescale (Gradstein et al., 2012) (Figure F4; Table T3). The biozones used for the Neogene are those described by Barron (1980, 1983, 1985a, 1985b) for the Pacific Ocean; however, some biozone boundaries were modified following bioevent ages calibrated for the

Figure F4 (continued). F. 75–85 Ma.

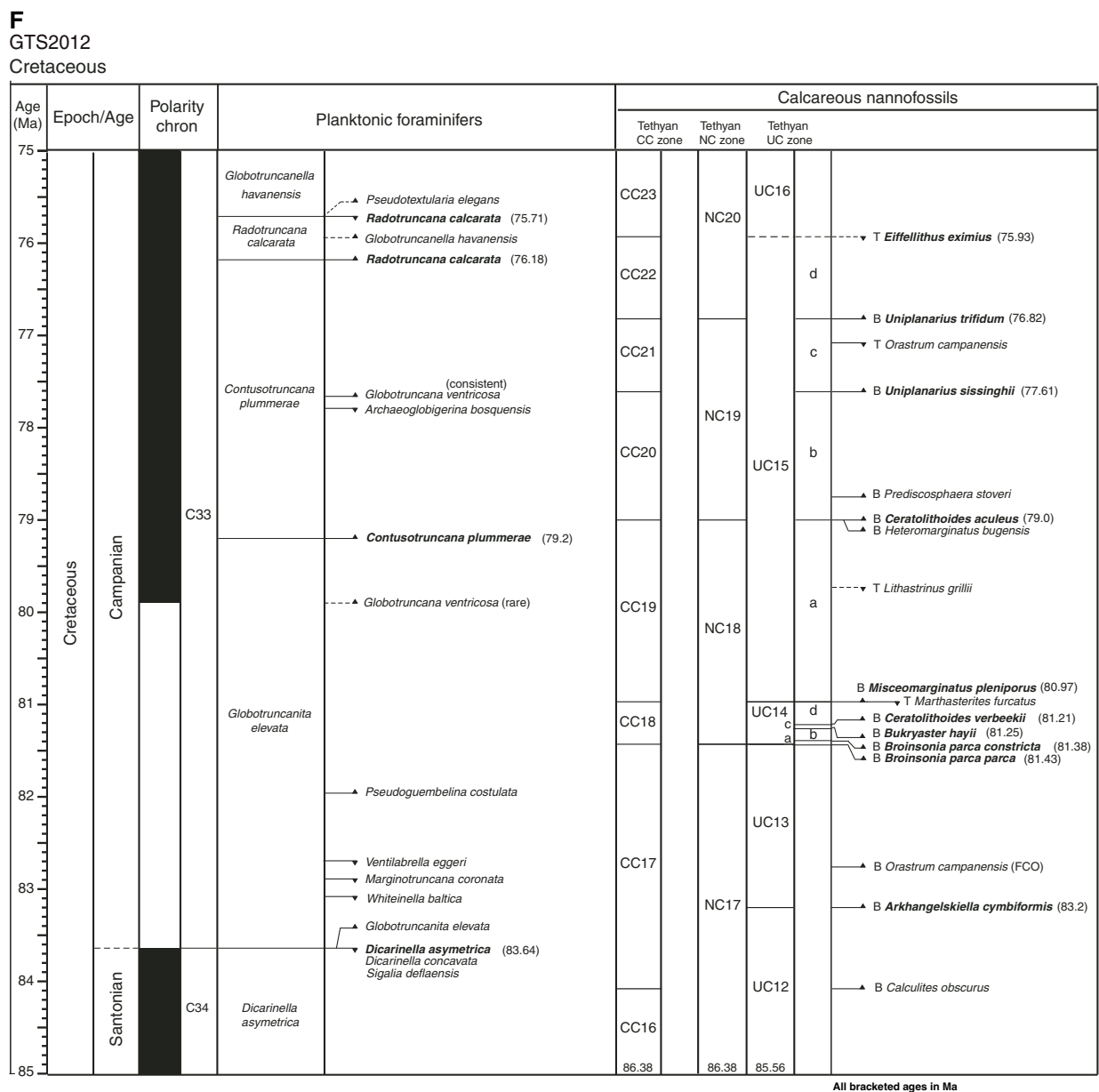


Table T1. Age estimates of calcareous nannofossil datum events, Expedition 353. B = bottom (lowest occurrence), T = top (highest occurrence), Bc = lowest common occurrence, Tc = highest common occurrence, Bd = lowest dominant occurrence, Td = highest dominant occurrence, X = crossover of dominance. GTS2012 = Geologic Timescale 2012. (Continued on next three pages.) [Download table in .csv format.](#)

Zone base (Martini, 1971; Sissingh, 1977)	Zone base (Okada and Bukry, 1980; Roth, 1978)	Species event	GTS2012 age (Ma)	Calibration reference
		X <i>Gephyrocapsa caribbeanica</i> – <i>Emiliana huxleyi</i>	0.09	Gradstein et al., 2012
NN21	CN15	B <i>Emiliana huxleyi</i>	0.29	Gradstein et al., 2012
NN20	CN14b	T <i>Pseudoemiliana lacunosa</i>	0.44	Gradstein et al., 2012
		Tc <i>Reticulofenestra asanoi</i>	0.91	Gradstein et al., 2012
		Td small <i>Gephyrocapsa</i> spp.	1.02	Gradstein et al., 2012
		B <i>Gephyrocapsa omega</i>	1.02	Gradstein et al., 2012
	CN14a	B medium <i>Gephyrocapsa</i> spp. reentrance	1.04	Gradstein et al., 2012
		Bc <i>Reticulofenestra asanoi</i>	1.14	Gradstein et al., 2012
		T large <i>Gephyrocapsa</i> spp. (>5.5 μm)	1.24	Gradstein et al., 2012
		Bc small <i>Gephyrocapsa</i> spp.	1.24	Gradstein et al., 2012
		T <i>Helicosphaera sellii</i>	1.26	Gradstein et al., 2012

Table T1 (continued). (Continued on next page.)

Zone base (Martini, 1971; Sissingh, 1977)	Zone base (Okada and Bukry, 1980; Roth, 1978)	Species event	GTS2012 age (Ma)	Calibration reference
		B large <i>Gephyrocapsa</i> spp.	1.46	Gradstein et al., 2012
		T <i>Calcidiscus macintyre</i>	1.6	Gradstein et al., 2012
	CN13b	B medium <i>Gephyrocapsa</i> spp.	1.73	Gradstein et al., 2012
NN19	CN13a	T <i>Discoaster brouweri</i>	1.93	Gradstein et al., 2012
		T <i>Discoaster triradiatus</i>	1.95	Gradstein et al., 2012
		Bc <i>Discoaster triradiatus</i>	2.22	Gradstein et al., 2012
NN18	CN12d	T <i>Discoaster pentaradiatus</i>	2.39	Gradstein et al., 2012
NN17	CN12c	T <i>Discoaster surculus</i>	2.49	Gradstein et al., 2012
		Pliocene/Pleistocene boundary	2.59	Gradstein et al., 2012
	CN12b	T <i>Discoaster tamalis</i>	2.8	Gradstein et al., 2012
		T <i>Sphenolithus</i> spp.	3.54	Gradstein et al., 2012
NN16	CN12a	T <i>Reticulofenestra pseudumbilicus</i>	3.7	Gradstein et al., 2012
NN15		T <i>Amaurolithus tricornulatus</i>	3.92	Gradstein et al., 2012
		Bc <i>Discoaster brouweri</i>	4.12	Gradstein et al., 2012
NN14	CN11b	Bc <i>Discoaster asymmetricus</i>	4.13	Gradstein et al., 2012
	CN11a	T <i>Amaurolithus primus</i>	4.5	Gradstein et al., 2012
		T <i>Ceratolithus acutus</i>	5.04	Gradstein et al., 2012
NN13	CN10c	B <i>Ceratolithus rugosus</i>	5.12	Gradstein et al., 2012
		T <i>Triquetrorhabdulus rugosus</i>	5.28	Gradstein et al., 2012
		Pliocene/Miocene boundary	5.33	Gradstein et al., 2012
		B <i>Ceratolithus larrymayeri</i>	5.34	Gradstein et al., 2012
	CN10b	B <i>Ceratolithus acutus</i>	5.35	Gradstein et al., 2012
NN12		T <i>Discoaster quinqueramus</i>	5.59	Gradstein et al., 2012
	CN9d	T <i>Nicklithus amplificus</i>	5.94	Gradstein et al., 2012
		X <i>Nicklithus amplificus</i> – <i>Triquetrorhabdulus rugosus</i>	6.79	Gradstein et al., 2012
	CN9c	B <i>Nicklithus amplificus</i>	6.91	Gradstein et al., 2012
	CN9b	B <i>Amaurolithus primus</i> , <i>Amaurolithus</i> spp.	7.42	Gradstein et al., 2012
		Bc <i>Discoaster loeblichii</i>	7.53	Gradstein et al., 2012
		Bc <i>Discoaster surculus</i>	7.79	Gradstein et al., 2012
		B <i>Discoaster quinqueramus</i>	8.12	Gradstein et al., 2012
NN11	CN9a	B <i>Discoaster berggrenii</i>	8.29	Gradstein et al., 2012
		T <i>Minylitha convallis</i>	8.68	Gradstein et al., 2012
		B <i>Discoaster loeblichii</i>	8.77	Gradstein et al., 2012
		Bc <i>Reticulofenestra pseudumbilicus</i>	8.79	Gradstein et al., 2012
		T <i>Discoaster bollii</i>	9.21	Gradstein et al., 2012
		Bc <i>Discoaster pentaradiatus</i>	9.37	Gradstein et al., 2012
NN10	CN8	T <i>Discoaster hamatus</i>	9.53	Gradstein et al., 2012
		T <i>Catinaster calyculus</i>	9.67	Gradstein et al., 2012
		T <i>Catinaster coalitus</i>	9.69	Gradstein et al., 2012
		B <i>Minylitha convallis</i>	9.75	Gradstein et al., 2012
		X <i>Discoaster hamatus</i> – <i>Discoaster neohamatus</i>	9.76	Gradstein et al., 2012
		B <i>Discoaster bellus</i>	10.4	Gradstein et al., 2012
		X <i>Catinaster calyculus</i> – <i>Catinaster coalitus</i>	10.41	Gradstein et al., 2012
		B <i>Discoaster neohamatus</i>	10.52	Gradstein et al., 2012
NN9	CN7	B <i>Discoaster hamatus</i>	10.55	Gradstein et al., 2012
		Bc <i>Helicosphaera stalis</i>	10.71	Gradstein et al., 2012
		Tc <i>Helicosphaera walbersdorfensis</i>	10.74	Gradstein et al., 2012
		B <i>Discoaster brouweri</i>	10.76	Gradstein et al., 2012
		B <i>Catinaster calyculus</i>	10.79	Gradstein et al., 2012
NN8	CN6	B <i>Catinaster coalitus</i>	10.89	Gradstein et al., 2012
		T <i>Coccolithus miopelagicus</i>	10.97	Gradstein et al., 2012
		T <i>Calcidiscus premacintyre</i>	11.21	Gradstein et al., 2012
		Tc <i>Discoaster kugleri</i>	11.58	Gradstein et al., 2012
		T <i>Cyclicargolithus floridanus</i>	11.85	Gradstein et al., 2012
NN7	CN5b	Bc <i>Discoaster kugleri</i>	11.9	Gradstein et al., 2012
		T <i>Coronocyclus nitescens</i>	12.12	Gradstein et al., 2012
		Tc <i>Calcidiscus premacintyre</i>	12.38	Gradstein et al., 2012
		Bc <i>Calcidiscus macintyre</i>	12.46	Gradstein et al., 2012
		B <i>Reticulofenestra pseudumbilicus</i>	12.83	Gradstein et al., 2012
		B <i>Triquetrorhabdulus rugosus</i>	13.27	Gradstein et al., 2012
		Tc <i>Cyclicargolithus floridanus</i>	13.28	Gradstein et al., 2012
		B <i>Calcidiscus macintyre</i>	13.36	Gradstein et al., 2012
NN6	CN5a	T <i>Sphenolithus heteromorphus</i>	13.53	Gradstein et al., 2012
NN5	CN4	T <i>Helicosphaera ampliaperta</i>	14.91	Gradstein et al., 2012
		Ta <i>Discoaster deflandrei</i> group	15.8	Gradstein et al., 2012
		B <i>Discoaster signus</i>	15.85	Gradstein et al., 2012
		B <i>Sphenolithus heteromorphus</i>	17.71	Gradstein et al., 2012
NN4	CN3	T <i>Sphenolithus belemnus</i>	17.95	Gradstein et al., 2012

Table T1 (continued). (Continued on next page.)

Zone base (Martini, 1971; Sissingh, 1977)	Zone base (Okada and Bukry, 1980; Roth, 1978)	Species event	GTS2012 age (Ma)	Calibration reference
NN3	CN2	T <i>Triquetrorhabdulus carinatus</i>	18.28	Gradstein et al., 2012
		B <i>Sphenolithus belemnus</i>	19.03	Gradstein et al., 2012
		B <i>Helicosphaera ampliaperta</i>	20.43	Gradstein et al., 2012
		X <i>Helicosphaera euphratis</i> – <i>Helicosphaera carteri</i>	20.92	Gradstein et al., 2012
		Bc <i>Helicosphaera carteri</i>	22.03	Gradstein et al., 2012
NN2	CN1c	T <i>Orthorhabdulus serratus</i>	22.42	Gradstein et al., 2012
		B <i>Sphenolithus disbelemnus</i>	22.76	Gradstein et al., 2012
		B <i>Discoaster druggi</i> (sensu stricto)	22.82	Gradstein et al., 2012
		T <i>Sphenolithus capricornutus</i>	22.97	Gradstein et al., 2012
		Miocene/Oligocene boundary	23.03	Gradstein et al., 2012
NN1	CN1a-b	T <i>Sphenolithus delphix</i>	23.11	Gradstein et al., 2012
		T <i>Reticulofenestra bisecta</i>	23.13	Gradstein et al., 2012
		B <i>Sphenolithus delphix</i>	23.21	Gradstein et al., 2012
		T <i>Zygrhablithus bijugatus</i>	23.76	Gradstein et al., 2012
		T <i>Sphenolithus ciperoensis</i>	24.43	Gradstein et al., 2012
NP25	CP19b	Tc <i>Cyclicargolithus abisectus</i>	22.67	Gradstein et al., 2012
		X <i>Triquetrorhabdulus longus</i> – <i>Triquetrorhabdulus carinatus</i>	24.67	Gradstein et al., 2012
		T <i>Chiasmolithus altus</i>	25.44	Gradstein et al., 2012
		Bc <i>Triquetrorhabdulus carinatus</i>	26.57	Gradstein et al., 2012
		T <i>Sphenolithus distentus</i>	26.84	Gradstein et al., 2012
NP24	CP19a	T <i>Sphenolithus predistentus</i>	26.93	Gradstein et al., 2012
		T <i>Sphenolithus pseudoradians</i>	28.73	Gradstein et al., 2012
NP23	CP18	B <i>Sphenolithus ciperoensis</i>	29.62	Gradstein et al., 2012
NP22	CP16c	B <i>Sphenolithus distentus</i>	30.00	Gradstein et al., 2012
		T <i>Reticulofenestra umbilicus</i>	32.02	Gradstein et al., 2012
NP21	CP16b	T <i>Coccolithus formosus</i>	32.92	Gradstein et al., 2012
		Ta <i>Clausiococcus subdistichus</i>	33.43	Gradstein et al., 2012
NP21	CP16a	Oligocene/Eocene boundary	33.89	Gradstein et al., 2012
		T <i>Discoaster saipanensis</i>	34.44	Gradstein et al., 2012
NP20-19	CP15	T <i>Discoaster barbadiensis</i>	34.76	Gradstein et al., 2012
		T <i>Reticulofenestra reticulata</i>	35.40	Gradstein et al., 2012
		B <i>Isthmolithus recurvus</i>	36.97	Gradstein et al., 2012
		B <i>Chiasmolithus oamaruensis</i>	37.32	Gradstein et al., 2012
		T <i>Chiasmolithus grandis</i>	37.98	Gradstein et al., 2012
NP18	CP14b	B <i>Chiasmolithus oamaruensis</i>	38.09	Gradstein et al., 2012
		B <i>Reticulofenestra bisecta</i>	38.25	Gradstein et al., 2012
NP17	CP14a	T <i>Chiasmolithus solitus</i>	40.4	Gradstein et al., 2012
		B <i>Reticulofenestra reticulata</i>	41.66	Gradstein et al., 2012
NP16	CP13c	T <i>Nannotetrina</i> spp.	41.85	Gradstein et al., 2012
		T <i>Nannotetrina fulgens</i>	42.87	Gradstein et al., 2012
NP15c	CP13b	B <i>Reticulofenestra umbilicus</i>	43.32	Gradstein et al., 2012
		T <i>Chiasmolithus gigas</i>	44.12	Gradstein et al., 2012
NP15b	CP13a	B <i>Chiasmolithus gigas</i>	45.49	Gradstein et al., 2012
		T <i>Discoaster sublodoensis</i> (5-rayed)	46.21	Gradstein et al., 2012
NP15a	CP12b	T <i>Discoaster lodoensis</i>	46.29	Gradstein et al., 2012
		T <i>Blackites piriformis</i>	47.41	Gradstein et al., 2012
		T <i>Blackites piriformis</i>	47.73	Gradstein et al., 2012
		B <i>Nannotetrina cristata</i> , <i>Nannotetrina</i> spp.	47.73	Gradstein et al., 2012
		B <i>Nannotetrina cristata</i> , <i>Nannotetrina</i> spp.	47.73	Gradstein et al., 2012
NP14b	CP12a	B <i>Blackites inflatus</i>	47.84	Gradstein et al., 2012
		B <i>Blackites piriformis</i>	47.94	Gradstein et al., 2012
NP14a	CP11	B <i>Discoaster sublodoensis</i> (5-rayed)	49.11	Gradstein et al., 2012
NP13	CP10	T <i>Tribrachiatus orthostylus</i>	50.50	Gradstein et al., 2012
		B <i>Reticulofenestra</i>	50.50	Gradstein et al., 2012
NP12	CP9b	B <i>Discoaster lodoensis</i>	53.70	Gradstein et al., 2012
		T <i>Tribrachiatus contortus</i>	54.17	Gradstein et al., 2012
NP11	CP9a	B <i>Sphenolithus radians</i>	54.17	Gradstein et al., 2012
		B <i>Tribrachiatus orthostylus</i>	54.37	Gradstein et al., 2012
NP10	CP8b	T <i>Tribrachiatus bramlettei</i>	54.42	Gradstein et al., 2012
		B <i>Tribrachiatus contortus</i>	54.76	Gradstein et al., 2012
		B <i>Discoaster diastypus</i>	54.95	Gradstein et al., 2012
		Bc <i>Tribrachiatus bramlettei</i>	55.42	Gradstein et al., 2012
		T <i>Fasciculithus</i> spp.	55.64	Gradstein et al., 2012
		Bc <i>Campylosphaera eodela</i>	55.81	Gradstein et al., 2012
		B <i>Tribrachiatus bramlettei</i>	55.86	Gradstein et al., 2012
		B <i>Rhombaster</i> spp.	55.96	Gradstein et al., 2012
		Eocene/Paleocene boundary	55.96	Gradstein et al., 2012
		B <i>Campylosphaera eodela</i>	56.66	Gradstein et al., 2012
T <i>Ericsonia robusta</i>	56.78	Gradstein et al., 2012		

Table T1 (continued).

Zone base (Martini, 1971; Sissingh, 1977)	Zone base (Okada and Bukry, 1980; Roth, 1978)	Species event	GTS2012 age (Ma)	Calibration reference
NP9	CP8a	Bc <i>Discoaster multiradiatus</i>	57.21	Gradstein et al., 2012
		B <i>Discoaster multiradiatus</i> (rare)	57.32	Gradstein et al., 2012
		T <i>Discoaster okadai</i>	57.47	Gradstein et al., 2012
		B <i>Discoaster okadai</i>	57.50	Gradstein et al., 2012
NP8	CP6	B <i>Discoaster nobilis</i>	57.50	Gradstein et al., 2012
		B <i>Heliolithus riedelii</i>	58.70	Gradstein et al., 2012
		T <i>Heliolithus kleinpellii</i>	58.80	Gradstein et al., 2012
NP7	CN7	B <i>Discoaster mohleri</i>	58.97	Gradstein et al., 2012
NP6	CP6	B <i>Heliolithus kleinpellii</i>	59.54	Gradstein et al., 2012
		B <i>Heliolithus cantabrigiae</i>	59.60	Gradstein et al., 2012
		B <i>Sphenolithus anarrhopus</i>	59.68	Gradstein et al., 2012
		T <i>Fasciculithus pileatus</i>	60.73	Gradstein et al., 2012
NP5	CP5	B <i>Chiasmolithus consuetus</i>	61.03	Gradstein et al., 2012
		B <i>Fasciculithus tympaniformis</i>	61.51	Gradstein et al., 2012
		B <i>Fasciculithus</i> 2nd radiation (B F. ulii)	61.59	Gradstein et al., 2012
		B <i>Neochiastozygus perfectus</i>	61.76	Gradstein et al., 2012
		B <i>Sphenolithus primus</i>	61.98	Gradstein et al., 2012
		B <i>Chiasmolithus bidens/edentulus</i>	62.07	Gradstein et al., 2012
NP4	CP4	B <i>Fasciculithus</i> 1st radiation	62.13	Gradstein et al., 2012
		B <i>Ellipsolithus macellus</i>	63.25	Gradstein et al., 2012
NP3	CP2	B <i>Chiasmolithus danicus</i>	64.81	Gradstein et al., 2012
NP2	CP1b	B <i>Cruciplacolithus tenuis</i>	65.47	Gradstein et al., 2012
		B <i>Cruciplacolithus primus</i> (3.5–5 µm)	65.76	Gradstein et al., 2012
		B <i>Neobiscutum parvulum</i>	65.9	Gradstein et al., 2012
		Cretaceous/Paleogene boundary	66.04	Gradstein et al., 2012
		T <i>Micula murus</i> , Cretaceous nannofossils	66.04	Gradstein et al., 2012
		B <i>Biantholithus sparsus</i> ; B <i>Calcispheres</i>	66.06	Gradstein et al., 2012
		B <i>Cribrosphera daniae</i>	66.76	Gradstein et al., 2012
		B <i>Micula prinsii</i>	67.3	Gradstein et al., 2012
		B <i>Ceratolithoides kamptneri</i>	67.84	Gradstein et al., 2012
		B <i>Nephrolithus frequens</i>	67.84	Gradstein et al., 2012
CC25c	NC23	B <i>Micula murus</i>	69	Gradstein et al., 2012
		B <i>Cribracorona gallica</i>	69	Gradstein et al., 2012
CC25b	NC22	B <i>Lithraphidites quadratus</i>	69.18	Gradstein et al., 2012
		T <i>Reinhardtites levis</i>	70.14	Gradstein et al., 2012
CC25a	NC21	T <i>Tranolithus orionatus</i>	71.01	Gradstein et al., 2012
		T <i>Uniplanarius trifidus</i>	71.31	Gradstein et al., 2012
		T <i>Broinsonia parca constricta</i>	72.02	Gradstein et al., 2012
		Maastrichtian/Campanian boundary	72.05	Gradstein et al., 2012
		T <i>Monomarginatus quaternarius</i>	72.18	Gradstein et al., 2012
		T <i>Tortolithus caistorensis</i>	72.28	Gradstein et al., 2012
		T <i>Tranolithus phacelosus</i>	72.32	Gradstein et al., 2012
		T <i>Uniplanarius gothicus</i>	72.54	Gradstein et al., 2012
		B <i>Heteromarginatus bugensis</i>	73.36	Gradstein et al., 2012
		T <i>Rheinhardtites anthophorus</i>	74.51	Gradstein et al., 2012
CC24	NC21	T <i>Bronsonia parca</i>	74.59	Gradstein et al., 2012
		B <i>Eiffellithus parallelus</i>	74.74	Gradstein et al., 2012
		B <i>Rheinhardtites levis</i>	74.84	Gradstein et al., 2012
		T <i>Eiffellithus eximus</i>	75.93	Gradstein et al., 2012
CC23	NC20	B <i>Uniplanarius trifidus</i>	76.82	Gradstein et al., 2012
T <i>Orastrum campanensis</i>		77.08	Gradstein et al., 2012	
B <i>Uniplanarius sissinghii</i>		77.61	Gradstein et al., 2012	
CC21	NC20	B <i>Prediscosphaera stoveri</i>	78.75	Gradstein et al., 2012
		B <i>Ceratolithoides aculeus</i>	79	Gradstein et al., 2012
CC20	NC19	B <i>Heteromarginatus bugensis</i>	79.01	Gradstein et al., 2012
		T <i>Lithastrinus grillii</i>	79.73	Gradstein et al., 2012
		T <i>Marthasterites furcatus</i>	80.97	Gradstein et al., 2012
		B <i>Misceomarginatus pleniporus</i>	80.97	Gradstein et al., 2012
CC19	NC19	B <i>Ceratolithoides verbeekii</i>	81.21	Gradstein et al., 2012
		B <i>Bukryaster hayii</i>	81.25	Gradstein et al., 2012
		B <i>Broinsonia parca constricta</i>	81.38	Gradstein et al., 2012
		B <i>Broinsonia parca parca</i>	81.43	Gradstein et al., 2012
CC18	NC18	Bc <i>Orastrum campanensis</i>	82.76	Gradstein et al., 2012
		B <i>Arkhangelskiella cymbiformis</i>	83.2	Gradstein et al., 2012
		Campanian/Santonian boundary	~83.64	Gradstein et al., 2012
		B <i>Calculites obscurus</i>	84.08	Gradstein et al., 2012
CC17				

Table T2. Age estimates of planktonic foraminifer datum events, Expedition 353. GTS2012 = geomagnetic timescale of Gradstein et al. (2012), GTS2004 = geomagnetic timescale of Gradstein et al. (2004). T = top, B = bottom, X = coiling direction change. (Continued on next four pages.) [Download table in .csv format.](#)

Zone/subzone base	Species event	GTS2012 age (Ma)	Calibration reference	GTS2004 age (Ma)	Calibration reference	Cande and Kent (1995) age (Ma)	Calibration reference
	T <i>Globorotalia flexuosa</i>	0.07	Gradstein et al., 2012	0.07	Wade et al., 2011	0.07	Wade et al., 2011
	T <i>Globigerinoides ruber</i> (pink); Indo-Pacific	0.12	Gradstein et al., 2012			0.12	Wade et al., 2011
	B <i>Globorotalia flexuosa</i>	0.40	Gradstein et al., 2012	0.4	Wade et al., 2011	0.40	Wade et al., 2011
PT1b	T <i>Globorotalia tosaensis</i>	0.61	Gradstein et al., 2012	0.61	Lourens et al., 2004	0.61	Wade et al., 2011
	B <i>Globorotalia hessi</i>	0.75	Gradstein et al., 2012	0.75	Wade et al., 2011	0.75	Wade et al., 2011
	X random to dextral in <i>Pulleniatina</i>	0.80	Gradstein et al., 2012			0.80	Wade et al., 2011
	B <i>Globorotalia excelsa</i>	1.00	Gradstein et al., 2012			1.00	Wade et al., 2011
	T <i>Globigerinoides obliquus</i>	1.30	Gradstein et al., 2012	1.3	Lourens et al., 2004	1.30	Wade et al., 2011
	T <i>Neogloboquadrina acostaensis</i>	1.58	Gradstein et al., 2012				
PT1a	T <i>Globigerinoides fistulosus</i>	1.88	Gradstein et al., 2012	1.88	Lourens et al., 2004	1.88	Wade et al., 2011
	B <i>Globorotalia truncatulinoides</i>	1.93	Gradstein et al., 2012	1.93	Lourens et al., 2004	1.93	Wade et al., 2011
	T <i>Globigerinoides extremus</i>	1.98	Gradstein et al., 2012	1.98	Lourens et al., 2004	1.99	Wade et al., 2011
	B <i>Pulleniatina finalis</i>	2.04	Gradstein et al., 2012	2.04	Lourens et al., 2004	2.05	Wade et al., 2011
	T <i>Globorotalia pertenuis</i>	2.30	Gradstein et al., 2012	2.3	Lourens et al., 2004	2.30	Wade et al., 2011
	T <i>Globoturborotalita woodi</i>	2.30	Gradstein et al., 2012	2.3	Lourens et al., 2004	2.30	Wade et al., 2011
PL6 (Indo-Pacific)	T <i>Globorotalia pseudomiocenica</i> (Indo-Pacific)	2.30	Gradstein et al., 2012			2.30	Wade et al., 2011
	T <i>Globorotalia limbata</i>	2.39	Gradstein et al., 2012	2.39	Lourens et al., 2004	2.39	Wade et al., 2011
	Pliocene/Pleistocene boundary	2.59	Gradstein et al., 2012	1.81	Aguirre and Pasini, 1985	1.80	Cande and Kent, 1995
	T <i>Globoturborotalita decoraperta</i>	2.75	Gradstein et al., 2012	2.75	Lourens et al., 2004	2.75	Wade et al., 2011
	T <i>Globorotalia multicamerata</i>	2.98	Gradstein et al., 2012	2.98	Lourens et al., 2004	2.99	Wade et al., 2011
	B <i>Globigerinoides fistulosus</i>	3.33	Gradstein et al., 2012	3.33	Wade et al., 2011	3.33	Wade et al., 2011
	B <i>Globorotalia tosaensis</i>	3.35	Gradstein et al., 2012	3.35	Wade et al., 2011	3.35	Wade et al., 2011
PL5	T <i>Dentoglobigerina altispira</i> (Pacific)	3.47	Gradstein et al., 2012			3.46	Wade et al., 2011
	B <i>Globorotalia pertenuis</i>	3.52	Gradstein et al., 2012	3.52	Lourens et al., 2004	3.51	Wade et al., 2011
PL4	T <i>Sphaeroidinellopsis seminulina</i> (Pacific)	3.58	Gradstein et al., 2012			3.57	Wade et al., 2011
	T <i>Pulleniatina primalis</i>	3.66	Gradstein et al., 2012			3.65	Wade et al., 2011
	T <i>Globorotalia plesiotumida</i>	3.77	Gradstein et al., 2012	3.77	Lourens et al., 2004	3.76	Wade et al., 2011
PL3	T <i>Globorotalia margaritae</i>	3.85	Gradstein et al., 2012	3.85	Lourens et al., 2004	3.84	Wade et al., 2011
	X <i>Pulleniatina</i> coiling sinistral to dextral	4.08	Gradstein et al., 2012	4.08	Lourens et al., 2004	4.07	Wade et al., 2011
	T <i>Pulleniatina spectabilis</i> (Pacific)	4.20	Gradstein et al., 2012			4.20	Wade et al., 2011
	B <i>Globorotalia crassaformis</i> sensu lato	4.31	Gradstein et al., 2012	4.31	Lourens et al., 2004	4.30	Wade et al., 2011
PL2	T <i>Globoturborotalita nepenthes</i>	4.37	Gradstein et al., 2012	4.37	Lourens et al., 2004	4.36	Wade et al., 2011
	B <i>Globorotalia exilis</i>	4.45	Gradstein et al., 2012	4.45	Lourens et al., 2004	4.44	Wade et al., 2011
	T <i>Sphaeroidinellopsis kochi</i>	4.53	Gradstein et al., 2012	4.53	Lourens et al., 2004	4.52	Wade et al., 2011
	T <i>Globorotalia cibaensis</i>	4.60	Gradstein et al., 2012	4.61	Wade et al., 2011	4.60	Wade et al., 2011
	T <i>Globigerinoides seiglei</i>	4.72	Gradstein et al., 2012				
	Pliocene/Miocene boundary	5.33	Gradstein et al., 2012	5.33	Lourens et al., 2004	5.33	Wade et al., 2011
	B <i>Sphaeroidinella dehiscentes</i> sensu lato	5.53	Gradstein et al., 2012	5.53	Lourens et al., 2004	5.48	Wade et al., 2011
PL1	B <i>Globorotalia tumida</i> (Pacific)	5.57	Gradstein et al., 2012			5.51	Wade et al., 2011
	B <i>Turborotalita humilis</i>	5.81	Gradstein et al., 2012	5.81	Lourens et al., 2004	5.71	Wade et al., 2011
	T <i>Globoquadrina dehiscentes</i>	5.92	Gradstein et al., 2012	5.92	Wade et al., 2011	5.80	Wade et al., 2011
	B <i>Globorotalia margaritae</i>	6.08	Gradstein et al., 2012	6.08	Lourens et al., 2004	5.95	Wade et al., 2011
M14	T <i>Globorotalia languensis</i>	6.12	Gradstein et al., 2012			6.00	Wade et al., 2011
	B <i>Globigerinoides conglobatus</i>	6.20	Gradstein et al., 2012	6.2	Lourens et al., 2004	6.08	Wade et al., 2011
	X <i>Neogloboquadrina acostaensis</i> coiling sinistral to dextral	6.37	Gradstein et al., 2012	6.34	Wade et al., 2011	6.20	Wade et al., 2011
	B <i>Pulleniatina primalis</i>	6.60	Gradstein et al., 2012	6.6	Wade et al., 2011	6.40	Wade et al., 2011
	X <i>Neogloboquadrina acostaensis</i> coiling dextral to sinistral	6.77	Gradstein et al., 2012	6.77	Wade et al., 2011	6.60	Wade et al., 2011
	X <i>Neogloboquadrina atlantica</i> coiling dextral to sinistral	6.99	Gradstein et al., 2012	6.99	Wade et al., 2011	6.80	Wade et al., 2011
	B <i>Candeina nitida</i>	8.43	Gradstein et al., 2012				
M13b	B <i>Globorotalia plesiotumida</i>	8.58	Gradstein et al., 2012	8.58	Lourens et al., 2004	8.52	Wade et al., 2011
	B <i>Globigerinoides extremus</i>	8.93	Gradstein et al., 2012	8.93	Lourens et al., 2004	8.86	Wade et al., 2011
	B <i>Globorotalia cibaensis</i>	9.44	Gradstein et al., 2012	9.44	Lourens et al., 2004	9.34	Wade et al., 2011
	B <i>Globorotalia juanai</i>	9.69	Gradstein et al., 2012	9.69	Lourens et al., 2004	9.62	Wade et al., 2011

Table T2 (continued). (Continued on next page.)

Zone/subzone base	Species event	GTS2012 age (Ma)	Calibration reference	GTS2004 age (Ma)	Calibration reference	Cande and Kent (1995) age (Ma)	Calibration reference
M13a	B <i>Neogloboquadrina acostaensis</i> , (sub)tropical	9.83	Gradstein et al., 2012	9.83	Lourens et al., 2004	9.79	Wade et al., 2011
	T <i>Globorotalia challengerii</i>	9.99	Gradstein et al., 2012				
M12	T <i>Paragloborotalia mayeri/siakensis</i> , (sub)tropical	10.62	Gradstein et al., 2012			10.53	Wade et al., 2012
	B <i>Globorotalia limbata</i>	10.64	Gradstein et al., 2012	10.64	Lourens et al., 2004	10.66	Wade et al., 2011
	T <i>Cassigerinella chipolensis</i>	10.89	Gradstein et al., 2012	10.89	Lourens et al., 2004	10.84	Wade et al., 2011
	B <i>Globoturborotalita apertura</i>	11.18	Gradstein et al., 2012	11.18	Lourens et al., 2004	11.12	Wade et al., 2011
	B <i>Globorotalia challengerii</i>	11.22	Gradstein et al., 2012				
	B regular <i>Globigerinoides obliquus</i>	11.25	Gradstein et al., 2012				
	B <i>Globoturborotalita decoraperta</i>	11.49	Gradstein et al., 2012	11.49	Lourens et al., 2004	11.42	Wade et al., 2011
	T <i>Globigerinoides subquadratus</i>	11.54	Gradstein et al., 2012	11.54	Lourens et al., 2004	11.46	Wade et al., 2011
M11	B <i>Globoturborotalita nepenthes</i>	11.63	Gradstein et al., 2012	11.63	Lourens et al., 2004	11.55	Wade et al., 2011
M10	T <i>Fohsella fohsi</i> , <i>Fohsella plexus</i>	11.79	Gradstein et al., 2012	11.79	Lourens et al., 2004	11.71	Wade et al., 2011
	T <i>Globorotalia praescitula</i>	12.02	Gradstein et al., 2012			11.90	Wade et al., 2011
	T <i>Clavatorella bermudezi</i>	12.00	Gradstein et al., 2012				
	B <i>Globorotalia languanensis</i>	12.84	Gradstein et al., 2012	12.84	Lourens et al., 2004	12.89	Wade et al., 2011
	B <i>Sphaeroidinellopsis subdehiscens</i>	13.02	Gradstein et al., 2012	13.02	Lourens et al., 2004	13.00	Wade et al., 2011
M9b	B <i>Fohsella robusta</i>	13.13	Gradstein et al., 2012	13.13	Lourens et al., 2004	13.09	Wade et al., 2011
	T <i>Cassigerinella martinez picoi</i>	13.27	Gradstein et al., 2012	13.27	Lourens et al., 2004	13.22	Wade et al., 2011
M9a	B <i>Fohsella fohsi</i>	13.41	Gradstein et al., 2012	13.41	Lourens et al., 2004	13.34	Wade et al., 2011
	B <i>Neogloboquadrina nympha</i>	13.49	Gradstein et al., 2012				
M8	B <i>Fohsella praefohsi</i>	13.77	Gradstein et al., 2012	13.77	Lourens et al., 2004	13.74	Wade et al., 2011
	T <i>Fohsella peripheroronda</i>	13.80	Gradstein et al., 2012	13.8	Lourens et al., 2004	13.77	Wade et al., 2011
	T regular <i>Clavatorella bermudezi</i>	13.82	Gradstein et al., 2012	13.82	Lourens et al., 2004	13.79	Wade et al., 2011
	T <i>Globorotalia archeomenardii</i>	13.87	Gradstein et al., 2012	13.87	Lourens et al., 2004	13.84	Wade et al., 2011
M7	B <i>Fohsella peripheroacuta</i>	14.24	Gradstein et al., 2012	14.24	Lourens et al., 2004	14.23	Wade et al., 2011
	B <i>Globorotalia praemenardii</i>	14.38	Gradstein et al., 2012	14.38	Lourens et al., 2004	14.39	Wade et al., 2011
	T <i>Praeorbulina sicana</i>	14.53	Gradstein et al., 2012	14.53	Lourens et al., 2004	14.56	Wade et al., 2011
	T <i>Globigeriantella insueta</i>	14.66	Gradstein et al., 2012	14.66	Lourens et al., 2004	14.69	Wade et al., 2011
	T <i>Praeorbulina glomerosa sensu stricto</i>	14.78	Gradstein et al., 2012				
	T <i>Praeorbulina circularis</i>	14.89	Gradstein et al., 2012				
M6	B <i>Orbulina suturalis</i>	15.10	Gradstein et al., 2012	15.1	Wade et al., 2011	15.10	Wade et al., 2011
	B <i>Clavatorella bermudezi</i>	15.73	Gradstein et al., 2012	15.73	Wade et al., 2011	15.76	Wade et al., 2011
	B <i>Praeorbulina circularis</i>	15.96	Gradstein et al., 2012	15.96	Wade et al., 2011	16.00	Wade et al., 2011
	B <i>Globigerinoides diminutus</i>	16.06	Gradstein et al., 2012				
	B <i>Globorotalia archeomenardii</i>	16.26	Gradstein et al., 2012	16.26	Lourens et al., 2004	16.29	Wade et al., 2011
M5b	B <i>Praeorbulina glomerosa sensu stricto</i>	16.27	Gradstein et al., 2012	16.27	Lourens et al., 2004	16.29	Wade et al., 2011
	B <i>Praeorbulina curva</i>	16.28	Gradstein et al., 2012	16.28	Wade et al., 2011	16.30	Wade et al., 2011
M5a/M4b	B <i>Praeorbulina sicana</i>	16.38	Gradstein et al., 2012	16.38	Wade et al., 2011	16.40	Wade et al., 2011
	T <i>Globorotalia incognita</i>	16.39	Gradstein et al., 2012				
M4b	B <i>Fohsella birnageae</i>	16.69	Gradstein et al., 2012	16.69	Wade et al., 2011	16.70	Wade et al., 2011
	B <i>Globorotalia miozea</i>	16.70	Gradstein et al., 2012				
	B <i>Globorotalia zealandica</i>	17.26	Gradstein et al., 2012	17.26	Wade et al., 2011	17.30	Wade et al., 2011
	T <i>Globorotalia semivera</i>	17.26	Gradstein et al., 2012				
M4a	T <i>Catapsydrax dissimilis</i>	17.54	Gradstein et al., 2012	17.54	Lourens et al., 2004	17.62	Wade et al., 2011
	B <i>Globigeriantella insueta sensu stricto</i>	17.59	Gradstein et al., 2012	17.59	Lourens et al., 2004	17.69	Wade et al., 2011
	B <i>Globorotalia praescitula</i>	18.26	Gradstein et al., 2012	18.26	Wade et al., 2011	18.50	Wade et al., 2011
	T <i>Globoquadrina binaiensis</i>	19.09	Gradstein et al., 2012	19.09	Lourens et al., 2004	19.43	Wade et al., 2011
M3	B <i>Globigerinatella</i> sp.	19.30	Gradstein et al., 2012	19.3	Lourens et al., 2004	19.66	Wade et al., 2011
	B <i>Globoquadrina binaiensis</i>	19.30	Gradstein et al., 2012				
	B <i>Globigerinoides altiapertura</i>	20.03	Gradstein et al., 2012	20.03	Wade et al., 2011	20.50	Wade et al., 2011
	T <i>Tenuitella munda</i>	20.78	Gradstein et al., 2012	20.78	Wade et al., 2011	21.40	Wade et al., 2011
	B <i>Globorotalia incognita</i>	20.93	Gradstein et al., 2012				
	T <i>Globoturborotalita angulisuturalis</i>	20.94	Gradstein et al., 2012	20.94	Wade et al., 2011	21.60	Wade et al., 2011
M2	T <i>Paragloborotalia kugleri</i>	21.12	Gradstein et al., 2012	21.12	Lourens et al., 2004	21.81	Wade et al., 2011
	T <i>Paragloborotalia pseudokugleri</i>	21.31	Gradstein et al., 2012	21.31	Lourens et al., 2004	22.04	Wade et al., 2011
	B <i>Globoquadrina dehiscens</i> forma <i>spinosa</i>	21.44	Gradstein et al., 2012				

Table T2 (continued). (Continued on next page.)

Zone/subzone base	Species event	GTS2012 age (Ma)	Calibration reference	GTS2004 age (Ma)	Calibration reference	Cande and Kent (1995) age (Ma)	Calibration reference
	T <i>Dentoglobigerina globularis</i>	21.98	Gradstein et al., 2012				
M1b	B <i>Globoquadrina dehiscentis</i>	22.44	Gradstein et al., 2012	22.44	Wade et al., 2011	23.20	Wade et al., 2011
	T <i>Globigerina ciperoensis</i>	22.90	Gradstein et al., 2012	22.9	Lourens et al., 2004	23.68	Wade et al., 2011
	B <i>Globigerinoides trilobus</i> sensu lato	22.96	Gradstein et al., 2012	22.96	Lourens et al., 2004	23.73	Wade et al., 2011
M1a	B <i>Paragloborotalia kugleri</i>	22.96	Gradstein et al., 2012	22.96	Lourens et al., 2004	23.73	Wade et al., 2011
	Miocene/Oligocene boundary	23.03	Gradstein et al., 2012	23.03	Lourens et al., 2004	23.80	Berggren et al., 1995
	T <i>Globigerina euapertura</i>	23.03	Gradstein et al., 2012				
	T <i>Tenuitella gemma</i>	23.50	Gradstein et al., 2012	23.6	Wade et al., 2011	24.30	Wade et al., 2011
	B common <i>Globigerinoides primordius</i>	23.50	Gradstein et al., 2012	23.6	Wade et al., 2011	24.30	Wade et al., 2011
O7	B <i>Paragloborotalia pseudokugleri</i>	25.21	Gradstein et al., 2012	25.4	Wade et al., 2011	25.90	Wade et al., 2011
	B <i>Globigerinoides primordius</i>	26.12	Gradstein et al., 2012	26.3	Wade et al., 2011	26.70	Wade et al., 2011
O6	T <i>Paragloborotalia opima</i> sensu stricto	26.93	Gradstein et al., 2012	27.3	Wade et al., 2011	27.50	Wade et al., 2011
O5	T common <i>Chiloguembelina cubensis</i>	28.09	Gradstein et al., 2012	28.3	Wade et al., 2011	28.40	Wade et al., 2011
O4	B <i>Globigerina angulituralis</i>	29.18	Gradstein et al., 2012	29.5	Wade et al., 2011	29.40	Wade et al., 2011
	B <i>Tenuitellinata juvenilis</i>	29.50	Gradstein et al., 2012				
	T <i>Subbotina angiporoides</i>	29.84	Gradstein et al., 2012	30.1	Wade et al., 2011	30.00	Wade et al., 2011
O3	T <i>Turborotalia ampliapertura</i>	30.28	Gradstein et al., 2012	30.4	Wade et al., 2011	30.30	Wade et al., 2011
	B <i>Paragloborotalia opima</i>	30.72	Gradstein et al., 2012	30.8	Wade et al., 2011	30.60	Wade et al., 2011
O2	T <i>Pseudohastigerina naguwichiensis</i>	32.10	Gradstein et al., 2012	32.2	Wade et al., 2011	32.00	Wade et al., 2011
O1	B <i>Cassigerinella chipolensis</i>	33.89	Gradstein et al., 2012				
O1	Oligocene/Eocene boundary	33.89	Gradstein et al., 2012	33.7	Berggren et al., 1995	33.70	Berggren et al., 1995
	T <i>Hantkenina</i> spp., <i>Hantkenina alabamensis</i>	33.89	Gradstein et al., 2012	33.9	Wade et al., 2011	33.70	Wade et al., 2011
	T common <i>Pseudohastigerina micra</i>	33.89	Gradstein et al., 2012	33.9	Wade et al., 2011	33.70	Wade et al., 2011
	T <i>Turborotalia cerroazulensis</i>	34.03	Gradstein et al., 2012	34	Wade et al., 2011	33.80	Wade et al., 2011
	T <i>Cribohantkenina inflata</i>	34.22	Gradstein et al., 2012				
E16	T <i>Globigerinatheka index</i>	34.61	Gradstein et al., 2012	34.5	Wade et al., 2011	34.30	Wade et al., 2011
	T <i>Turborotalia pomeroli</i>	35.66	Gradstein et al., 2012				
	B <i>Turborotalia cunialensis</i>	35.71	Gradstein et al., 2012	35.4	Wade et al., 2011	35.30	Wade et al., 2011
	B <i>Cribohantkenina inflata</i>	35.87	Gradstein et al., 2012				
E15	T <i>Globigerinatheka semiinvoluta</i>	36.18	Gradstein et al., 2012	35.8	Wade et al., 2011	35.80	Wade et al., 2011
	T <i>Acarinina</i> spp.	37.75	Gradstein et al., 2012				
	T <i>Subbotina linaperta</i>	37.96	Gradstein et al., 2012				
	T <i>Acarinina collactea</i>	37.96	Gradstein et al., 2012				
E14	T <i>Morozovelloides crassatus</i>	38.25	Gradstein et al., 2012	37.7	Wade et al., 2011	38.00	Wade et al., 2011
	B <i>Globigerinatheka semiinvoluta</i>	38.62	Gradstein et al., 2012	37.7	Wade et al., 2011	38.00	Wade et al., 2011
	T <i>Acarinina mcgowrani</i>	38.62	Gradstein et al., 2012	37.7	Wade et al., 2011	38.00	Wade et al., 2011
	T <i>Planorotalites</i> spp.	38.62	Gradstein et al., 2012				
	T <i>Acarinina primitiva</i>	39.12	Gradstein et al., 2012				
	T <i>Turborotalia frontosa</i>	39.42	Gradstein et al., 2012	38.8	Wade et al., 2011	39.30	Wade et al., 2011
E13	T <i>Orbulinoides beckmanni</i>	40.03	Gradstein et al., 2012	39.4	Wade et al., 2011	40.00	Wade et al., 2011
E12	B <i>Orbulinoides beckmanni</i>	40.49	Gradstein et al., 2012	39.8	Wade et al., 2011	40.50	Wade et al., 2011
	T <i>Acarinina bullbrookii</i>	40.49	Gradstein et al., 2012	39.8	Wade et al., 2011	40.50	Wade et al., 2011
E11	T <i>Guembeltrioides nuttalli</i>	~42.07	Gradstein et al., 2012	~41.4	Wade et al., 2011	~42.30	Wade et al., 2011
	B <i>Turborotalia pomeroli</i>	42.21	Gradstein et al., 2012	41.5	Wade et al., 2011	42.40	Wade et al., 2011
	B <i>Globigerinatheka index</i>	42.64	Gradstein et al., 2012	41.9	Wade et al., 2011	42.90	Wade et al., 2011
	B <i>Morozovelloides lehneri</i>	43.15	Gradstein et al., 2012	42.5	Wade et al., 2011	43.50	Wade et al., 2011
E10	T <i>Morozovella aragonensis</i>	43.26	Gradstein et al., 2012	42.6	Wade et al., 2011	43.60	Wade et al., 2011
E9	B <i>Globigerinatheka kugleri</i>	~43.88	Gradstein et al., 2012	~43.4	Wade et al., 2011	~44.40	Wade et al., 2011
	B <i>Hantkenina singanoae</i>	~44.49	Gradstein et al., 2012	43.5	Wade et al., 2011	44.50	Wade et al., 2011
	B <i>Turborotalia possagnoensis</i>	45.49	Gradstein et al., 2012				
E8	B <i>Guembeltrioides nuttalli</i> (common)	45.86	Gradstein et al., 2012	45.5	Wade et al., 2011	46.40	Wade et al., 2011
	B <i>Morozovelloides crassatus</i>	47.89	Luciani and Giusberti, 2014				
E7b	B <i>Turborotalia frontosa</i>	48.31	Gradstein et al., 2012	48.6	Wade et al., 2011	49.00	Wade et al., 2011
	B <i>Pseudohastigerina micra</i>	49.15	Luciani and Giusberti, 2014				

Table T2 (continued). (Continued on next page.)

Zone/subzone base	Species event	GTS2012 age (Ma)	Calibration reference	GTS2004 age (Ma)	Calibration reference	Cande and Kent (1995) age (Ma)	Calibration reference
	T <i>Planorotalites palmerae</i>	50.11	Luciani and Giusberti, 2014				
E7a	B <i>Planorotalites palmerae</i>	50.20	Luciani and Giusberti, 2014	50.3	Wade et al., 2011	50.40	Wade et al., 2011
	B <i>Acarinina mcgowrani</i>	50.25	Luciani and Giusberti, 2014				
	B <i>Acarinina bullbrookii</i>	50.38	Luciani and Giusberti, 2014				
	T <i>Morozovella formosa</i>	50.46	Luciani and Giusberti, 2014				
	B <i>Acarinina pentacamerata</i>	50.67	Luciani and Giusberti, 2014				
E6	T <i>Morozovella subbotinae</i>	50.67	Gradstein et al., 2012	50.8	Wade et al., 2011	50.80	Wade et al., 2011
	B <i>Acarinina cuneicamerata</i>	51.81	Luciani and Giusberti, 2014	50.3	Wade et al., 2011	50.40	Wade et al., 2011
	B <i>Guembeltrioides nuttalli</i> (rare)	52.49	Luciani and Giusberti, 2014				
	B <i>Acarinina primitiva</i>	52.72	Luciani and Giusberti, 2014				
	T <i>Morozovella marginodentata</i>	52.85	Gradstein et al., 2012	52.8	Wade et al., 2011	52.50	Wade et al., 2011
	T <i>Morozovella lensiformis</i>	53.14	Gradstein et al., 2012	53.1	Wade et al., 2011	52.70	Wade et al., 2011
E5	B <i>Morozovella aragonensis</i>	53.39	Luciani and Giusberti, 2014	52.3	Wade et al., 2011	52.30	Wade et al., 2011
	T <i>Morozovella gracilis</i>	53.39	Luciani and Giusberti, 2014				
	T <i>Morozovella aequa</i>	54.20	Gradstein et al., 2012	54	Wade et al., 2011	53.60	Wade et al., 2011
E4	B <i>Morozovella formosa</i>	54.61	Gradstein et al., 2012	54.4	Wade et al., 2011	54.00	Wade et al., 2011
	B <i>Morozovella lensiformis</i>	54.61	Gradstein et al., 2012	54.4	Wade et al., 2011	54.00	Wade et al., 2011
	T <i>Subbotina velascoensis</i>	55.07	Gradstein et al., 2012				
E3	T <i>Morozovella velascoensis</i>	~55.20	Gradstein et al., 2012	54.9	Wade et al., 2011	54.50	Wade et al., 2011
	T <i>Morozovella acuta</i>	55.39	Gradstein et al., 2012	55.1	Wade et al., 2011	54.70	Wade et al., 2011
	B <i>Morozovella gracilis</i>	55.39	Gradstein et al., 2012	55.1	Wade et al., 2011	54.70	Wade et al., 2011
	B <i>Igorina broedermanni</i>	55.39	Gradstein et al., 2012	55.1	Wade et al., 2011	54.70	Wade et al., 2011
	B <i>Morozovella marginodentata</i>	55.54	Gradstein et al., 2012	55.2	Wade et al., 2011	54.80	Wade et al., 2011
E2	B <i>Pseudohastigerina wilcoxensis</i>	55.81	Gradstein et al., 2012	55.7	Wade et al., 2011	55.40	Wade et al., 2011
	B <i>Globanomalina australiformis</i>	55.96	Gradstein et al., 2012	55.8	Wade et al., 2011	55.50	Wade et al., 2011
E1	B <i>Acarinina sibaiyaensis</i>	55.96	Gradstein et al., 2012	55.8	Wade et al., 2011	55.50	Wade et al., 2011
	Eocene/Paleocene boundary	55.96	Gradstein et al., 2012	55.8	Wade et al., 2011	55.50	Ouda and Aubry, 2003
P5	T <i>Globanomalina pseudomenardii</i>	57.10	Gradstein et al., 2012	56.7	Wade et al., 2011	55.90	Wade et al., 2011
	B <i>Morozovella subbotinae</i>	57.10	Gradstein et al., 2012	56.7	Wade et al., 2011	55.90	Wade et al., 2011
	T <i>Acarinina mckannai</i>	57.66	Gradstein et al., 2012	57.1	Wade et al., 2011	56.30	Wade et al., 2011
	T <i>Acarinina acarinata</i>	57.66	Gradstein et al., 2012	57.1	Wade et al., 2011	56.30	Wade et al., 2011
P4c	B <i>Acarinina soldadoensis</i>	57.79	Gradstein et al., 2012	57.3	Wade et al., 2011	56.50	Wade et al., 2011
	B <i>Acarinina coalingensis</i>	57.79	Gradstein et al., 2012	57.3	Wade et al., 2011	56.50	Wade et al., 2011
	B <i>Morozovella aequa</i>	57.79	Gradstein et al., 2012	57.3	Wade et al., 2011	56.50	Wade et al., 2011
	T <i>Acarinina subsphaerica</i>	58.44	Gradstein et al., 2012	57.9	Wade et al., 2011	57.10	Wade et al., 2011
	B <i>Acarinina mckannai</i>	60.43	Gradstein et al., 2012	59.9	Wade et al., 2011	59.10	Wade et al., 2011
P4b	T <i>Parasubbotina variospira</i>	60.52	Gradstein et al., 2012	60	Wade et al., 2011	59.20	Wade et al., 2011
	B <i>Acarinina acarinata</i>	60.52	Gradstein et al., 2012	60	Wade et al., 2011	59.20	Wade et al., 2011
	B <i>Acarinina subsphaerica</i>	60.52	Gradstein et al., 2012	60	Wade et al., 2011	59.20	Wade et al., 2011
P4a	B <i>Globanomalina pseudomenardii</i>	60.73	Gradstein et al., 2012	60.2	Wade et al., 2011	59.40	Wade et al., 2011
P3b	B <i>Igorina albeari</i>	61.33	Gradstein et al., 2012	60.8	Wade et al., 2011	60.00	Wade et al., 2011
	B <i>Morozovella velascoensis</i>	61.33	Gradstein et al., 2012	60.8	Wade et al., 2011	60.00	Wade et al., 2011
	B <i>Acarinina strabocella</i>	61.77	Gradstein et al., 2012				
	B <i>Morozovella conicotruncata</i>	62.22	Gradstein et al., 2012	61.7	Wade et al., 2011	60.90	Wade et al., 2011
P3a	B <i>Morozovella angulata</i>	62.29	Gradstein et al., 2012	61.7	Wade et al., 2011	61.00	Wade et al., 2011
	B <i>Igorina pusilla</i>	62.29	Gradstein et al., 2012	61.7	Wade et al., 2011	61.00	Wade et al., 2011
	B <i>Morozovella praeangulata</i>	62.46	Gradstein et al., 2012	61.9	Wade et al., 2011	61.20	Wade et al., 2011
	B <i>Globanomalina imitata</i>	62.54	Gradstein et al., 2012	~62	Wade et al., 2011	~61.30	Wade et al., 2011
P2	B <i>Praemurica uncinata</i>	62.60	Gradstein et al., 2012	62.1	Wade et al., 2011	61.40	Wade et al., 2011
P1c	B <i>Globanomalina compressa</i>	63.90	Gradstein et al., 2012	63.5	Wade et al., 2011	62.90	Wade et al., 2011
	B <i>Praemurica inconstans</i>	63.90	Gradstein et al., 2012	63.5	Wade et al., 2011	62.90	Wade et al., 2011

Table T2 (continued).

Zone/subzone base	Species event	GTS2012 age (Ma)	Calibration reference	GTS2004 age (Ma)	Calibration reference	Cande and Kent (1995) age (Ma)	Calibration reference
	B <i>Parasubbotina varianta</i>	64.02	Gradstein et al., 2012	63.6	Wade et al., 2011	63.00	Wade et al., 2011
P1b	B <i>Subbotina trilocolinoides</i>	65.25	Gradstein et al., 2012	64.7	Wade et al., 2011	64.30	Wade et al., 2011
P1a	T <i>Parvularugoglobigerina eugubina</i>	65.72	Gradstein et al., 2012	65.2	Wade et al., 2011	64.80	Wade et al., 2011
	B <i>Parasubbotina pseudobulloides</i>	65.76	Gradstein et al., 2012				
	B <i>Parvularugoglobigerina extensa</i>	65.94	Gradstein et al., 2012	65.4	Wade et al., 2011	64.90	Wade et al., 2011
Pa	B <i>Parvularugoglobigerina eugubina</i>	66.00	Gradstein et al., 2012	65.46	Wade et al., 2011	64.97	Wade et al., 2011
	Cretaceous/Paleogene boundary	66.04	Gradstein et al., 2012	65.5	Wade et al., 2011		
P0	T <i>Globotruncana</i> spp., <i>Racemiguembelina fructicosa</i> ; tops of other Cretaceous foraminifers	66.04	Gradstein et al., 2012	65.5	Wade et al., 2011	65.00	Wade et al., 2011
<i>Plummerita hantkeninoides</i>	T <i>Abathomphalus mayaroensis</i>	66.35	Gradstein et al., 2012				
	T <i>Gansserina gansseri</i>	~66.49	Gradstein et al., 2012				
	T <i>Contusotruncana patelliformis</i>	66.72	Gradstein et al., 2012				
<i>Pseudoguembelina hariaensis</i>	B <i>Pseudoguembelina hariaensis</i>	67.30	Gradstein et al., 2012				
	T <i>Abathomphalus intermedia</i>	67.33	Gradstein et al., 2012				
	T <i>Globotruncana linneiana</i>	68.37	Gradstein et al., 2012				
	T <i>Globotruncana bulloides</i>	68.82	Gradstein et al., 2012				
	T <i>Rugoglobigerina pennyi</i>	68.86	Gradstein et al., 2012				
	T <i>Contusotruncana fornicata</i>	69.13	Gradstein et al., 2012				
<i>Abathomphalus mayaroensis</i>	B <i>Abathomphalus mayaroensis</i>	69.18	Gradstein et al., 2012				
	T <i>Pseudotextularia elegans</i>	69.55	Gradstein et al., 2012				
	T <i>Planoglobulina acervulinoides</i>	~70.05	Gradstein et al., 2012				
<i>Racemiguembelina fructicosa</i>	B <i>Racemiguembelina fructicosa</i>	~70.14	Gradstein et al., 2012				
	T <i>Globotruncana ventricosa</i>	~70.14	Gradstein et al., 2012				
	B <i>Globotruncana lapparenti</i> , <i>Globotruncana linneiana</i>	70.90	Gradstein et al., 2012				
	B <i>Contusotruncana contusa</i>	~71.01	Gradstein et al., 2012				
	B <i>Racemiguembelina powelli</i>	71.47	Gradstein et al., 2012				
<i>Pseudoguembelina palpebra</i>	B <i>Pseudoguembelina palpebra</i>	71.75	Gradstein et al., 2012				
	B <i>Pseudoguembelina kempensis</i>	71.97	Gradstein et al., 2012				
	Maastrichtian/Campanian boundary	72.05	Gradstein et al., 2012				
<i>Gansserina gansseri</i>	B <i>Gansserina gansseri</i>	~72.97	Gradstein et al., 2012				
	B <i>Planoglobulina acervulinoides</i>	~72.97	Gradstein et al., 2012				
<i>Globotruncana aegyptiaca</i>	B <i>Globotruncana aegyptiaca</i>	~74.00	Gradstein et al., 2012				
	B <i>Pseudoguembelina excolata</i>	~74.00	Gradstein et al., 2012				
<i>Globotruncanella havanensis</i>	T <i>Radotruncana calcarata</i>	75.71	Gradstein et al., 2012				
	B <i>Pseudotextularia elegans</i>	~75.71	Gradstein et al., 2012				
	B <i>Globotruncanella havanensis</i>	~75.94	Gradstein et al., 2012				
<i>Radotruncana calcarata</i>	B <i>Radotruncana calcarata</i>	76.18	Gradstein et al., 2012				
	B <i>Globotruncana ventricosa</i> (consistent)	77.66	Gradstein et al., 2012				
	T <i>Archaeoglobigerina bosquensis</i>	77.79	Gradstein et al., 2012				
<i>Contusotruncana plummerae</i>	B <i>Contusotruncana plummerae</i>	~79.20	Gradstein et al., 2012				
	B <i>Globotruncana ventricosa</i> (rare)	~79.90	Gradstein et al., 2012				
	B <i>Pseudoguembelina costulata</i>	81.96	Gradstein et al., 2012				
	T <i>Ventilabrella eggeri</i>	82.71	Gradstein et al., 2012				
	T <i>Marginotruncana coronata</i>	82.89	Gradstein et al., 2012				
	T <i>Whiteinella baltica</i>	83.08	Gradstein et al., 2012				
<i>Globotruncanita elevata</i>	B <i>Globotruncanita elevata</i>	83.64	Gradstein et al., 2012				
	Campanian/Santonian boundary	~83.64	Gradstein et al., 2012				

Table T3. Age estimates of diatom datum events, Expedition 353. FO = first occurrence, LO = last occurrence, LCO = last common occurrence, AC = acme. ? = noncalibrated ages. (Continued on next page.) [Download table in .csv format.](#)

Bioevent	Age (Ma)	Biozone	Biozone abbreviation	Calibration reference
LO <i>Nitzschia fossilis</i>	0.44–0.58	<i>Fragilariopsis doliolus</i>	NTD17	Fourtanier, 1991a
LCO <i>Nitzschia fossilis</i>	0.83–0.90	<i>Fragilariopsis doliolus</i>	NTD17	Fourtanier, 1991a
LO <i>Nitzschia reinholdii</i>	0.90–1.0	<i>Nitzschia reinholdii</i> / <i>Fragilariopsis doliolus</i>	NTD16/NTD17	Fourtanier, 1991a
LCO <i>Nitzschia reinholdii</i>	1.0–1.28	<i>Nitzschia reinholdii</i>	NTD16	Fourtanier, 1991a
LO <i>Rhizosolenia praebergonii</i> var. <i>robusta</i>	1.49–1.60	<i>Nitzschia reinholdii</i>	NTD16 a/b	Fourtanier, 1991a
LO <i>Rhizosolenia praebergonii</i>	1.49–1.60	<i>Nitzschia reinholdii</i>	NTD16 a/b	Fourtanier, 1991a
AC <i>Shionodiscus oestrupii</i>	1.7	<i>Nitzschia reinholdii</i>	NTD16	Mikkelsen, 1990
FO <i>Fragilariopsis doliolus</i>	1.8	<i>Rhizosolenia praebergonii</i> / <i>Nitzschia reinholdii</i>	NTD15/NTD16	Mikkelsen, 1990
LO <i>Thalassiosira convexa</i>	2.5	<i>Rhizosolenia praebergonii</i>	NTD15 b/c	Mikkelsen, 1990
LO <i>Thalassiosira convexa</i> var. <i>aspinosa</i>	2.50–2.51	<i>Rhizosolenia praebergonii</i>	NTD15	Fourtanier, 1991a
LO <i>Nitzschia jouseae</i>	2.6	<i>Rhizosolenia praebergonii</i>	NTD15 a/b	Mikkelsen, 1990
FO <i>Rhizosolenia praebergonii</i>	3	<i>Nitzschia jouseae</i> / <i>Rhizosolenia praebergonii</i>	NTD14/NTD15	Barron, 1985b
AC <i>Thalassiosira convexa</i> var. <i>aspinosa</i>	3.3	<i>Nitzschia jouseae</i>	NTD14	Mikkelsen, 1990
FO <i>Thalassiosira convexa</i> var. <i>convexa</i>	3.6	<i>Nitzschia jouseae</i>	NTD14	Barron, 1985b
FO <i>Asteromphalus elegans</i>	3.9	<i>Nitzschia jouseae</i>	NTD14	Barron, 1985b
LO <i>Nitzschia cylindrica</i>	4.35	<i>Nitzschia jouseae</i>	NTD14	Barron, 1985b
FO <i>Nitzschia jouseae</i>	4.6	<i>Thalassiosira convexa</i> / <i>Nitzschia jouseae</i>	NTD13/NTD14	Mikkelsen, 1990
LO <i>Thalassiosira miocenica</i>	5.05	<i>Thalassiosira convexa</i>	NTD13 b/c	Barron, 1985b
FO <i>Shionodiscus oestrupii</i>	5.3	<i>Thalassiosira convexa</i>	NTD13	Mikkelsen, 1990
LO <i>Nitzschia miocenica</i>	5.7	<i>Thalassiosira convexa</i>	NTD13	Barron, 1985b
LO <i>Thalassiosira praeconvexa</i>	5.9	<i>Thalassiosira convexa</i>	NTD13 a/b	Barron, 1985b
FO <i>Nitzschia fossilis</i>	6.1	<i>Nitzschia miocenica</i> / <i>Thalassiosira convexa</i>	NTD12/NTD13	Mikkelsen, 1990
FO <i>Thalassiosira convexa</i> var. <i>aspinosa</i>	6.1	<i>Nitzschia miocenica</i> / <i>Thalassiosira convexa</i>	NTD12/NTD13	Mikkelsen, 1990
FO <i>Thalassiosira miocenica</i>	6.15	<i>Nitzschia miocenica</i>	NTD12	Barron, 1985b
FO <i>Thalassiosira praeconvexa</i>	6.35	<i>Nitzschia miocenica</i>	NTD12 a/b	Barron, 1985b
FO <i>Nitzschia miocenica</i>	7.35	<i>Nitzschia porteri</i> / <i>Nitzschia miocenica</i>	NTD11/NTD12	Barron, 1985b
LO <i>Rossiella paleacea</i>	7.45	<i>Nitzschia porteri</i>	NTD11	Barron, 1985b
LO <i>Thalassiosira burckliana</i>	~7.85	<i>Nitzschia porteri</i>	NTD11 a/b	Barron, 1985b
LO <i>Thalassiosira yabei</i>	8.6	<i>Thalassiosira yabei</i> / <i>Nitzschia porteri</i>	NTD10/NTD11	Barron, 1985b
FO <i>Thalassiosira burckliana</i>	9.1	<i>Thalassiosira yabei</i>	NTD10 a/b	Barron, 1985b
LO <i>Thalassiosira yabei</i> var. <i>elliptica</i>	9.4	<i>Thalassiosira yabei</i>	NTD10	Mikkelsen, 1990
FO <i>Thalassiosira yabei</i> var. <i>elliptica</i>	9.7	<i>Thalassiosira yabei</i>	NTD10	Mikkelsen, 1990
LO <i>Coscinodiscus vetustissimus</i> var. <i>javanica</i>	10.6	<i>Thalassiosira yabei</i>	NTD10	Barron, 1985b
FO <i>Coscinodiscus vetustissimus</i> var. <i>javanica</i>	11.1	<i>Thalassiosira yabei</i>	NTD10	Barron, 1985b
LCO <i>Denticulopsis hustedtii</i>	11.3	<i>Thalassiosira yabei</i>	NTD10	Barron, 1985b
LO <i>Actinocyclus moronensis</i>	11.4	<i>Actinocyclus moronensis</i> / <i>Thalassiosira yabei</i>	NTD9/NTD10	Barron, 1985b
LO <i>Azpeitia apiculata</i>	11.9	<i>Actinocyclus moronensis</i>	NTD9	Barron, 1985b
LO <i>Denticulopsis punctata</i> var. <i>hustedtii</i>	12.1	<i>Craspedodiscus coscinodiscus</i> / <i>Actinocyclus moronensis</i>	NTD8/NTD9	Barron, 1985b
LO <i>Craspedodiscus coscinodiscus</i>	~12.1	<i>Craspedodiscus coscinodiscus</i> / <i>Actinocyclus moronensis</i>	NTD8/NTD9	Barron, 1985b
FO <i>Hemidiscus cuneiformis</i>	12.5	<i>Craspedodiscus coscinodiscus</i>	NTD8	Barron, 1985b
FO <i>Coscinodiscus temperei</i> var. <i>delicata</i>	12.7	<i>Coscinodiscus giga</i> var. <i>diorama</i> / <i>Craspedodiscus coscinodiscus</i>	NTD7/NTD8	Barron, 1985b
LO <i>Coscinodiscus lewiasianus</i>	~13.5	<i>Coscinodiscus lewiasianus</i> / <i>Coscinodiscus giga</i> var. <i>diorama</i>	NTD6/NTD7	Barron, 1985b
LO <i>Cestodiscus peplum</i>	14	<i>Cestodiscus peplum</i> / <i>Coscinodiscus lewiasianus</i>	NTD5/NTD6	Barron, 1985b
LO <i>Azpeitia apiculata</i>	14.1	<i>Cestodiscus peplum</i>	NTD5	Barron, 1985b
LO <i>Annellus californicus</i>	~14.8	<i>Cestodiscus peplum</i>	NTD5 a/b	Barron, 1985b
FO <i>Cestodiscus peplum</i>	~16	<i>Denticulopsis nicobarica</i> / <i>Cestodiscus peplum</i>	NTD4/NTD5	Barron, 1985b
LO <i>Thalassiosira bukryi</i>	~16.6	<i>Denticulopsis nicobarica</i>	NTD4 a/b	Barron, 1985b
FO <i>Denticulopsis nicobarica</i>	~17.5	<i>Triceratium pileus</i> / <i>Denticulopsis nicobarica</i>	NTD3/NTD4	Barron, 1985b
LO <i>Craspedodiscus elegans</i>	18.7	<i>Craspedodiscus elegans</i> / <i>Triceratium pileus</i>	NTD2/NTD3	Fourtanier, 1991a
LO <i>Bogorovia veniamini</i>	19.9	<i>Rossiella paleacea</i> / <i>Craspedodiscus elegans</i>	NTD1/NTD2	Fourtanier, 1991a
LO <i>Azpeitia oligocena</i>	~20.5	<i>Rossiella paleacea</i>	NTD1 b/c	Barron, 1985b
FO <i>Rossiella paleacea</i>	22.7	<i>Rocella gelida</i> / <i>Rossiella palacea</i>		Fourtanier, 1991a
LO <i>Rocella gelida</i>	24.2	<i>Rocella gelida</i>		Barron et al., 2004
LO <i>Thalassiosira primalabiata</i>	~25	<i>Rossiella paleacea</i>	NTD1 a/b	Barron, 1985b
FO <i>Rocella gelida</i>	25.8	<i>Bogorovia veniamini</i> / <i>Rocella gelida</i>		Barron et al., 2004
FO <i>Bogorovia veniamini</i>	26.5	<i>Rocella vigilans</i> / <i>Bogorovia veniamini</i>		Fourtanier, 1991a
LO <i>Triceratium pileus</i>	?			Barron, 1985b
FO <i>Triceratium pileus</i>	?			Barron, 1985b
FO <i>Rocella vigilans</i>	29.9	<i>Cestodiscus reticulatus</i> / <i>Rocella vigilans</i>		Barron et al., 2004
FO <i>Rossiella symmetrica</i>	?			Fenner, 1985
LO <i>Coscinodiscus excavatus</i>	33.6–33.5	<i>Cestodiscus reticulatus</i>		Barron et al., 2004
FO <i>Cestodiscus reticulatus</i>	~35.9	<i>Coscinodiscus excavatus</i> / <i>Cestodiscus reticulatus</i>		Fenner, 1985
FO <i>Coscinodiscus excavatus</i>	~39	<i>Baxteriopsis brunii</i> / <i>Coscinodiscus excavatus</i>		Fenner, 1985
FO <i>Baxteriopsis brunii</i>	~40	<i>Asterolampra marylandica</i> / <i>Baxteriopsis brunii</i>		Fenner, 1985
FO <i>Asterolampra marylandica</i>	~43	<i>Brightwellia imperfecta</i> / <i>Asterolampra marylandica</i>		Fenner, 1985
FO <i>Hemiaulus grassus</i>	?	<i>Pyxilla caputavis</i>		Fenner, 1985
FO <i>Brightwellia imperfecta</i>	~44.5	<i>Hemiaulus gondolaformis</i> / <i>Brightwellia imperfecta</i>		Fenner, 1985
FO <i>Hemiaulus gondolaformis</i>	~46.3	<i>Hemiaulus alatus</i> / <i>Hemiaulus gondolaformis</i>		Fenner, 1985
FO <i>Hemiaulus alatus</i>	~47	<i>Pyxilla caputavis</i> / <i>Hemiaulus alatus</i>		Fenner, 1985

Table T3 (continued).

Bioevent	Age (Ma)	Biozone	Biozone abbreviation	Calibration reference
FO <i>Pyxilla caputavis</i>	~47.9	<i>Triceratium kanayae</i> / <i>Pyxilla caputavis</i>		Fenner, 1985
FO <i>Triceratium kanayae</i>	~49.1	<i>Craspedodiscus oblongus</i> / <i>Triceratium kanayae</i>		Fenner, 1985
LO <i>Cestodiscus reticulatus</i>	?			Fenner, 1985
FO <i>Coscinodiscus hajosiae</i>	?	<i>Pyxilla caputavis</i>		Fenner, 1984
FO <i>Coscinodiscus oblongus</i>	~49.1	<i>Craspedodiscus undulatus</i> / <i>Craspedodiscus oblongus</i>		Fenner, 1985
FO <i>Trinacria excavata</i> f. <i>tetragona</i>	?	<i>Craspedodiscus undulatus</i>		Fenner, 1984
FO <i>Abas wittii</i>	?	<i>Craspedodiscus undulatus</i>		Fenner, 1984
FO <i>Triceratium polycystinorum</i>	?	<i>Craspedodiscus undulatus</i>		Fenner, 1984
FO <i>Pyxilla gracilis</i>	56.30–56.65	<i>Hemiaulus inaequilateralis</i>		Fourtanier, 1991b
LO <i>Hemiaulus incurvus</i>	56.65–56.80	<i>Hemiaulus inaequilateralis</i>		Fourtanier, 1991b
FO <i>Hemiaulus peripterus</i> var. <i>longispinus</i>	56.85–57.40	<i>Hemiaulus inaequilateralis</i>		Fourtanier, 1991b
LO <i>Trinacria aries</i>	57.65–57.95	<i>Hemiaulus inaequilateralis</i>		Fourtanier, 1991b
FO <i>Triceratium orbiculatum</i>	58.35–58.65	<i>Sceptroneis</i> sp. A		Fourtanier, 1991b
LO <i>Stephanopyxis biseriata</i>	~58.5	<i>Sceptroneis</i> sp. A		Fenner, 1985
LO <i>Triceratium gombosii</i> var. A	60.75–60.80	<i>Odontotropis klavensii</i>		Fourtanier, 1991b
FO <i>Triceratium gombosii</i>	61 (60.95–61.05)	<i>Odontotropis klavensii</i>		Fourtanier, 1991b
FO <i>Hemiaulus incurvus</i>	61.60–61.65	<i>Odontotropis klavensii</i>		Fourtanier, 1991b
LO <i>Hemiaulus peripterus</i> var. <i>peripterus</i>	61.75–61.85	<i>Odontotropis klavensii</i>		Fourtanier, 1991b
FO <i>Stephanopyxis biseriata</i>	~62.5	<i>Odontotropis klavensii</i>		Fenner, 1985
LO <i>Hemiaulus asymmetricus</i>	~66.5	<i>Odontotropis klavensii</i>		Fenner, 1985; Hajós, 1975
LO <i>Eunotograma fueleopi</i>	~66.5			Fenner, 1985; Hajós, 1975
LO <i>Pterotheca parvula</i>	~66.5			Fenner, 1985; Hajós, 1975
LO <i>Acanthodiscus antarticus</i>	~66.5			Fenner, 1985; Hajós, 1975
LO <i>Pseudopyxilla russica</i>	~66.5			Fenner, 1985; Hajós, 1975
LO <i>Gladius jouseanus</i>	~66.5			Fenner, 1985; Hajós, 1975
LO <i>Triceratium kuepperi</i>	~66.5			Fenner, 1985; Hajós, 1975
LO <i>Huttonia antiqua</i>	?			Hajós, 1975
LO <i>Achnatodiscus convexus</i>	?			Hajós, 1975
LO <i>Gladius pacificus</i> f. <i>minor</i>	?			Hajós, 1975
LO <i>Trinacria tristictia</i>	?			Hajós, 1975
LO <i>Gladius maximus</i>	?			Hajós, 1975
LO <i>Gladius pacificus</i>	?			Hajós, 1975
LO <i>Gladius pacificus</i>	?			Hajós, 1975
LO <i>Biddulphia cretacea</i>	?			Hajós, 1975
LO <i>Coscinodiscus ildicoi</i>	?			Hajós, 1975
LO <i>Triceratium sectum</i>	?			Hajós, 1975
LO <i>Stephanopyxis lavrenkoi</i>	?			Hajós, 1975
LO <i>Hemiaulus schmidtii</i>	?			Hajós, 1975
LO <i>Triceratium schultzi</i>	?			Hajós, 1975
LO <i>Achantodiscus ornatus</i>	?			Hajós, 1975
LO <i>Gonothecium odontella</i>	?			Hajós, 1975
LO <i>Pterotheca aculeata</i>	?			Hajós, 1975
LO <i>Gonothecium odontella</i>	?			Hajós, 1975
LO <i>Pterotheca aculeata</i>	?			Hajós, 1975
LO <i>Trinacria incipiens</i>	?			Hajós, 1975
LO <i>Cerataulina cretacea</i>	?			Hajós, 1975

Indian Ocean (Fourtanier 1991a, 1991b; Mikkelsen, 1990) (Figure F4A, F4B).

Several taxonomic studies of diatoms preserved in low-latitude Indian Ocean sediments are available. For identification of diatoms to the lowest possible taxonomic level, we mainly followed Strelnikova (1974), Hajós (1975), Fenner (1984, 1985), Barron (1980, 1983, 1985a, 1985b), and Harwood (1988).

Methods of study for diatoms

Smear slides of all core catchers were prepared by placing a small amount of raw sediment onto a slide and allowing the water to evaporate by heating on a hot plate for ~5 min. About 1–2 drops of NOA 61 was applied to the dry slide, which was then covered with a 22 mm × 30 mm glass coverslip. The adhesive was solidified by placing the slide under UV light for ~10 min. In addition, slides of silty mud sediments from split core sections were prepared when expected to be diatomaceous. Smear slides were partially examined at

400× and/or 630× magnification for stratigraphic markers and other common taxa using a Zeiss Axioplan microscope. When needed, 1000× magnification was used to identify some smaller taxa.

Total abundance of diatoms and the species composition of the preserved diatom assemblage were determined for all slides. Total diatom abundance in the sediment was assessed following Koç and Scherer (1996) using the following criteria:

- D = dominant (>60% valves).
- A = abundant (~20%–60% valves).
- C = common (~5%–20% valves).
- F = few (2%–5% valves).
- R = rare (<2% valves).
- B = barren (no diatoms present).

Relative abundances of each diatom taxon, as reported in range charts, were estimated using the following qualitative scale:

- A = abundant (>10 valves/FOV).
 C = common (1–10 valves/FOV).
 F = few (≥ 1 valve/10 FOVs and <1 valve/FOV).
 R = rare (≥ 3 valves/traverse of coverslip and <1 valve/10 FOVs).
 X = present (<3 valves/traverse of coverslip, including fragments).
 B = barren (no valves).

Diatom preservation categories, as reported in range charts, are described qualitatively following Barron and Gladenkov (1995):

- VG = very good (no breakage or dissolution).
 G = good (majority of specimens complete, with minor dissolution and/or breakage and no significant enlargement of the areolae or dissolution of frustule rims detected; the sample generally has a high diatoms/g concentration).
 M = moderate (minor but common areolae enlargement and dissolution of frustule rims, with a considerable amount of breakage of specimens).
 P = poor (strong dissolution or breakage, some specimens unidentifiable, strong dissolution of frustule rims and areolae enlargement; the sample generally has lower diatoms/g concentration).

Geochemistry

The shipboard geochemistry program characterized the gases, pore fluids, and sediment composition of the cores. Headspace and void samples were analyzed for routine shipboard safety and pollution prevention purposes. Interstitial water chemistry and sedimentary carbonate and organic carbon content were analyzed to understand the depositional history of the sediments and help direct shore-based sampling and research.

Sedimentary gases

Routine analysis of hydrocarbon gas in sediment cores is a part of standard IODP shipboard monitoring to ensure that the sediments being drilled do not contain more than the amount of hydrocarbons that is safe for drilling operations. The most common method of hydrocarbon monitoring used during IODP expeditions is the analysis of gas samples obtained from either sediment samples (headspace analysis) or from gas expansion pockets visible through clear plastic core liners (void gas analysis). When gas pockets were encountered, free gas was drawn from the sediment void using a syringe attached to a hollow stainless steel tool used to puncture the core liner as described by Kvenvolden and McDonald (1986). For headspace analyses, a 3 cm³ bulk sediment sample was collected immediately after core retrieval from the freshly exposed top end of a core section next to the interstitial water sample using a brass boring tool or plastic syringe. The sediment plug was placed in a glass vial and sealed with an aluminum crimp cap with Teflon/silicone septa. The vial was then heated to 70°C for ~30 min to evolve hydrocarbon gases from the sediment plug before analysis. When consolidated or lithified samples were encountered, chips of material were placed in the vial and sealed. For gas chromatographic analysis, a 5 cm³ volume of headspace gas was extracted from the sealed sample vial using a standard gas syringe and analyzed by gas chromatography.

Headspace samples were directly injected into the Agilent/Hewlett Packard 6890 Series II gas chromatograph (GC3) fitted with a flame ionization detector (FID) or the natural gas analyzer (NGA).

The GC3 is equipped with an 8 ft (2.00 mm inner diameter [ID]; ½ inch OD) stainless steel column packed with 80/100 mesh HayeSep (Restek) and an FID set at 250°C. The GC3 oven temperature was programmed to hold for 8.25 min at 80°C, ramp at 40°C/min to 150°C, hold for 5 min, and return to 100°C post-run, for a total run time of 15 min. Helium was used as the carrier gas. The GC3 system determines concentrations of methane (C₁), ethane (C₂), ethene (C₂₌), propane (C₃), and propene (C₃₌). For hydrocarbon analysis, the NGA is outfitted with an Agilent 7890 GC equipped with an Agilent DB-1 dimethylpolysiloxane capillary column (60 m × 0.320 mm diameter × 1.50 µm film thickness) fitted with an FID and using He as carrier gas (constant flow of 21 mL/min). The NGA oven temperature was programmed to hold for 2 min at 50°C, ramp at 8°C/min to 70°C, and then ramp at 25°C/min to 200°C, with a final holding time of 5.1 min. The FID temperature was 250°C. For non-hydrocarbon gases, thermal conductivity detector (TCD) separation used three columns: a 6 ft × 2.0 mm ID stainless steel column (Poropak T; 50/80 mesh), a 3 ft × 2.0 mm ID stainless steel molecular sieve column (13X; 60/80 mesh), and a 2.4 m × 3.2 mm ID stainless steel column packed with 80/100 mesh HayeSep.

The Agilent Chemstation data processing program used peak areas of C₁–C₃ hydrocarbons of interest to calculate the relative abundances.

Interstitial water collection

For pore fluid analyses, whole-round cores were cut on the catwalk, capped, and taken to the laboratory for processing. In general, samples were processed under normal atmospheric conditions. For some sites and samples, cores were processed inside a nitrogen bag to avoid oxidation of redox-sensitive elements. During high-resolution sampling, when the capacity to process pore fluid samples immediately after retrieval was exceeded, capped whole-round core sections were stored under a nitrogen atmosphere until they were squeezed, which occurred within 6 h of core retrieval.

After extrusion from the core liner, the surface of each whole-round interstitial water core sample was carefully scraped with a spatula to remove potential contamination from seawater and sediment smearing in the borehole. In APC cores, ~0.5 cm of material from the OD and the top and bottom faces was removed. The remaining sediment (~150–300 cm³) was placed into a titanium squeezer, modified after the stainless steel squeezer of Manheim and Sayles (1974). Gauge forces up to a maximum of 25,000 lb were applied using a laboratory hydraulic press to extract pore water. Most samples were squeezed at <15,000 lb.

The squeezed pore fluids were filtered through a prewashed Whatman No. 1 filter placed in the squeezers above a titanium screen. The squeezed pore fluids were filtered into a precleaned plastic syringe attached to the squeezing assembly and then through a 0.2 µm polysulfone disc filter.

Shipboard interstitial water analyses

Pore fluid samples were analyzed on board the ship following the protocols in Gieskes et al. (1991), Murray et al. (2000), and the IODP user manuals for new shipboard instrumentation.

Salinity, alkalinity, and pH

Salinity, alkalinity, and pH were measured immediately after squeezing, following the procedures in Gieskes et al. (1991). Salinity was measured using a Fisher temperature-compensated handheld refractometer. pH was measured with a combined glass electrode,

and alkalinity was determined by Gran titration with an autotitrator (Metrohm 794 basic Titrino) using 0.1 M HCl at 20°C. International Association for the Physical Sciences of the Oceans (IAPSO) standard seawater was used for calibration and was analyzed, at least, at the beginning and end of a set of samples for each site.

Chloride

High-precision chloride concentrations were acquired using a Metrohm 785 DMP autotitrator and silver nitrate (AgNO₃) solution calibrated against repeated titrations of an IAPSO standard. A 0.5 mL aliquot of sample was diluted with 10 mL of 90 ± 2 mM HNO₃ and titrated with 0.1778 M AgNO₃. Repeated analyses of an IAPSO standard yielded a precision better than 0.05%.

Sulfate

Pore fluid SO₄ concentrations were measured by ion chromatography using the Dionex ICS-3000.

Ammonium and phosphate

Ammonium concentrations were determined by spectrophotometry using an Agilent Technologies Cary Series 100 UV-visible spectrophotometer with a sipper sample introduction system following the protocol in Gieskes et al. (1991). Samples were diluted prior to color development so that the highest concentration was <1000 µM. Phosphate was measured using the ammonium molybdate method described in Gieskes et al. (1991), using appropriate dilutions.

Major and minor elements

Major and minor elements were analyzed by inductively coupled plasma–atomic emission spectroscopy (ICP-AES) with a Teledyne Prodigy high-dispersion ICP spectrometer. Major elements were also measured by ion chromatography using the Dionex ICS-3000. The general method for shipboard ICP-AES analysis of samples is described in ODP Technical Note 29 (Murray et al., 2000) and the user manuals for shipboard instrumentation. Multiple wavelengths were measured for each element, and the best were selected for reporting element concentrations. Wavelengths were selected based on possible interferences, the linearity of calibration

curves, and the precision and accuracy of IAPSO seawater measurements. These wavelengths were Li = 670.784 nm, B = 249.772 nm, Na = 589.592 nm, Mg = 279.553 or 285.213 nm, Si = 250.690 or 251.611 nm, K = 769.897 nm, Ca = 315.887 or 317.933 nm, Sr = 460.733 nm, and Ba = 455.403 or 493.409 nm. Absolute Si concentrations obtained for the IAPSO seawater varied from day to day, so these were adjusted to give an average value of 72 µM for the IAPSO seawater. This adjustment was not required after the torch of the ICP was changed before analyses of the samples from the last two sites. Iron and Mn are not present in IAPSO seawater at micromolar levels, so the reproducibility of standard solutions was used to select the wavelengths Fe = 239.563 or 259.940 nm and Mn = 259.372 nm. Detection limits for the minor elements, defined here as 3.3 times the standard deviation of the blank intensities converted to concentrations, are given for each analytical session in Table T4. These are multiplied by 20 to account for the required sample dilution. Samples were diluted 1:20 using 2% HNO₃ spiked with 10 ppm Y for minor element analyses (Li, B, Si, Mn, Fe, Sr, and Ba) and 1:100 for major elements (Na, K, Ca, and Mg). Measured intensities were blank corrected and, if necessary, a drift correction was applied to each element by linear interpolation between the drift-monitoring solutions.

Standardization of major cations was achieved by dilutions of IAPSO standard seawater to have 300%, 200%, 100%, 75%, 50%, 25%, and 10% IAPSO seawater in the 100× diluted solution. The results from calibration curves using slightly nonlinear intensity responses were corrected to ensure the 100% IAPSO values were near true seawater values. This was always necessary for Na but was run-dependent for the other major elements.

The high concentration of salt in the interstitial water samples at the 1:20 dilution used for minor element analysis demands matrix matching of standards and samples, so standards were prepared with a NaCl matrix solution to have an ionic strength similar to 20× diluted seawater. A stock standard solution was gravimetrically prepared from ultrapure primary standards (SPC Science PlasmaCAL) diluted in 1% HNO₃. This was diluted, along with the NaCl matrix, to have minor element concentrations bracketing the samples. Analytical precision was estimated by repeated analyses of the IAPSO

Table T4. Detection limits for ICP minor elements, Expedition 353. [Download table in .csv format.](#)

Element (wavelength, nm):	B (249.772)	Ba (455.403)	Ba (493.409)	Fe (239.563)	Fe (259.940)	Li (670.784)	Mn (259.372)	Si (250.690)	Si (251.611)	Sr (460.733)
Site U1443 minors 12 Dec 2014										
Detection limit	1.670	0.004	0.015	0.024	0.005	0.048	0.003	0.263	0.361	0.204
Detect × 20	33.41	0.082	0.302	0.476	0.103	0.959	0.067	5.267	7.222	4.084
Site U1444 minors 30 Dec 2014										
Detection limit	0.270	0.005	0.018	0.015	0.026	0.111	0.002	0.299	0.243	0.232
Detect × 20	5.403	0.110	0.356	0.298	0.512	2.217	0.049	5.974	4.853	4.633
Site U1445 minors 8 Jan 2015										
Detection limit	0.308	0.005	0.008	0.025	0.011	0.069	0.037	0.242	0.300	0.034
Detect × 20	6.163	0.107	0.157	0.496	0.219	1.389	0.746	4.837	5.995	0.671
Site U1446 minors 12 Jan 2015										
Detection limit	0.032	0.002	0.003	0.026	0.018	0.084	0.007	0.454	0.292	0.142
Detect × 20	0.648	0.050	0.057	0.520	0.351	1.686	0.132	9.084	5.834	2.847
Site U1447 minors 22 Jan 2015										
Detection limit	0.672	0.002	0.008	0.005	0.014	0.028	0.003	0.174	0.334	0.044
Detect × 20	13.45	0.033	0.162	0.109	0.283	0.552	0.068	3.475	6.681	0.883
Site U1448 minors 24 Jan 2015										
Detection limit	0.704	0.003	0.021	0.010	0.015	0.015	0.006	0.237	0.179	0.046
Detect × 20	14.08	0.058	0.424	0.196	0.309	0.303	0.127	4.730	3.584	0.920
Average detection limit (µM in sample):	12.19	0.073	0.243	0.349	0.296	1.184	0.198	5.561	5.695	2.340

Table T5. Accuracy and precision for ICP major and minor elements in IAPSO, Expedition 353. * = adjusted Si. [Download table in .csv format.](#)

Minor element (wavelength, nm):	B (249.772)	Li (670.784)	Si (251.611)	Sr (460.733)	Major element (wavelength, nm)	Ca (317.933)	K (769.897)	Mg (285.213)	Na (589.592)
Site U1443 minors 12 Dec 2014					Site U1443 majors 11 Dec 2014				
IAPSO - 1	432	25.2	70.6*	89.1	IAPSO - 1	10.2	9.68	52.6	468
IAPSO - 2	429	25.1	68.6*	91.6	IAPSO - 2	10.4	9.84	53.6	465
IAPSO - 3	433	25.5	67.7*	95.0	IAPSO - 3	10.3	9.77	53.1	468
IAPSO - 4	437	25.5	77.7*	94.4	IAPSO - 4	10.1	9.59	52.4	465
IAPSO - 5	436	25.8	73.3*	94.0	IAPSO - 5	10.3	9.71	53.2	467
Site U1444 minors 30 Dec 2014					Hole U1444A majors 29 Dec 2014				
IAPSO - 1	442	24.8	71.4*	94.3	IAPSO - 1	10.3	9.79	53.2	468
IAPSO - 2	447	23.9	74.4*	95.5	IAPSO - 2	10.3	9.68	53.2	466
IAPSO - 3	434	23.4	71.7*	94.1	IAPSO - 3	10.6	9.73	53.3	470
IAPSO - 4	429	23.6	69.3*	93.9					
IAPSO - 5	428	23.1	73.2*	91.8					
Site U1445 minors 8 Jan 2015					Site U1445 majors 7–8 Jan 2015				
IAPSO - 1	451	25.5	71.6*	92.1	IAPSO - 1	11.1	9.78	53.1	516
IAPSO - 2	453	26.9	70.2*	93.3	IAPSO - 2	10.9	9.47	51.4	507
IAPSO - 3	441	25.3	68.3*	88.7	IAPSO - 3	11.3	9.88	53.1	526
IAPSO - 4	444	25.9	67.6*	90.6	IAPSO - 4	11.2	9.55	51.7	514
IAPSO - 5	449	25.9	70.1*	90.0	IAPSO - 5	10.7	9.28	50.0	501
					IAPSO - 6	10.9	9.89	54.3	471
					IAPSO - 7	10.6	9.62	52.9	469
					IAPSO - 8	10.6	9.56	52.6	466
Site U1446 minors 12 Jan 2015					Site U1446 majors 11 Jan 2015				
IAPSO - 1	468	—	73.1	98.5	IAPSO - 1	10.1	9.60	52.1	490
IAPSO - 2	442	—	73.5	93.5	IAPSO - 2	10.3	10.06	53.4	471
IAPSO - 3	448	—	72.4	93.6	IAPSO - 3	10.1	9.56	53.4	449
IAPSO - 4	448	—	70.5	92.5	IAPSO - 4	10.3	9.81	54.2	454
IAPSO - 5	447	—	70.4	94.3	IAPSO - 5	10.4	9.72	54.8	452
Site U1447 minors 22 Jan 2015					Site U1447 majors 21 Jan 2015				
IAPSO - 1	444	23.0	74.0	92.7	IAPSO - 1	10.5	10.31	54.9	486
IAPSO - 2	448	24.2	72.5	91.5	IAPSO - 2	9.8	9.09	51.7	463
IAPSO - 3	447	23.7	73.1	90.9	IAPSO - 3	10.2	9.35	53.4	461
IAPSO - 4	451	24.5	75.0	92.2	IAPSO - 4	10.2	10.05	52.4	464
Site U1448 minors 24 Jan 2015					Site U1448 majors 24 Jan 2015				
IAPSO - 1	437	24.5	76.2	92.3	IAPSO - 1	10.2	9.58	52.8	460
IAPSO - 2	445	23.5	70.8	91.7	IAPSO - 2	10.2	9.55	52.8	460
IAPSO - 3	455	24.5	74.1	94.2	IAPSO - 3	10.1	9.66	52.3	466
					IAPSO - 4	10.2	9.68	53.1	468
					IAPSO - 5	10.3	9.62	52.9	462
Average:	443	24.70	71.91	92.82	Average:	10.4	9.68	52.9	474
2σ:	18.41	2.11	5.07	4.16	2σ:	0.72	0.48	2.02	39.4
2σ (%):	4.15	8.55	7.06	4.48	2σ (%):	6.87	4.99	3.83	8.31
N:	27	22	27	27	N:	28	28	28	28

seawater (Table T5) or repeated measurement of samples from previous sites (Table T6). Although Si ions were measured by ICP, the text refers to silicate, as we assume all dissolved (<0.2 μm) Si was present as silicic acid.

Sediment geochemistry

For shipboard sediment geochemistry, 5 cm³ of sediment was freeze-dried for ~24 h, crushed to a fine powder using an agate pestle and mortar, and sampled to analyze inorganic carbon, total carbon (TC), and total nitrogen (TN).

Elemental analysis

TC and TN contents of the sediment samples were determined with a ThermoElectron Corporation FlashEA 1112 carbon-hydrogen-nitrogen-sulfur (CHNS) elemental analyzer equipped with a ThermoElectron packed column CHNS/NCS and a TCD. Approximately 10–15 mg of freeze-dried, ground sediment was weighed into a tin cup, and the sample was combusted at 900°C in a stream of oxygen. The reaction gases were passed through a reduction chamber to reduce nitrogen oxides to nitrogen and were then sepa-

rated by the gas chromatograph before detection by TCD. All carbon content measurements were calibrated with the La Luna shale (11.52% C) reference material for samples with high carbon contents (>4%) or Thermo Soil Reference Material 33840025 for samples with low carbon content, which was run approximately every six samples for verification. Repeated ($n = 4$) analyses of the standards yielded a precision of <0.17% for TC.

Inorganic and organic carbon content

Total inorganic carbon (TIC) concentrations were determined using a UIC 5011 CO₂ coulometer. Between 10 and 12 mg of freeze-dried ground sediment was weighed and reacted with 2 M HCl. The liberated CO₂ was titrated, and the end-point was determined by a photodetector. Calcium carbonate content, expressed as weight percent, was calculated from the TIC content, assuming that all evolved CO₂ was derived from the dissolution of CaCO₃ by the following equation:

$$\text{CaCO}_3 \text{ (wt\%)} = \text{TIC} \times 8.33 \text{ (wt\%)}$$

Table T6. Accuracy and precision for ICP minor elements in samples, Expedition 353. NA = data not available. [Download table in .csv format.](#)

Element (wavelength, nm):	B (249.772)	Ba (455.403)	Ba (493.409)	Fe (239.563)	Fe (259.940)	Li (670.784)	Mn (259.372)	Si (250.690)	Si (251.611)	Sr (460.733)
Site U1444 minors 29 Dec 2014										
U1444A 3H2 AIR	416	2.98	2.84	5.89	5.95	0.99	6.26	355	404	73.4
U1444A 3H2 AIR	413	2.90	2.87	5.91	5.76	0.89	6.25	359	407	74.3
U1444A 3H2 AIR	423	3.00	2.91	6.11	5.97	0.70	6.35	363	413	75.7
Average:	417	2.96	2.87	5.97	5.89	0.86	6.29	359	408	74.5
2 σ :	9.82	0.10	0.07	0.24	0.23	0.30	0.11	7.82	9.73	2.28
2 σ (%):	2.35	3.54	2.49	3.95	3.86	34.6	1.77	2.18	2.39	3.06
Site U1445 minors 8 Jan 2015										
LIQ6216911 7 Jan 2015	556	0.55	0.47	17.0	15.8	21.8	48.5	587	956	
1445A 1H4 A	548	0.49	0.53	15.6	16.0	21.6	46.5	569	926	89.0
1445A 1H4 B	558	0.48	0.46	16.1	16.1	21.1	47.1	577	939	89.7
1445A 1H4 C	559	0.47	0.45	16.0	16.0	20.8	46.8	569	927	89.9
Average:	555	0.50	0.48	16.1	16.0	21.3	47.2	575	937	89.5
2 σ :	9.62	0.07	0.07	1.20	0.23	0.97	1.80	17.4	28.3	0.91
2 σ (%):	1.73	14.1	14.6	7.45	1.42	4.55	3.80	3.02	3.02	1.02
Site U1446 minors 12 Jan 2015										
LIQ6229881 8 Jan 2015	362	141	137	26.0	24.6	29.1	6.29	985	966	98.4
1445A 21H A	355	133	130	24.3	24.0	NA	5.69	918	946	99.5
1445A 21H B	373	138	134	25.7	25.6	NA	6.00	957	999	103
1445A 21H C	362	136	132	24.8	24.5	NA	6.00	951	999	101
Average:	362	137	133	25.2	24.7		6.00	953	978	101
2 σ :	14.7	6.07	6.43	1.61	1.34		0.48	54.6	52.5	4.49
2 σ (%):	4.04	4.43	4.82	6.38	5.43		8.09	5.73	5.37	4.45
Site U1447 minors 22 Jan 2015										
LIQ6293841 12 Jan 2015	352	76.6	78.1	37.4	37.1	NA	1.25	928	965	104
LIQ6293841 A	350	78.2	77.7	38.0	37.1	62.8	1.20	915	976	101
LIQ6293841 B	346	77.6	76.8	37.4	36.7	59.4	1.22	889	984	99.9
LIQ6293841 C	345	76.7	75.8	36.8	36.3	58.4	1.16	888	992	96.7
Average:	348	77.3	77.1	37.4	36.8	60.2	1.21	905	979	100
2 σ :	6.62	1.55	2.07	0.97	0.79	4.67	0.08	39.3	22.3	6.26
2 σ (%):	1.90	2.01	2.69	2.60	2.15	7.76	6.25	4.34	2.27	6.24
Site U1448 minors 24 Jan 2015										
LIQ6360701 22 Jan 2015	523	11.9	11.3	10.5	10.4	18.9	6.75	622	709	70.1
LIQ6360701 A	527	10.6	11.6	10.6	10.5	19.0	6.82	634	669	71.6
LIQ6360701 B	509	10.3	11.2	10.4	10.1	18.3	6.62	618	664	70.1
LIQ6360701 C	515	10.4	11.4	10.4	10.1	18.7	6.73	628	686	71.2
Average:	518	10.8	11.4	10.5	10.3	18.7	6.73	625	682	70.8
2 σ :	15.5	1.47	0.36	0.19	0.38	0.62	0.17	13.8	40.4	1.52
2 σ (%):	2.99	13.7	3.14	1.81	3.71	3.32	2.56	2.20	5.93	2.15

No correction was made for the presence of other carbonate minerals. Accuracy during individual batches of analyses was determined by running a pure carbonate CaCO₃ standard approximately every 10 samples. Typical precision assessed using 36 replicate analyses of a carbonate sample was 1%. The detection limit for CaCO₃, defined here as three times the standard deviation of the blank (2 M HCl), was 0.1% for 100 mg of pelagic clay. Total organic carbon (TOC) content was calculated as the difference between TC (measured on the elemental analyzer) and inorganic carbon (measured by coulometry):

$$\text{TOC} = \text{TC} - \text{inorganic carbon.}$$

For samples with very low organic carbon the “acidification method” of TOC analysis was also applied to examine improving analytical precision. Freeze-dried samples weighed (~30 mg) into precombusted silver capsules were treated with small aliquots (10 μ L) of concentrated HCl at room temperature to remove CaCO₃; samples were treated with repeated aliquots until no further reaction was visible and then dried in an oven at 60°C. Please note that

tin capsules are not appropriate for this purpose. TOC concentration was determined using a Thermo Electron Flash EA 1112 element analyzer for TC, calibrated using the Thermo Reference Material 33840025 (TOC = 2.26%).

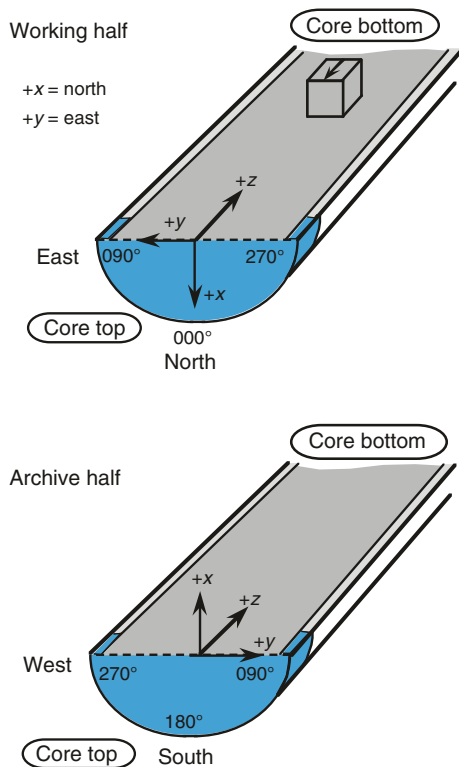
Paleomagnetism

The paleomagnetism team identified temporal variations in the ancient geomagnetic field vector in order to develop an age model for Expedition 353 sediment cores. By measuring changes in magnetic polarity (direction of geomagnetic field) for each core, magnetic polarity chrons were identified and the magnetostratigraphy defined. Outside of magnetostratigraphy, the paleomagnetists also carried out several rock magnetic experiments to characterize the mineral magnetic assemblage.

Paleomagnetic methodology

Standard IODP paleomagnetic measurement conventions were used to express orientations for Expedition 353 core samples. The positive x -axis is vertical upward from the split face of the archive

Figure F5. Schematic of archive- and working-half core orientations, Expedition 353.



half of the core. The positive y -axis is left facing upcore along the split surface of the archive half, whereas the positive z -axis is down-core (Figure F5). For APC cores, corrections for geographic orientation were reconstructed using data from either the FlexIT tool or the Icefield MI-5 tool mounted above the core barrel.

Split core measurements of magnetic remanence were performed with a 2G Enterprises pass-through cryogenic superconducting quantum interference device (SQUID) rock magnetometer. This magnetometer is equipped with an in-line alternating field (AF) demagnetizer (2G model 2G600) that allows for demagnetization of samples up to 80 mT. A nominal sample area of 15.59 cm² was used throughout the expedition, and tray speed was chosen at 10 cm/s. Each archive half was measured in continuous mode at 1–10 cm intervals, where natural remanent magnetization was measured first, followed by remanent magnetization after 5–20 mT AF demagnetization. An alternating field was applied to the x -, y -, and z -axes in this fixed order. The AF demagnetization level chosen to eliminate viscous remanent magnetization and drilling-induced remanence was based upon full AF demagnetization analyses of representative discrete samples (7 cm³ plastic cubes). Discrete samples were taken at intervals dictated by core recovery and scientific interest from the working half at each site, typically from Hole A. Remanence measurements for discrete samples were performed on either the cryogenic magnetometer or an AGICO JR-6A spinner magnetometer. Stepwise AF demagnetization was performed using either the in-line AF demagnetizer of the cryogenic magnetometer or an ASC Scientific D-2000 AF demagnetizer to full demagnetization, or until a remanence component decreasing toward origin was visually confirmed. Because the in-line AF demagnetizer on the *JOIDES Resolution* is known to impart a small artificial remanence, as far as time permitted, we used the D-2000 demagnetizer for dis-

crete samples. In demagnetization using the D-2000, an AF field was applied to the z -, y -, and x -axes in this fixed order. Full demagnetization results were analyzed by principal component analysis to isolate characteristic remanent magnetization (ChRM) (Kirschvink, 1980). For other samples, the endpoints were assumed to represent the ChRM directions.

Rock magnetic experiments were performed on selected discrete samples after demagnetization when time permitted. An hysteretic remanent magnetization (ARM) was acquired on discrete samples using the D-2000 AF demagnetizer by applying a decaying AF from a peak of 80 mT superimposed by a constant direct current field of 0.05 mT. Isothermal remanent magnetization (IRM) was acquired on discrete samples using an ASC Scientific Pulse magnetizer at fields of 100 and 300 mT. An assumed saturation isothermal remanent magnetization (SIRM) was further acquired at 1000 mT. The acquired laboratory remanences were measured on the JR-6 spinner magnetometer. S -ratios were calculated from both the IRM_{100mT} and IRM_{300mT} normalized by SIRM (S_{100} and S_{300} , respectively). Hard isothermal remanent magnetization was calculated as the difference in remanence between SIRM and IRM_{300mT} normalized by 2.

Magnetostratigraphy

Based upon the paleomagnetic measurements, we divided cores into intervals with constant polarity (magnetostratigraphic polarity zones or magnetozones). For shipboard interpretations, we defined the magnetozone boundaries as middle depths between stable magnetozones, which in turn were determined visually or calculated by depth uncertainty between points. Magnetostratigraphy for each site was constructed by correlating obtained magnetozones with the GPTS (Gradstein et al., 2012), which is derived by astronomical tuning of polarity boundary ages for the Neogene, and by a composite of astronomical tuning and radiometric dating for the Paleogene (Figure F4; Table T7). In some cases, defining paleomagnetic polarity and magnetostratigraphy from magnetic measurements alone was difficult, and biostratigraphic age constraints were incorporated to place magnetozones within the GPTS.

Whenever possible, we offered an interpretation of the magnetic polarity, following the naming convention of correlative anomaly numbers prefaced by the letter C (Tauxe et al., 1983). Subchrons are referred to using suffixes (e.g., 1n, 2r, etc.) that increase with age. For the younger part of the timescale (Pliocene–Pleistocene), we also used traditional names to refer to the various chrons and subchrons (e.g., Brunhes, Jaramillo, Olduvai, etc.). In general, polarity reversals occurring at core ends were treated with extreme caution because of the edge effects caused by coring-related disruptions.

Laboratory issues

The shipboard y -axis SQUID in the cryogenic magnetometer has a known “flux jump” issue, where readings jump during measurements, resulting in erroneous values. Although some previous Expedition Reports relate this flux jump to a specific lithology, during Expedition 353 we found no clear relationship to sediment type, moisture content, or sea condition. Instead, the problem seemed to depend on the condition of certain cores and liners. Often, sections in specific cores suffered from frequent flux jumps even when remeasured multiple times. Placing a small layer of polystyrene between the tray and the section sometimes prevented the occurrence of flux jumps. In any case, the mechanism remains unclear.

Table T7. Geomagnetic polarity timescale used during Expedition 353. Ages are based on the GTS2012 (Gradstein et al., 2012). [Download table in .csv format.](#)

Polarity chron	Top (Ma)	Base (Ma)	Polarity chron	Top (Ma)	Base (Ma)	Polarity chron	Top (Ma)	Base (Ma)
C1n (Brunhes)	0.000	0.781	C5Ar.2r	12.770	12.829	C9n	26.42	27.44
C1r.1r (Matuyama)	0.781	0.988	C5Ar.2n	12.829	12.887	C9r	27.44	27.86
C1r.1n (Jaramillo)	0.988	1.072	C5Ar.3r	12.887	13.032	C10n.1n	27.86	28.09
C1r.2r	1.072	1.173	C5AAn	13.032	13.183	C10n.1r	28.09	28.14
C1r.2n (Cobb Mountain)	1.173	1.185	C5AAr	13.183	13.363	C10n.2n	28.14	28.28
C1r.3r	1.185	1.778	C5ABn	13.363	13.608	C10r	28.28	29.18
C2n (Olduvai)	1.778	1.945	C5ABr	13.608	13.739	C11n.1n	29.18	29.48
C2r.1r	1.945	2.128	C5ACn	13.739	14.070	C11n.1r	29.48	29.53
C2r.1n (Reunion)	2.128	2.148	C5ACr	14.070	14.167	C11n.2n	29.53	29.97
C2r.2r	2.148	2.581	C5ADn	14.167	14.609	C11r	29.97	30.59
C2An.1n (Gauss)	2.581	3.032	C5ADr	14.609	14.775	C12n	30.59	31.03
C2An.1r (Kaena)	3.032	3.116	C5Bn.1n	14.775	14.870	C12r	31.03	33.16
C2An.2n	3.116	3.207	C5Bn.1r	14.870	15.032	C13n	33.16	33.71
C2An.2r (Mammoth)	3.207	3.330	C5Bn.2n	15.032	15.160	C13r	33.71	35.00
C2An.3n (Gauss)	3.330	3.596	C5Bn.2r	15.160	15.974	C15n	35.00	35.29
C2Ar (Gilbert)	3.596	4.187	C5Cn.1n	15.974	16.268	C15r	35.29	35.71
C3n.1n (Cochiti)	4.187	4.300	C5Cn.1r	16.268	16.303	C16n.1n	35.71	35.89
C3n.1r	4.300	4.493	C5Cn.2n	16.303	16.472	C16n.1r	35.89	36.05
C3n.2n (Nunivak)	4.493	4.631	C5Cn.2r	16.472	16.543	C16n.2n	36.05	36.70
C3n.2r	4.631	4.799	C5Cn.3n	16.543	16.721	C16r	36.70	36.97
C3n.3n (Sidufjall)	4.799	4.896	C5Cr	16.721	17.235	C17n.1n	36.97	37.75
C3n.3r	4.896	4.997	C5Dn	17.235	17.533	C17n.1r	37.75	37.87
C3n.4n (Thvera)	4.997	5.235	C5Dr.1r	17.533	17.717	C17n.2n	37.87	38.09
C3r	5.235	6.033	C5Dr.1n	17.717	17.740	C17n.2r	38.09	38.16
C3An.1n	6.033	6.252	C5Dr.2r	17.740	18.056	C17n.3n	38.16	38.33
C3An.1r	6.252	6.436	C5En	18.056	18.524	C17r	38.33	38.62
C3An.2n	6.436	6.733	C5Er	18.524	18.748	C18n.1n	38.62	39.63
C3Ar	6.733	7.140	C6n	18.748	19.722	C18n.1r	39.63	39.70
C3Bn	7.140	7.212	C6r	19.722	20.040	C18n.2n	39.70	40.14
C3Br.1r	7.212	7.251	C6An.1n	20.040	20.213	C18r	40.14	41.15
C3Br.1n	7.251	7.285	C6An.1r	20.213	20.439	C19n	41.15	41.39
C3Br.2r	7.285	7.454	C6An.2n	20.439	20.709	C19r	41.39	42.30
C3Br.2n	7.454	7.489	C6Ar	20.709	21.083	C20n	42.30	43.43
C3Br.3r	7.489	7.528	C6AAn	21.083	21.159	C20r	43.43	45.72
C4n.1n	7.528	7.642	C6AAr.1r	21.159	21.403	C21n	45.72	47.35
C4n.1r	7.642	7.695	C6AAr.1n	21.403	21.483	C21r	47.35	48.57
C4n.2n	7.695	8.108	C6AAr.2r	21.483	21.659	C22n	48.57	49.34
C4r.1r	8.108	8.254	C6AAr.2n	21.659	21.688	C22r	49.34	50.63
C4r.1n	8.254	8.300	C6AAr.3r	21.688	21.767	C23n.1n	50.63	50.83
C4r.2r	8.300	8.771	C6Bn.1n	21.767	21.936	C23n.1r	50.83	50.96
C4An	8.771	9.105	C6Bn.1r	21.936	21.992	C23n.2n	50.96	51.83
C4Ar.1r	9.105	9.311	C6Bn.2n	21.992	22.268	C23r	51.83	52.62
C4Ar.1n	9.311	9.426	C6Br	22.268	22.564	C24n.1n	52.62	53.07
C4Ar.2r	9.426	9.647	C6Cn.1n	22.564	22.754	C24n.1r	53.07	53.20
C4Ar.2n	9.647	9.721	C6Cn.1r	22.754	22.902	C24n.2n	53.20	53.27
C4Ar.3r	9.721	9.786	C6Cn.2n	22.902	23.03	C24n.2r	53.27	53.42
C5n.1n	9.786	9.937	C6Cn.2r	23.03	23.23	C24n.3n	53.42	53.98
C5n.1r	9.937	9.984	C6Cn.3n	23.23	23.30	C24r	53.98	57.10
C5n.2n	9.984	11.056	C6Cr	23.30	23.96	C25n	57.10	57.66
C5r.1r	11.056	11.146	C7n.1n	23.96	24.00	C25r	57.66	58.96
C5r.1n	11.146	11.188	C7n.1r	24.00	24.11	C26n	58.96	59.24
C5r.2r	11.188	11.592	C7n.2n	24.11	24.47	C26r	59.24	62.22
C5r.2n	11.592	11.657	C7r	24.47	24.76	C27n	62.22	62.52
C5r.3r	11.657	12.049	C7An	24.76	24.98	C27r	62.52	63.49
C5An.1n	12.049	12.174	C7Ar	24.98	25.10	C28n	63.49	64.67
C5An.1r	12.174	12.272	C8n.1n	25.10	25.26	C28r	64.67	64.96
C5An.2n	12.272	12.474	C8n.1r	25.26	25.30	C29n	64.96	65.69
C5Ar.1r	12.474	12.735	C8n.2n	25.30	25.99			
C5Ar.1n	12.735	12.770	C8r	25.99	26.42			

During transit to the first site, we found that the amplifier connected to the D-2000 AF demagnetizer had a problem; when both Channels A and B of the amplifier were used, the demagnetizer gave significant artificial remanence, possibly an ARM caused by frequency mismatch of the two channels. We decided to use only Channel B, and, consequently, we limited the maximum AF demagnetization field to 80 mT. Another issue throughout the expedition was that the D-2000 controller would stop responding during either AF demagnetization or ARM acquisition, although a field would

persist within the coil. Once the controller came back on, the field rapidly ramped to near-zero rather than at the specified slew rate. From our experience, regularly shutting down the software, the controller and the amplifier sometimes reduced the number of failed runs. Also, continually recommunicating every 3–4 demagnetization runs via the “diagnostic” feature in the software sometimes cleared the problem. However, the ultimate cause of this problem was not identified.

Physical properties

High-resolution physical property measurements were made during Expedition 353 to provide information on (1) the bulk physical character and (2) the acoustic and elastic parameters of recovered sediments. Such data enhance our understanding of the physico-chemical context and history for oceanic deposits, augment lithologic characterization, and facilitate the correlation of downhole logging data with discrete core measurements and core descriptions. Physical property data can be measured quickly in contrast to isotopic ratios and grain-size distributions and, as such, serve as important first-order proxies for determining changes in environmental conditions, geological processes, and/or depositional environments. Shipboard physical property data play a key role in the following tasks:

- Hole-to-hole correlation for construction of composite stratigraphic sections;
- Detection of discontinuities and inhomogeneities, either caused naturally or by the drilling process;
- Identification of differences in the composition and texture of sediments;
- Time-series analysis for detection of orbital cycles and tuning to reference cores for stratigraphic purposes;
- Calculation of sedimentation rates;
- Core-log-seismic integration;
- Identification of major seismic reflectors and construction of synthetic seismic profiles; and
- Input parameters for testing climate models.

Physical properties were first measured on whole-round core sections. Two logging systems were used to analyze core sections immediately following cutting on the catwalk: (1) the STMSL and (2) the WRMSL. The STMSL houses a GRA bulk densitometer and a MS sensor loop. The WRMSL employs, in order, a GRA bulk densitometer, a MS sensor loop, and a compressional *P*-wave velocity sensor. Downhole logging devices cannot measure sediments in the uppermost 80–100 m of a hole because the drill string is left in the hole for tool reentry and to retain hole stability; thus data from the WRMSL is used to supplement the downhole log data. Following WRMSL scanning, whole-round sections were equilibrated to laboratory ambient temperature and then logged through the NGRL, which generates spectral gamma ray data.

Discrete samples were collected from the working halves, primarily from Hole A, to measure wet bulk density, dry bulk density, water content, porosity, and grain density with moisture and density (MAD) procedures. Holes B and C were only sampled for MAD measurements if there were extensive gaps in the Hole A sample series, if unusual sediments were recovered in Holes B and C with no equivalent in Hole A, or if an interval in Hole A was to be cross-validated. Automated vane shear strength measurements on split cores were also taken for Hole A. Archive halves were measured with the SHMSL for color reflectance (via an Ocean Optics sensor) and MS using a discrete point-source Bartington probe. A full discussion of all methodologies and calculations used aboard the *JOIDES Resolution* in the Physical Properties laboratory is available in Blum (1997). Finally, based on significant changes in physical properties the data sets are divided into multiple units. These units (labeled 1, 2, etc.) are not necessarily same as the lithostratigraphic units (labeled I, II, etc). Physical property classifications are intended to help in identifying sediment packages with distinctly different physical behavior.

STMSL and WRMSL

High-resolution STMSL and WRMSL GRA (GRA porosity evaluation) bulk density and MS data were collected for shipboard core-to-core correlation between drill holes and constructing composite stratigraphic sections. The time required for these measurements depended on the spatial sampling interval set on the instrument. Therefore, the sampling interval was chosen such that both tasks were completed within a reasonable time, yielding the most relevant information and not encumbering the downstream core processing and sample collection. The quality of STMSL and WRMSL data was highly dependent on the structural integrity of the sediment (cracks, voids, biscuiting, etc.) and the presence of gaps between the sediment and the core liner. GRA bulk density and MS were measured nondestructively on all whole-round core sections. *P*-wave velocity was also measured nondestructively and until the acoustic signal disappeared from high attenuation, which typically occurs in sections undisturbed by gas expansion voids and cracks.

Gamma ray attenuation bulk density

Bulk density is a function of water-saturated porosity and grain density (dominant mineralogy) and is influenced by grain packing and coring disturbance. To measure bulk density, the GRA densitometer uses a 10 mCi ¹³⁷Cs capsule as a gamma ray source (with the principal energy peak at 0.662 MeV) and a scintillation detector. The narrow collimated peak is attenuated as it passes through the center of the core. Incident photons are scattered by the electrons of the sediment by Compton scattering.

The attenuation of the incident intensity (I_0) is directly related to the electron density in the sediment core of diameter (D) that can be related to bulk density given the average attenuation coefficient (in micrometers) of the sediment (Evans, 1965; Harms and Choquette, 1965). Because the attenuation coefficient is similar for most common minerals and aluminum, bulk density is acquired through direct calibration of the densitometer using aluminum rods of different diameters mounted in a core liner filled with distilled water.

Magnetic susceptibility

MS is a measure of the degree to which a material can be magnetized by an external magnetic field. It provides information on the magnetic mineral composition of the sediment that commonly can be related to changes in the mineralogical assemblage (e.g., flux of terrigenous material, biogenic mineral formation, in situ diagenesis, or postdepositional alteration). Magnetite and other iron oxides/oxyhydroxides or iron sulfides with ferromagnetic (*senso lato*) characteristics have a specific MS several orders of magnitude higher than, for example, clay, which has paramagnetic properties. Carbonate layers, opal, water, and plastic (core liner) have small negative values of MS due to diamagnetism. Calcareous and biogenic deposits with low clay and iron-bearing mineral debris content thus have values approaching the detection limit of MS instruments found on board.

MS was measured on the WRMSL and STMSL with a Bartington Instruments MS2C system. The loops were operated at different frequencies so that they did not interfere with one another when used concurrently. A correction factor of 1.282 was applied to the MS data collected by the STMSL. The output of the MS sensors can be set to centimeter-gram-second (cgs) units or SI units (IODP standard). To derive dimensionless SI volume-specific MS values, the instrument units stored in the IODP database must be multiplied by a correction factor (0.68) to compensate for instrument

scaling and the geometric ratio between core and loop dimensions (Blum, 1997).

Compressional *P*-wave velocity

P-wave velocity varies with the material's lithology, porosity, bulk density, state of stress, temperature, fabric, and/or degree of fracturing. In sediments and rocks, velocity is controlled by the degree of consolidation and lithification, fracturing, and occurrence/abundance of free gas and gas hydrates.

The *P*-wave velocity sensor measures the ultrasonic *P*-wave velocity of the whole-round sediment sample residing in the core liner. The *P*-wave logger transmits a 500 kHz *P*-wave pulse across the core section at a specified repetition rate. Traveltime is determined by signal processing software that automatically detects the first arrival of the *P*-wave signal to a precision of 50 ns. Ultrasonic *P*-wave velocity is calculated after correcting for system propagation delay, liner thickness, and liner material velocity.

Natural gamma radiation

The NGRL measures gamma rays emitted from whole-round core sections. Gamma rays detected by the logger arise primarily from the decay of U, Th, and K isotopes. In general, high counts identify fine-grained deposits containing K-rich clay minerals and their associated U and Th atoms.

The main NGR detector unit consists of 8 sodium iodide (NaI) scintillator detectors surrounding the lower half of the section, 7 shielding plastic scintillator detectors, 22 photomultipliers, and passive lead shielding. The NaI detectors are covered by at least 8 cm of lead shielding. In addition, lead separators (~7 cm of low-background lead) are positioned between the NaI detectors. Half of the lead shielding closest to the NaI detectors is composed of low-background lead, whereas the outer half is composed of common lead. In addition to this passive lead shielding, the overlying plastic scintillators detect incoming high-energy gamma and muon cosmic radiation and cancel this signal from the total counted by the NaI detectors.

A measurement run generally consisted of counting one position on each core section for 12 min, for a total of 8 measurements per 150 cm section. For analyses, "Position 2" was commonly chosen to avoid analyzing the disturbed uppermost part of the first section of each core. Therefore, NGR logging required ~80 min of measurement time per core with an additional ~10 min for core, software, and data handling. Further information may be found in Vasiliev et al. (2011) and Dunlea et al. (2013).

Moisture and density

Discrete samples were collected to determine wet and dry bulk density, grain density, water content, salt content, and porosity. In soft sediment, ~12 cm³ samples were collected with a 2 cm diameter plastic syringe that fits into the top of a 10 cm³ volume glass vial, allowing for the vial to be filled completely with sediment. To accommodate the large volume of sediment cored, as well as the Rhizon experiments that require MAD data, three MAD samples were taken and measured per core (usually at 5–7 cm in Sections 2, 4, and 6). For Rhizon sampling, MAD samples were collected in consultation with the chemistry laboratory.

Samples were placed in numbered/labeled, preweighed 16 mL Wheaton glass vials for wet and dry sediment mass measurements. The sediment samples were dried in a convective oven for 24 h, allowed to cool for 3 h, and then subjected to dry volume measurements. The weights of wet and dry sample masses were determined

to a precision of 0.005 g using two Mettler Toledo electronic balances and a computer averaging system to compensate for the ship's motion. Dry sample volume was determined using a hexapycnometer system of a 6-celled, custom-configured Micromeritics AccuPyc 1330TC helium-displacement pycnometer. The precision of each cell is <1% of the full-scale volume when properly calibrated and operated. Volume measurements were preceded by three purges of the sample chamber with helium warmed to ~28°C. Three measurement cycles were run for each sample. A reference volume (calibration sphere) was placed sequentially in one of the six chambers to check for instrument drift and systematic error. The volumes of the numbered Wheaton vials were calculated before the cruise by multiplying each vial's weight against the average density of the vial glass. Dry mass and volume were measured after samples were heated in an oven at 105° ± 5°C for 24 h and allowed to cool in a desiccator. The procedures for the determination of these physical properties comply with the American Society for Testing and Materials (ASTM) designation (D) 2216 (ASTM International, 1990). The fundamental relation and assumptions for the calculations of all MAD physical property parameters are discussed by Blum (1997) and summarized below.

Mass and volume calculation

Wet mass (M_{wet}), dry mass (M_{dry}), and dry volume (V_{dry}) were measured in the laboratory. The ratio of mass (rm) is a computational constant of 0.965 (i.e., 0.965 g of freshwater per 1 g of seawater). Salt precipitated in sediment pores during the drying process is included in the M_{dry} and V_{dry} values. The mass of the evaporated water (M_{water}) and salt (M_{salt}) in the sample are given by

$$M_{\text{water}} = M_{\text{wet}} - M_{\text{dry}}, \text{ and}$$

$$M_{\text{salt}} = M_{\text{water}}[s/(1 - s)],$$

where s is the assumed saltwater salinity (0.035%) corresponding to a pore water density (ρ_{pw}) of 1.024 g/cm³ and a salt density (ρ_{salt}) of 2.22 g/cm³. The corrected mass of pore water (M_{pw}), volume of pore water (V_{pw}), mass of solids excluding salt (M_{solid}), volume of salt (V_{salt}), volume of solids excluding salt (V_{solid}), and wet volume (V_{wet}) are

$$M_{\text{pw}} = (M_{\text{wet}} - M_{\text{dry}})/\text{rm},$$

$$V_{\text{pw}} = M_{\text{pw}}/\rho_{\text{pw}},$$

$$M_{\text{solid}} = M_{\text{wet}} - M_{\text{pw}},$$

$$M_{\text{salt}} = M_{\text{pw}} - (M_{\text{wet}} - M_{\text{dry}}),$$

$$V_{\text{salt}} = M_{\text{salt}}/\rho_{\text{salt}},$$

$$V_{\text{wet}} = V_{\text{dry}} - V_{\text{salt}} + V_{\text{pw}}, \text{ and}$$

$$V_{\text{solid}} = V_{\text{wet}} - V_{\text{pw}}.$$

Calculation of bulk properties

For all sediment samples, water content (w) is expressed as the ratio of mass of pore water to wet sediment (total) mass,

$$w = M_{\text{pw}}/M_{\text{wet}}.$$

Wet bulk density (ρ_{wet}), dry bulk density (ρ_{dry}), sediment grain density (ρ_{solid}), porosity (ϕ), and void ratio (VR) are calculated as

$$\rho_{\text{wet}} = M_{\text{wet}}/V_{\text{wet}}$$

$$\rho_{\text{dry}} = M_{\text{solid}}/V_{\text{wet}}$$

$$\rho_{\text{solid}} = M_{\text{solid}}/V_{\text{solid}}$$

$$\phi = V_{\text{pw}}/V_{\text{wet}} \text{ and}$$

$$VR = V_{\text{pw}}/V_{\text{solid}}$$

MAD properties reported and plotted in the Physical properties sections of all site chapters were calculated with the MADMax shipboard program.

Section Half Measurement Gantry

Shear strength measurements on split cores were performed via the automated vane shear strength device on the Section Half Measurement Gantry. Measurements were usually taken at ~20 cm section depth; however, if this interval did not provide high-quality sediment (e.g., if there were abundant sands or cracks), alternative positions were chosen to generate viable data. Vane shear strength ($S_{u(v)}$) can be determined by the torque (T) required to cause failure and a vane constant (K_v):

$$S_{u(v)} = T/K_v$$

All vane shear strength measurements were obtained using a vane with a height of 12.7 mm and a blade length of 6.35 mm. Failure torque was determined by measuring the rotation of a torsional spring using a spring-specific relation between rotation angle and torque.

Digital color image

The SHIL imaged the flat face of the archive half of split cores using a line-scan camera. Prior to imaging, and when necessary, the core face was prepared by scraping across, rather than along, the core section using a stainless steel or glass scraper. Scraping parallel to bedding with a freshly cleaned tool prevented cross-stratigraphic contamination. Post splitting, the archive halves were imaged as soon as possible to capture the core surface prior to drying and/or oxidation. Images were scanned at an interval of 10 lines/mm, with camera height allowing for square pixels. The imaging light was provided by three pairs of advanced illumination high-current-focused LED line lights with fully adjustable angles to the lens axis. Compression of line-scanned images on VCDs or summary figures may result in visual artifacts, primarily lamination that is not present in the actual sections. RGB data were also generated using the SHIL and used as a primary tool for stratigraphic correlation.

Spectrophotometry and visual color determination

After imaging, spectrophotometry and MS were measured on the archive halves with the SHMSL. Spurious measurements may occur from small cracks, drilling disturbance, or plastic section dividers. These data were further degraded by the inability of the instrument to consistently land the sensors flatly on the core surface, resulting in the leakage of ambient room light into the spectro-

photometer readings and reduced MS values. Additional details regarding measurement and interpretation of spectral data can be found in Balsam et al. (1997, 1998), Balsam and Damuth (2000), and Giosan et al. (2002).

Reflectance of visible light from the archive halves of sediment cores was measured using an Ocean Optics USB4000 spectrophotometer mounted on the automated SHMSL. Freshly split cores were covered with clear plastic wrap (Glad Wrap) and placed on the SHMSL. Measurements were taken at 2.5 cm spacing to provide a high-resolution stratigraphic record of color variation for visible wavelengths. Each measurement was recorded in 2 nm wide spectral bands from 400 to 900 nm.

MS was measured with a Bartington Instruments MS2E point sensor (high-resolution surface scanning sensor) on discrete points along the SHMSL track. Measurements were taken at the same spacing as the reflectance measurements, integrating a volume of 10.5 mm \times 3.8 mm \times 4 mm, where 10.5 mm is the length perpendicular to the core axis, 3.8 mm is the width in the core axis, and 4 mm is the depth. For conversion of the instrument units stored in the IODP database, a correction factor (67/80) must be employed to correct for the relation of the sensor diameter and sediment thickness.

Data preconditioning

The data acquired using the shipboard tools need to be conditioned to remove outliers that are related to end caps, voids, and foam spacers. A simple script written in MATLAB removed these data points for plotting and visualization purposes.

Downhole logging

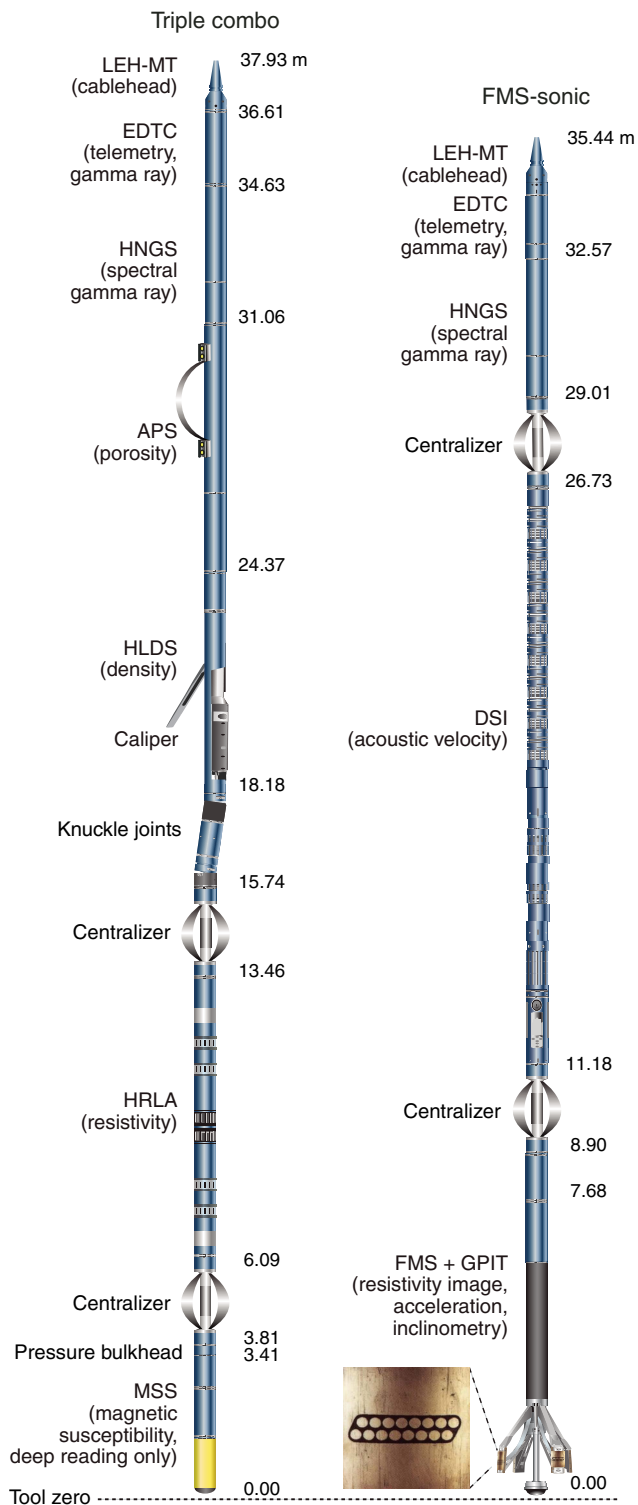
Downhole logs document the physical, chemical, and structural properties of the geological formations surrounding boreholes following drilling operations. The data are rapidly collected, continuous with depth (at vertical sampling intervals ranging from 2.5 to 150 mm), and measured in situ. Vertical resolutions are intermediate between laboratory measurements on core samples and surface geophysical surveys. Downhole logs are thus useful in calibrating the interpretation of geophysical survey data and provide a necessary link for the integrated understanding of physical properties at a range of spatial scales.

Downhole logs can be interpreted in terms of the stratigraphy, lithology, mineralogy, and geochemical composition of the penetrated formations. They also provide information on the condition, shape, and size of the borehole and on any possible deformation induced by drilling and/or formation stress. Where core recovery is incomplete or cored material is disturbed, log data may help to characterize missing intervals. Where core recovery is good, log and core data complement one another and may be interpreted jointly.

Logging operation

During wireline logging operations, a variety of logging tools are combined into several tool strings that are run down the hole after the completion of drilling operations. Two primary tool strings were utilized during Expedition 353 (Figure F6): the triple combo string (spectral and natural gamma ray, porosity, density, resistivity, and MS) and the Formation MicroScanner (FMS)-sonic string (spectral and natural gamma ray, elastic velocity, and resistivity images). These tool strings may be modified in response to expected borehole conditions or tool performance.

Figure F6. Wireline tool strings deployed during Expedition 353: triple combo and FMS-sonic. LEH-MT = logging equipment head-mud temperature, EDTC = Enhanced Digital Telemetry Cartridge, HNGS = Hostile Environment Natural Gamma Ray Sonde, APS = Accelerator Porosity Sonde, HLDS = Hostile Environment Litho-Density Sonde, HRLA = High-Resolution Laterolog Array, MSS = magnetic susceptibility sonde, DSI = Dipole Shear Sonic Imager, GPIT = General Purpose Inclinometry Tool.



In preparation for logging, boreholes are flushed of debris by circulating viscous drilling fluid and then filled with seawater or a seawater-based logging gel (sepiolite mud mixed with seawater; approximate density = 8.8 lb/gal, or 1.055 g/cm³) to help stabilize the borehole walls. Heavier logging fluid (sepiolite mud mixed with seawater, weighted with barite) may be used where borehole conditions call for additional stabilization. The BHA is pulled up to between 80 and 100 m DSE, depending on the stability of the hole. Each tool string is then lowered downhole by a seven-conductor wireline cable during sequential deployments. Each tool string deployment is a logging “run,” starting with the assembly of the tool string and the necessary calibrations. A tool string is then sent down to the bottom of the hole while recording a partial set of data and then is pulled up at a constant speed, typically 250–500 m/h, to record the primary data. During each run, tool strings can be lowered down and pulled up the hole several times to evaluate reproducibility or to try to improve the quality of the data. Each lowering or hauling-up of the tool string while collecting data constitutes a “pass.” During each pass, incoming data are recorded and monitored in real time using the minimum configuration multitask acquisition and imaging system (MAXIS). A logging run is complete once the tool string has been returned to the rig floor and disassembled. A wireline heave compensator (WHC) is employed to minimize the effect of ship’s heave on the tool string’s position in the borehole.

Logged properties and tool measurement principles

The main logging measurements recorded during Expedition 353 are listed in Table T8. More detailed descriptions of individual tools and their geological applications may be found in Ellis and Singer (2007), Goldberg (1997), Rider (1996), Lovell et al. (1998), Schlumberger (1989, 1994), and Serra (1984, 1986, 1989). A complete list of acronyms for the Schlumberger tools and measurement curves is available at <http://www.apps.slb.com/cmd>.

Caliper

The caliper log allows us to investigate the size of the borehole. Large-diameter boreholes that do not allow proper contact of the logging equipment with the borehole wall are detrimental to the log data quality. In particular, the FMS, sonic, density, and shallow-reading MS tools require good contact with the borehole wall; the quality of these logs may be degraded in zones where the borehole diameter varies over short intervals because of changes in lithology. Deep investigation measurements such as gamma ray and deep resistivity do not particularly require contact with the borehole wall and are therefore generally less sensitive to borehole conditions, although they may be affected by the mud chemistry.

Natural gamma radioactivity

The Hostile Environment Natural Gamma Ray Sonde (HNGS) was used to measure natural gamma radioactivity in the formation. It uses two bismuth germanate scintillation detectors and five-window spectroscopy to determine concentrations of potassium (in weight percent), thorium (in parts per million), and uranium (in parts per million). The radioactive isotopes of these three elements dominate NGR emissions in most rocks and sediments. The HNGS filters out gamma ray energies below 500 keV, eliminating sensitivity to bentonite or KCl in the drilling mud and improving measurement accuracy. The HNGS also provides a measure of the total spectral

Table T8. Downhole measurements made by wireline tool strings, Expedition 353. All tool names except Magnetic Susceptibility Sonde (MSS) are trademarks of Schlumberger. Sampling interval based on optimal logging speed. Acoustic imaging approximate vertical resolution is at 500 kHz. EDTC = Enhanced Digital Telemetry Cartridge, HNGS = Hostile Environment Natural Gamma Ray Sonde, HLDS = Hostile Environment Litho-Density Sonde, APS = Accelerator Porosity Sonde, HRLA = High-Resolution Laterolog Array, FMS = Formation MicroScanner, DSI = Dipole Shear Sonic Imager. [Download table in .csv format.](#)

Tool string	Tool	Measurement	Sampling interval (cm)	Vertical resolution (cm)
Triple combo with MSS	EDTC	Total gamma ray	5 and 15	30
	HNGS	Spectral gamma ray	15	20–30
	HLDS	Bulk density, borehole diameter	2.5 and 15	38
	APS	Neutron porosity	5 and 15	36
	HRLA	Resistivity	15	30
	MSS	Magnetic susceptibility (deep reading sensor only)	4	40
FMS-sonic	EDTC	Total gamma ray	5 and 15	30
	DSI	Acoustic velocity	15	107
	HNGS	Spectral gamma ray	15	20–30
	FMS	Microresistivity, borehole diameter	0.25	0.50

gamma ray (HSGR) emission and uranium-free or computed gamma ray (HCGR) emission that are measured in American Petroleum Institute units (gAPI). The HNGS response is influenced by the borehole diameter; therefore, HNGS data are corrected for borehole diameter variations during acquisition.

The Enhanced Digital Telemetry Cartridge (EDTC) was used primarily to communicate data from the tool strings in the borehole to the surface. The EDTC also includes a sodium iodide scintillation detector that measures the total natural gamma ray emissions. It is not a spectral tool, but it provides high-resolution total gamma radiation measurements for each pass, which allows precise depth match processing between logging runs and passes. The inclusion of a gamma ray tool (either HNGS or EDTC) in every tool string allows for the use of gamma ray data for depth correlation between logging strings and passes.

Density

Formation density was measured with the Hostile Environment Litho-Density Sonde (HLDS). The HLDS normally consists of a radioactive cesium (^{137}Cs) gamma ray source (661 keV) and far- and near-gamma ray detectors mounted on a shielded skid, which is pressed against the borehole wall by a hydraulically activated eccentricizing arm. Gamma rays emitted by the source undergo Compton scattering by electrons in the formation. The number of scattered gamma rays that reach the detectors is proportional to the density of electrons in the formation, which is in turn related to bulk density. Porosity may also be derived from this bulk density if the matrix density is known.

The HLDS also measures the photoelectric effect (PEF) caused by absorption of low-energy gamma rays. Photoelectric absorption occurs when gamma rays reach <150 keV after being repeatedly scattered by electrons in the formation. The PEF is determined by comparing counts from the far detector in the high-energy region, where only Compton scattering occurs, with those in the low energy region, where count rates depend on both reactions. The far detector is used because it has a greater depth of investigation (tens of centimeters). The response of the short-spaced detector, mostly influenced by mudcake (minimally present in riserless drilling because seawater-based mud is used) and borehole rugosity, is used to correct the density measurement for these effects. Because PEF depends on the atomic number of the elements in the formation, it also varies according to the chemical composition of the minerals present and can be used for the identification of some minerals. For

example, the PEF of calcite = 5.08 b/e⁻, illite = 3.03 b/e⁻, quartz = 1.81 b/e⁻, and kaolinite = 1.49 b/e⁻.

Good contact between the tool and borehole wall is essential for high-quality HLDS logs. Poor contact results in the underestimation of density values. Both the density correction and caliper measurements of borehole diameter are used to check the contact quality.

Porosity

Formation porosity was measured with the Accelerator Porosity Sonde. This sonde includes a minitron neutron generator that produces fast (14.4 MeV) neutrons and five neutron detectors (four epithermal and one thermal) positioned at different spacing from the minitron. The tool's detectors count neutrons that arrive at the detectors after being scattered and slowed by collisions with atomic nuclei in the formation.

The highest energy loss occurs when neutrons collide with hydrogen nuclei, which have practically the same mass as the neutron (the neutrons simply bounce off of heavier elements without losing much energy). If the hydrogen (i.e., water) concentration is low, as in low-porosity formations, neutrons can travel farther before being captured and the count rates increase at the detector. The opposite effect occurs in high-porosity formations where the water content is high. The raw porosity value is often an overestimate because hydrogen atoms bound in minerals such as clays or contained in hydrocarbons also contribute to the measurement.

Upon reaching thermal energies (0.025 eV), the neutrons are captured by the nuclei of Cl, Si, B, and other elements, resulting in a gamma ray emission. This neutron capture cross section (Σf) is also measured by the tool.

P-wave velocity

The Dipole Shear Sonic Imager (DSI) measures the transit times between sonic transmitters and an array of eight receivers. The recorded waveforms are then used to calculate the sonic velocity of the formation. The omnidirectional monopole transmitter emits high-frequency (5–15 kHz) pulses to extract the compressional wave velocity of the formation, as well as the shear wave velocity when it is faster than the S-wave velocity of the borehole fluid. It combines replicate measurements, thus providing a measurement of compressional wave velocity through sediment that is relatively free from the effects of formation damage and an enlarged borehole (Schlumberger, 1989). The same transmitter can be fired in se-

quence at a lower frequency (0.5–1 kHz) to generate Stoneley waves that are sensitive to fractures and variations in permeability. Along with the monopole transmitters found on most sonic tools, the DSI also has two cross-dipole transmitters, which allow an additional measurement of shear wave velocity. Dipole measurements are necessary to measure shear velocities in “slow” formations, where shear wave velocity is slower than the *S*-wave velocity in the borehole fluid. Such slow formations are typically encountered in deep-ocean drilling. The two shear wave velocities measured from the two orthogonal dipole transmitters can be used to identify sonic anisotropy associated with the local stress regime.

Formation MicroScanner

The FMS produces high-resolution images of borehole wall microresistivity that can be used for detailed lithostratigraphic and structural interpretation. The tool has four orthogonally oriented pads, each with 16 button electrodes that are pressed against the borehole walls. The electrodes are arranged in two diagonally offset rows of eight electrodes each. A focused current is emitted from the button electrodes into the formation, with a return electrode near the top of the tool. Resistivity of the formation at the button electrodes is derived from the intensity of current passing through the button electrodes. Processing transforms these measurements into oriented high-resolution images that reveal the geologic structures of the borehole wall based on their conductivity. Features such as bedding, stratification, fracturing, slump folding, and bioturbation can be resolved. The images are oriented to magnetic north so that fabric analysis can be carried out and the dip and direction (azimuth) of planar features in the formation can be measured. In addition, when the corresponding planar features can be identified in recovered core samples, individual core pieces can be reoriented with respect to true north.

The maximum extension of the FMS caliper arms is 15 inches (~38 cm). In boreholes with a diameter larger than this maximum, the pad contact at the end of the caliper will be inconsistent, and the FMS images may appear out of focus and may overestimate conductivity. Irregular borehole walls will also adversely affect the images if contact with the wall is poor. Approximately 30% of a borehole with a diameter of 25 cm is imaged during a single pass. Coverage can be increased by a second run. The vertical resolution of FMS images is ~5 mm.

Magnetic susceptibility

The magnetic susceptibility sonde (MSS), a wireline tool designed by Lamont-Doherty Earth Observatory (LDEO), measures the ease with which particular formations are magnetized when subjected to a magnetic field. The ease of magnetization, or MS, is ultimately related to the concentration and composition (size, shape, and mineralogy) of material within the formation. These measurements provide one of the best methods for investigating stratigraphic changes in mineralogy and lithology because the measurement is quick, repeatable, and nondestructive and because different lithologies often have strongly contrasting susceptibilities. High-resolution susceptibility measurements can aid significantly in paleoclimatic and paleoceanographic studies, where construction of an accurate and complete stratigraphic framework is critical to reconstructing past climatic changes.

A single-coil sensor provides high-resolution measurements (~10 cm vertical resolution) with a shallow depth of investigation (~3 cm penetration into the borehole wall). A dual-coil sensor pro-

vides lower resolution measurements (~40 cm vertical resolution), with greater depth of investigation (~20 cm penetration into the borehole wall), and because of its more robust nature acts as a quality control for the high-resolution measurements. The MSS can be run as a component in a Schlumberger tool string, using a specially developed data translation cartridge. For quality control and environmental correction, the MSS also measures internal tool temperature and z-axis acceleration.

Electrical resistivity

The High-Resolution Laterolog Array (HRLA) provides six electrical resistivity measurements with different depths of investigation (including the borehole, or mud resistivity, and five measurements of formation resistivity with increasing penetration into the formation). This sonde sends a focused current into the formation and measures the intensity necessary to maintain a constant drop in voltage across a fixed interval, providing a direct resistivity measurement. The array has one central (source) electrode and six electrodes above and below it, which serve alternatively as focusing and returning current electrodes. By rapidly changing the role of these electrodes, a simultaneous resistivity measurement at six penetration depths is achieved. The tool is designed to ensure that all signals are measured at exactly the same time and tool position and to reduce the sensitivity to “shoulder bed” effects when crossing sharp beds thinner than the electrode spacing. The design of the HRLA, which eliminates the need for a surface reference electrode, improves formation resistivity evaluation compared to the traditional dual induction method. The HRLA is run centralized in the borehole for optimal results, so knuckle joints are used to centralize the HRLA while allowing the eccentricized density and porosity tools to maintain good contact with the borehole wall.

The Phasor Dual Induction–Spherically Focused Resistivity Tool (DIT) was used rather than the HRLA to measure electrical resistivity in boreholes where unstable hole conditions presented greater risk to logging tools. The DIT provides three measures of resistivity at different depths of investigation into the formation. The two induction devices (deep and medium depths of penetration) transmit high-frequency alternating current through coil transmitters, creating a magnetic field that induces a secondary current in the formation. These currents produce a new inductive signal, proportional to the conductivity of the formation, which is measured by the receiving coils. Measured conductivities are then converted to resistivity (in ohm-meters). Spherically focused resistivity is measured by an electrode device that sends a current into the formation while maintaining a constant voltage drop. The amount of current necessary to keep a constant voltage gives a direct measure of resistivity. This device uses electrodes to focus the current flow into the formation so that equipotential surfaces are spherical and has a shallower depth of investigation and a higher vertical resolution than induction measurements.

Auxiliary logging equipment

Cable head

The Schlumberger logging equipment head (or cable head) measures tension at the very top of the wireline tool string, which diagnoses difficulties in running the tool string up or down the borehole or when exiting or entering the drill string or casing. The logging equipment head-mud temperature (LEH-MT) used during Expedition 353 also includes a thermal probe to measure the borehole fluid temperature.

Telemetry cartridges

Telemetry cartridges are used in each tool string to allow the transmission of the data from the tools to the surface. The EDTC also includes a sodium iodide scintillation detector to measure the total natural gamma ray emission of the formation. This gamma ray log is used to match depths between different passes and runs. In addition, it includes an accelerometer that can be used in real time to evaluate the efficiency of the WHC.

Joints and adapters

Because the tool strings combine tools of different generations and with various designs, they include several adapters and joints between individual tools to allow communication, provide isolation, avoid interferences (mechanical and acoustic), terminate wiring, or to position the tool properly in the borehole. Knuckle joints in particular are used to allow some of the tools such as the HRLA to remain centralized in the borehole while the overlying HLDS is pressed against the borehole wall.

Wireline heave compensator

The WHC system is designed to compensate for the vertical motion of the ship and maintain a steady motion of the logging tools. It uses vertical acceleration measurements made by a motion reference unit (MRU), located under the rig floor near the center of gravity of the ship, to calculate the vertical motion of the ship. It then adjusts the length of the wireline by varying the distance between two sets of pulleys through which the cable passes. Real-time measurements of uphole (surface) and downhole acceleration are made simultaneously by the MRU and EDTC, respectively. An LDEO-developed software package allows these data to be analyzed and compared in real time, displaying the actual motion of the logging tool string and enabling monitoring of the efficiency of the compensator.

Logging data flow and depth scales

Data for each wireline logging run were monitored in real time and recorded using the Schlumberger MAXIS 500 system. These data were then copied to the shipboard processing stations for preliminary processing. Typically, the main pass of the triple combo is used as a reference to which other passes are interactively depth matched. The initial logging data are referenced to the rig floor (WRF). After depth matching, all the logging depths were shifted to a seafloor reference (WSF) based on the step in the gamma radiation at the sediment/water interface and preliminarily depth matched to remove offsets between different logging passes. Potential sources of error in depth matching include sea state, uncompensated heave, wireline stretch, and errors in the reference

log used; the magnitude of uncertainty is typically on the order of centimeters to meters (IODP Depth Scales Terminology, v.2, at <http://www.iodp.org/policies-and-guidelines>). These data were made available to the science party within a few days of their acquisition.

The downhole log data were also transferred onshore to LDEO for standardized data processing. The main part of the processing is rigorous depth matching to remove depth offsets between different logging passes, which results in a new depth scale: wireline log matched depth below seafloor (WMSF). Also, corrections are made to certain tools and logs (e.g., FMS images are corrected for tool acceleration), documentation for the logs (with an assessment of log quality) is prepared, and data are converted to ASCII for the conventional logs. The standardized processed data are made available (in ASCII and DLIS formats) shortly after the expedition through the IODP logging database (<http://iodp.ldeo.columbia.edu/DATA/index.html>).

For a summary of borehole and downhole logging depth scales used during Expedition 353, see Table T9.

Log data quality

The principal influence on log data quality is the condition of the borehole wall. If the borehole diameter varies over short intervals because of washouts during drilling or ledges made of layers of harder material, the logs from tools that require good contact with the borehole wall (i.e., the FMS and density tools) may be degraded. Very narrow (“bridged”) sections will also cause irregular log results. The quality of the borehole is improved by minimizing the circulation of drilling fluid while drilling, conditioning by flushing the borehole to remove debris, and logging as soon as possible after drilling and conditioning are completed.

The quality of the logging depth determination depends on several factors. The depth of the logging measurements is determined from the length of the cable payed out from the winch on the ship. The seafloor (mudline) is identified on the natural gamma log by the abrupt reduction in gamma ray count at the water/sediment boundary. Discrepancies between DSF, CSF-A, and WMSF depths occur because of core expansion, incomplete core recovery, tides, or incomplete heave compensation for the drilling depth. In the case of log depth, discrepancies between successive runs occur because of incomplete heave compensation, incomplete correction for cable stretch, and cable slip. In the case of very fine sediments in suspension, the mudline can be an elusive datum. Tidal changes in sea level also will have an effect. The hydraulic WHC was used to adjust the wireline length for rig motion during wireline logging operations, to minimize the wireline tool motion caused by ship heave.

Table T9. Borehole and downhole logging depth scales, Expedition 353. [Download table in .csv format.](#)

Depth scale	Complete name	Definition
DSF	Drillers depth below seafloor	The length of all drill string components between seafloor and target.
WRF	Wireline log depth below rig floor	Length of wireline and sensor offset between the rig floor and the target.
WSF	Wireline log depth below seafloor	WRF with seafloor depth below rig floor subtracted.
WMSF	Wireline log matched depth below seafloor	Depth derived by correlation between reference run and all additional runs to make a set of WSF runs internally consistent.

Stratigraphic correlation

The function of stratigraphic correlation is (1) to provide guidance to drillers attempting to cover drilling gaps in successive holes at each site and (2) to construct complete stratigraphic sections at each site using information from multiple holes such that shipboard or shore-based measurements/data are discussed in a common depth scale reference system.

Complete stratigraphic sections cannot be constructed from a single drilled hole because core-recovery gaps on the order of 20 to 50 cm occur between successive cores despite 100% or more nominal recovery (e.g., Ruddiman et al., 1987; Hagelberg et al., 1995; Acton et al., 2001). The construction of a complete stratigraphic section, referred to as a splice, requires combining stratigraphic intervals from two or more offset holes cored at a single site.

Core depth below seafloor (CSF-A) scale

By definition, the depth to the top of each core is based on the DSF scale. DSF is essentially the length of the drill string below the rig floor to the top of the cored interval minus the length of drill string from the rig floor to the mudline, which is assumed to be the seafloor. Adding the DSF of the top of each core to the curated length measured to any given sample or data point in that core will provide a depth for that sample/data point. This resulting depth scale is referred to as CSF-A (Figure F7) and includes expansion due to relief of overburden as well as gas expansion as the cores are raised from the seafloor to atmospheric pressure and temperature. The CSF-A scale is equivalent to the historical DSDP, ODP, and Integrated Ocean Drilling Program meters below seafloor (mbsf) scale (see IODP Depth Scales Terminology, v.2, at <http://www.iodp.org/policies-and-guidelines>). Error in the CSF-A scale includes pipe and BHA stretch and compression, tides, and uncompensated heave, as well as incomplete recovery and core expansion as a result of elastic rebound and gas. During this expedition, tides were minimal and not accounted for.

Core composite depth below seafloor (CCSF-A) scale

Constructing a composite depth scale entails integrating collocated, and assumed coeval, laterally continuous stratigraphic features into a common frame of reference by shifting the depth of each individual core (starting on the CSF-A scale) to maximize correlation between holes. The resulting CCSF-A scale is equivalent to the historical ODP and Integrated Ocean Drilling Program meters composite depth (mcd) scale. In constructing the CCSF-A scale from the CSF-A scale, the depths of the individual cores are shifted by a core-specific constant amount (i.e., no stretching or squeezing within an individual core is employed). The CCSF-A scale provides good first-order correlation between cores from different holes, estimates of the length of coring gaps, and a basis upon which higher order composite depth scales are constructed. The mudline is not merely taken as the top of the first core in a given hole but is the top of the core with the best-preserved sediment/water interface. This core anchors the entire composite depth scale for all holes at a site. The anchor core is typically the only core in which the depths are the same for both the CSF-A and CCSF-A scales. Each core downhole is then tied to the composite section by adding or subtracting a single depth offset that best aligns an observed lithologic feature among adjacent cores from different holes. Due to the differing effects of coring-induced stretching and squeezing among cores as

well as hole-to-hole sedimentological differences, this approach very rarely aligns all features (Figure F7).

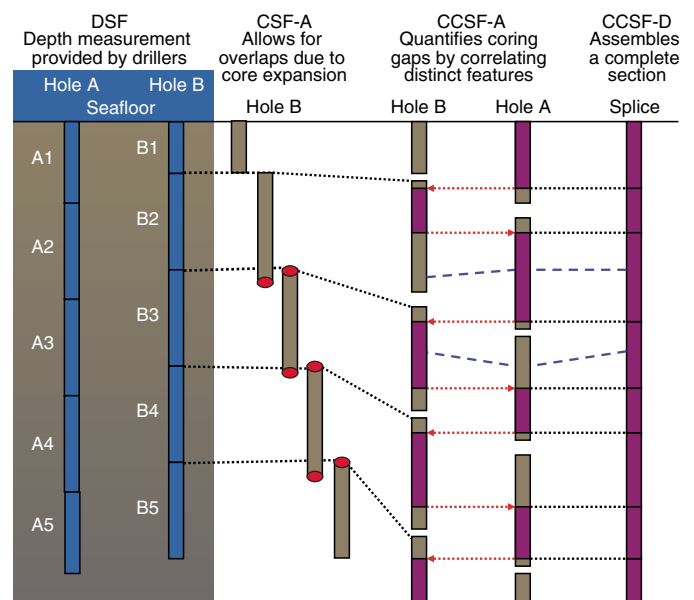
The depth offset of every core is tabulated in an affine table. If gaps between cores never come into alignment among all holes at a site and recovery is sufficiently high, it should be possible to correlate (or “tie”) each successive core in one hole to a core from an adjacent hole, all the way to the bottom of a drilled section. If aligned coring gaps across all holes at a site do occur, the cores below the gap are no longer tied to the mudline core but can often still be tied to one another.

When constructing the composite section, the total CCSF-A depth is typically ~5% to 15% longer than the CSF-A scale. This expansion is mostly caused by decompression of the cores as they are brought to the surface, gas expansion, stretching that occurs as part of the coring process, and/or from curation practice, in which material that has fallen downhole or gas expansion voids are curated as part of the core (e.g., Hagelberg et al., 1995; Acton et al., 2001).

Core composite depth below seafloor (CCSF-D) scale

Once the CCSF-A scale has been developed and the between-core gaps identified, a complete stratigraphic section is created by splicing together selected intervals from the various holes such that gaps, overlaps, and disturbed sections are avoided. The depth scale for this “splice” is designated the CCSF-D scale (Figure F7). Al-

Figure F7. Depth scales used during Expedition 353. Blue, brown, and purple = recovered core. Dashed and dotted lines = equivalent horizons. Core depth below seafloor and core composite depth below seafloor scales: “-A” and “-D” differentiate different methods of depth scale construction. The CSF-A scale is established by adding the curated core length to the core top DSF depth. Core expansion creates apparent overlaps and stratigraphic reversals when data are plotted on the CSF-A scale (red ovals). The CCSF-A scale is constructed based on correlation of distinct horizons identified in multiple holes at a given site (red dashed arrows). The primary splice (CCSF-D) is constructed by combining selected intervals (purple) such that coring gaps and disturbed section are excluded, resulting in a complete stratigraphic section (less any natural, sedimentological hiatuses). CCSF-A depth designations are not necessarily equivalent to CCSF-D for intervals not included in the splice (blue dashed lines).



though CCSF-D is merely a subset of the CCSF-A, the -D designation applies only to intervals included in the splice. Intervals not included in the primary splice, including any alternate splice(s), are assigned a CCSF-A scale only. If coring gaps aligned across all holes drilled at a site do occur, the spliced sections below are “appended” to those above and referred to as “floating splice sections” (i.e., not tied to the mudline). The amount of missing material between floating splices can be measured using appropriate downhole logs. Where no logs are available, the CCSF-A scale provides a reasonably accurate estimate of the length of the missing section, especially when coring in calm seas.

Core composite depth below seafloor (CCSF-C) scale

At some sites, once the splice is constructed, it is possible to map into the splice those intervals not used in constructing the splice itself. This methodology is based on identification of tie points among records, with linear adjustments of data between ties. This is designated as the CCSF-C scale and is best thought of as the “equivalent splice depth.” The CCSF-C and CCSF-D scales are only equivalent to the extent that the correlations are accurate. These depth-depth mapping functions, if available, are provided in table form for specific sites. At core boundaries, where strong stretching and compression are prevalent, the depth maps are less accurate. Users are encouraged to plot the data on the CCSF-C scale along with the splice (CCSF-D scale) in order to assess whether or not the CCSF-C scale is sufficiently accurate for the intended use. We did not construct CCSF-C tables based on shipboard data but intend to provide these tables at a later stage when high-resolution X-ray fluorescence scanner data are available that allow a more detailed stratigraphic correlation, particularly for the four holes of Site U1443.

Measurements and methods specific to Expedition 353

Compositing and splicing was accomplished using Correlator software (version 2.01, released during Expedition 353; <http://core-wall.org/downloads.html>) to generate standard affine tables (lists of offsets added to each core to place it on the CCSF-A scale) and splice interval tables. During the cruise we used specific applications (i.e., SCORS Downloader and Uploader) for downloading and uploading data to and from Correlator. These tables were uploaded into the LIMS database. Real-time correlation contributed to guiding drilling of offset holes during the expedition. However, generating splice interval tables and affine tables was not possible until one week before the end of the expedition because of problems with the new version of the correlating software (Correlator) and its interfacing with the LIMS database. Old versions of Correlator were tried and found incompatible with the LIMS database. As a result, the quality of splices and affines provided are limited by the time available during the last week of the expedition. Postcruise, the splice interval tables were modified using the Splice-File-Fixer program to ensure that each depth has been assigned the correct sample identification. Both the affine and the corrected splice interval tables were uploaded into LIMS during the first postcruise meeting in June 2015. The core top depths in the affine tables were not corrected and hence may be slightly incorrect in a range of <2 cm. However, the offsets are correct.

The composite sections and splices are based on the stratigraphic correlation of data sets acquired from the WRMSL, the NGRL, and digitized green color data (from the RGB triplet) ex-

tracted from core images acquired from the SHIL. Details on the instruments calibrations, settings, and measurement intervals for Expedition 353 are given in **Physical properties**. The resulting data sets available for compositing and splicing included MS, GRA, and RGB (green) data. The remaining components of the RGB triplet (red and blue) are highly correlated to green and to each other because, to a first order, all are measures of the reflectivity of the sediment. The small differences between R, G, and B can be expressed as ratios such as red/green, red/blue, or green/blue. However, ratios were not employed in our correlation due to lack of time. Reflectance spectroscopy data (i.e., L^* , a^* , and b^*), which can produce information similar to RGB ratios, were not used for correlation due to inconsistent variability from hole to hole resulting from low-quality wavelength spectra collected by the Ocean Optics USB4000 spectrophotometer on the monotonously dark sediments of Sites U1445–U1448. The only exception is Site U1443 where light, carbonate-rich pelagic sediments allowed collection of better reflectance data.

To allow for real-time correlation during Expedition 353, we followed a strategy developed during Expedition 346. We employed both the STMSL and WRMSL in measuring GRA and MS on thermally unequilibrated cores immediately after recovery and processing on the catwalk. This effectively doubles the measurement speeds for GRA and MS, allowing us to evaluate gap coverage in near real time.

In most cases, splices were constructed on the basis of whole-round MS and green (RGB) data acquired after the cores were split and imaged, aided at times by NGR data. At sites with significant gas expansion, where voids developed in the liner, the process of splitting (bottom to top) causes sediment to be moved upsection, which may introduce centimeter- to decimeter-scale differences between parameters measured on whole-round versus split cores (see each site chapter for details). For these reasons, the WRMSL and STMSL MS and GRA data may not agree with data generated after splitting (e.g., RGB).

References

- Acton, G.D., Borton, C.J., and the Leg 178 Shipboard Scientific Party, 2001. Palmer Deep composite depth scales for Leg 178 Sites 1098 and 1099. In Barker, P.F., Camerlenghi, A., Acton, G.D., and Ramsay, A.T.S. (Eds.), *Proceedings of the Ocean Drilling Program, Scientific Results*, 178: College Station, TX (Ocean Drilling Program), 1–35. <http://dx.doi.org/10.2973/odp.proc.sr.178.202.2001>
- Aguirre, E., and Pasini, G., 1985. The Pliocene–Pleistocene boundary. *Epi-sodes*, 8:11–120.
- ASTM International, 1990. Standard method for laboratory determination of water (moisture) content of soil and rock (Standard D2216–90). In *Annual Book of ASTM Standards for Soil and Rock* (Volume 04.08): Philadelphia (American Society for Testing Materials). [revision of D2216-63, D2216-80]
- Balsam, W.L., and Damuth, J.E., 2000. Further investigations of shipboard vs. shore-based spectral data: implications for interpreting Leg 164 sediment composition. In Paull, C.K., Matsumoto, R., Wallace, P., and Dillon, W.P. (Eds.), *Proceedings of the Ocean Drilling Program, Scientific Results*, 164: College Station, TX (Ocean Drilling Program), 313–324. <http://dx.doi.org/10.2973/odp.proc.sr.164.222.2000>
- Balsam, W.L., Damuth, J.E., and Schneider, R.R., 1997. Comparison of shipboard vs. shore-based spectral data from Amazon Fan cores: implications for interpreting sediment composition. In Flood, R.D., Piper, D.J.W., Klaus, A., and Peterson, L.C. (Eds.), *Proceedings of the Ocean Drilling Program, Scientific Results*, 155: College Station, TX (Ocean Drilling Program), 193–215. <http://dx.doi.org/10.2973/odp.proc.sr.155.210.1997>

- Balsam, W.L., Deaton, B.C., and Damuth, J.E., 1998. The effects of water content on diffuse reflectance spectrophotometry studies of deep-sea sediment cores. *Marine Geology*, 149(1–4):177–189. [http://dx.doi.org/10.1016/S0025-3227\(98\)00033-4](http://dx.doi.org/10.1016/S0025-3227(98)00033-4)
- Barron, J.A., 1980. Upper Pliocene and Quaternary diatom biostratigraphy of Deep Sea Drilling Project Leg 54, tropical eastern Pacific. In Rosendahl, B.R., Hekinian, R., et al., *Initial Reports of the Deep Sea Drilling Project*, 54: Washington, DC (U.S. Government Printing Office), 455–485. <http://dx.doi.org/10.2973/dsdp.proc.54.117.1980>
- Barron, J.A., 1983. Latest Oligocene through early middle Miocene diatom biostratigraphy of the eastern tropical Pacific. *Marine Micropaleontology*, 7(6):487–515. [http://dx.doi.org/10.1016/0377-8398\(83\)90012-9](http://dx.doi.org/10.1016/0377-8398(83)90012-9)
- Barron, J.A., 1985a. Late Eocene to Holocene diatom biostratigraphy of the equatorial Pacific Ocean, Deep Sea Drilling Project Leg 85. In Mayer, L., Theyer, F., Thomas, E., et al., *Initial Reports of the Deep Sea Drilling Project*, 85: Washington, DC (U.S. Government Printing Office), 413–456. <http://dx.doi.org/10.2973/dsdp.proc.85.108.1985>
- Barron, J.A., 1985b. Miocene to Holocene planktic diatoms. In Bolli, H.M., Saunders, J.B., and Perch-Nielsen, K. (Eds.), *Plankton Stratigraphy*: Cambridge, United Kingdom (Cambridge University Press), 763–809.
- Barron, J.A., Fourtanier, E., and Bohaty, S.M., 2004. Oligocene and earliest Miocene diatom biostratigraphy of ODP Leg 199 Site 1220, equatorial Pacific. In Wilson, P.A., Lyle, M., Janecek, T.R., and Firth, J.V. (Eds.), *Proceedings of the Ocean Drilling Program, Scientific Results*, 199: College Station, TX (Ocean Drilling Program), 1–25. <http://dx.doi.org/10.2973/odp.proc.sr.199.204.2004>
- Barron, J.A., and Gladenkov, A.Y., 1995. Early Miocene to Pleistocene diatom stratigraphy of Leg 145. In Rea, D.K., Basov, I.A., Scholl, D.W., and Allan, J.F. (Eds.), *Proceedings of the Ocean Drilling Program, Scientific Results*, 145: College Station, TX (Ocean Drilling Program), 3–19. <http://dx.doi.org/10.2973/odp.proc.sr.145.101.1995>
- Berggren, W.A., Kent, D.V., Swisher, C.C., III, and Aubry, M.-P., 1995. A revised Cenozoic geochronology and chronostratigraphy. In Berggren, W.A., Kent, D.V., Aubry, M.-P., and Hardenbol, J. (Eds.), *Geochronology, Time Scales and Global Stratigraphic Correlation*. Special Publication - SEPM (Society for Sedimentary Geology), 54:129–212. <http://dx.doi.org/10.2110/pec.95.04.0129>
- Berggren, W.A., and Pearson, P.N., 2005. A revised tropical to subtropical Paleogene planktonic foraminiferal zonation. *Journal of Foraminiferal Research*, 35(4):279–298. <http://dx.doi.org/10.2113/35.4.279>
- Blow, W.H., 1979. *The Cainozoic Globigerinida: A Study of the Morphology, Taxonomy, Evolutionary Relationships and the Stratigraphical Distribution of Some Globigerinida (mainly Globigerinacea)*: Leiden, The Netherlands (E.J. Brill).
- Blum, P., 1997. *Technical Note 26: Physical Properties Handbook—A guide to the Shipboard Measurement of Physical Properties of Seep-sea Cores*. Ocean Drilling Program. <http://dx.doi.org/10.2973/odp.tn.26.1997>
- Bolli, H.M., and Saunders, J.B., 1985. Oligocene to Holocene low latitude planktic foraminifera. In Bolli, H.M., Saunders, J.B., and Perch-Nielsen, K. (Eds.), *Plankton Stratigraphy* (Volume 1): *Planktic Foraminifera, Calcareous Nannofossils and Calpionellids*: Cambridge, United Kingdom (Cambridge University Press), 155–262.
- Bouma, A.H., 1962. *Sedimentology of Some Flysch Deposits: A Graphic Approach to Facies Interpretation*: Amsterdam (Elsevier).
- Bown, P.R. (Ed.), 1998. *Calcareous Nannofossil Biostratigraphy*: London (Chapman and Hall).
- Bown, P.R., 2005. Palaeogene calcareous microfossils from the Kilwa and Lindi areas of coastal Tanzania (Tanzania Drilling Project 2003–4). *Journal of Nannoplankton Research*, 27(1):21–95.
- Bralower, T.J., Leckie, R.M., Sliter, W.V., and Thierstein, H.R., 1995. An integrated Cretaceous microfossil biostratigraphy. In Berggren, W.A., Kent, D.V., Aubry, M.-P., and Hardenbol, J. (Eds.), *Geochronology, Time Scales, and Global Stratigraphic Correlation*. Special Publication - SEPM (Society for Sedimentary Geology), 54:65–79. <http://dx.doi.org/10.2110/pec.95.04.0065>
- Burnett, J.A., 1998. Upper Cretaceous. In Bown, P.R. (Ed.), *Calcareous Nannofossil Biostratigraphy*: Dordrecht, The Netherlands (Kluwer Academic Publishing), 132–199.
- Cande, S.C., and Kent, D.V., 1995. Revised calibration of the geomagnetic polarity timescale for the Late Cretaceous and Cenozoic. *Journal of Geophysical Research: Solid Earth*, 100(B4):6093–6095. <http://dx.doi.org/10.1029/94JB03098>
- Chaisson, W.P., and Pearson, P.N., 1997. Planktonic foraminifer biostratigraphy at Site 925: middle Miocene–Pleistocene. In Shackleton, N.J., Curry, W.B., Richter, C., and Bralower, T.J. (Eds.), *Proceedings of the Ocean Drilling Program, Scientific Results*, 154: College Station, TX (Ocean Drilling Program), 3–31. <http://dx.doi.org/10.2973/odp.proc.sr.154.104.1997>
- Dunlea, A.G., Murray, R.W., Harris, R.N., Vasiliev, M.A., Evans, H., Spivack, A.J., and D'Hondt, S., 2013. Assessment and use of NGR instrumentation on the JOIDES Resolution to quantify U, Th, and K concentrations in marine sediment. *Scientific Drilling*, 15:57–63. <http://dx.doi.org/10.2204/iodp.sd.15.05.2013>
- Ellis, D.V., and Singer, J.M., 2007. *Well Logging for Earth Scientists* (2nd edition): New York (Elsevier).
- Evans, H.B., 1965. GRAPE—a device for continuous determination of material density and porosity. *Transactions of the SPWLA Annual Logging Symposium*: 6(2):B1–B25. <https://www.spwla.org/SymposiumTransactions/grape-device-continuous-determination-material-density-and-porosity>
- Fenner, J., 1984. Eocene–Oligocene planktic diatom stratigraphy in the low latitudes and the high southern latitudes. *Micropaleontology*, 30(4):319–342. <http://dx.doi.org/10.2307/1485708>
- Fenner, J., 1985. Late Cretaceous to Oligocene planktic diatoms. In Bolli, H.M., Saunders, J.B., and Perch-Nielsen, K. (Eds.), *Plankton Stratigraphy*: Cambridge, United Kingdom (Cambridge University Press), 713–762.
- Fenner, J., and Mikkelsen, N., 1990. Eocene–Oligocene diatoms in the western Indian Ocean: taxonomy, stratigraphy, and paleoecology. In Duncan, R.A., Backman, J., et al., *Proceedings of the Ocean Drilling Program, Scientific Results*, 115: College Station, TX (Ocean Drilling Program), 433–463. <http://dx.doi.org/10.2973/odp.proc.sr.115.207.1990>
- Fourtanier, E., 1991a. Diatom biostratigraphy of equatorial Indian Ocean Site 758. In Weissel, J., Peirce, J., Taylor, E., Alt, J., et al., *Proceedings of the Ocean Drilling Program, Scientific Results*, 121: College Station, TX (Ocean Drilling Program), 189–208. <http://dx.doi.org/10.2973/odp.proc.sr.121.137.1991>
- Fourtanier, E., 1991b. Paleocene and Eocene diatom biostratigraphy and taxonomy of eastern Indian Ocean Site 752. In Weissel, J., Peirce, J., Taylor, E., Alt, J., et al., *Proceedings of the Ocean Drilling Program, Scientific Results*, 121: College Station, TX (Ocean Drilling Program), 171–187. <http://dx.doi.org/10.2973/odp.proc.sr.121.136.1991>
- Gieskes, J.M., Gamo, T., and Brumsack, H., 1991. *Technical Note 15: Chemical Methods for Interstitial Water Analysis Aboard JOIDES Resolution*. Ocean Drilling Program. <http://dx.doi.org/10.2973/odp.tn.15.1991>
- Giosan, L., Flood, R.D., and Aller, R.C., 2002. Paleooceanographic significance of sediment color on western North Atlantic drifts: I. Origin of color. *Marine Geology*, 189(1–2):25–41. [http://dx.doi.org/10.1016/S0025-3227\(02\)00321-3](http://dx.doi.org/10.1016/S0025-3227(02)00321-3)
- Goldberg, D., 1997. The role of downhole measurements in marine geology and geophysics. *Reviews of Geophysics*, 35(3):315–342. <http://dx.doi.org/10.1029/97RG00221>
- Gradstein, F.M., Ogg, J.G., and Smith, A. (Eds.), 2004. *A Geologic Time Scale 2004*: Cambridge, United Kingdom (Cambridge University Press). <http://dx.doi.org/10.2277/0521786738>
- Gradstein, F.M., Ogg, J.G., Schmitz, M.D., and Ogg, G.M. (Eds.), 2012. *The Geological Time Scale 2012*: Amsterdam (Elsevier).
- Hagelberg, T.K., Pisias, N.G., Shackleton, N.J., Mix, A.C., and Harris, S., 1995. Refinement of a high-resolution, continuous sedimentary section for studying equatorial Pacific Ocean paleoceanography, Leg 138. In Pisias, N.G., Mayer, L.A., Janecek, T.R., Palmer-Julson, A., and van Andel, T.H. (Eds.), *Proceedings of the Ocean Drilling Program, Scientific Results*, 138: College Station, TX (Ocean Drilling Program), 31–46. <http://dx.doi.org/10.2973/odp.proc.sr.138.103.1995>
- Hajós, M., 1975. Late Cretaceous archaeomonadaceae, diatomaceae, and silicoflagellatae from the south Pacific Ocean, Deep Sea Drilling Project, Leg 29, Site 275. In Kennett, J.P., Houtz, R.E., et al., *Initial Reports of the Deep*

- Sea Drilling Project*, 29: Washington, DC (U.S. Government Printing Office), 913–1009. <http://dx.doi.org/10.2973/dsdp.proc.29.126.1975>
- Harms, J.C., and Choquette, P.W., 1965. Geologic evaluation of a gamma-ray porosity device. *Transactions of the SPWLA Annual Logging Symposium*, 6(2):C1–C37.
- Harwood, D.M., 1988. Upper Cretaceous and lower Paleocene diatom and silicoflagellate biostratigraphy of Seymour Island, eastern Antarctic Peninsula. In Feldman, R.M., and Woodburne, M.O. (Eds.), *Geology and Paleontology of Seymour Island*. Memoir - Geological Society of America, 169:55–129.
- Hornibrook, N.d.B., Brazier, R.C., and Strong, C.P., 1989. Manual of New Zealand Permian to Pleistocene foraminiferal biostratigraphy. *New Zealand Geological Survey Paleontological Bulletin*, 56.
- Jenkins, D.G., 1971. New Zealand Cenozoic planktonic foraminifera. *New Zealand Geological Survey Paleontological Bulletin*, 42.
- Keene, J.B., 1975. Cherts and porcellanites from the North Pacific DSDP, Leg 32. In Larson, R.L., Moberly, R., et al. *Initial Reports of the Deep Sea Drilling Project*, 32: Washington, DC (U.S. Government Printing Office), 429–507. <http://dx.doi.org/10.2973/dsdp.proc.32.114.1975>
- Kennett, J.P., and Srinivasan, M.S., 1983. *Neogene Planktonic Foraminifera: A Phylogenetic Atlas*: Stroudsburg, PA (Hutchinson Ross).
- Kirschvink, J.L., 1980. The least-squares line and plane and the analysis of palaeomagnetic data. *Geophysical Journal of the Royal Astronomical Society*, 62(3):699–718. <http://dx.doi.org/10.1111/j.1365-246X.1980.tb02601.x>
- Koç, N., and Scherer, R.P., 1996. Neogene diatom biostratigraphy of the Iceland Sea Site 907. In Thiede, J., Myhre, A.M., Firth, J.V., Johnson, G.L., and Ruddiman, W.F. (Eds.), *Proceedings of the Ocean Drilling Program, Scientific Results*, 151: College Station, TX (Ocean Drilling Program), 61–74. <http://dx.doi.org/10.2973/odp.proc.sr.151.108.1996>
- Kvenvolden, K.A., and McDonald, T.J., 1986. *Technical Note, 6: Organic Geochemistry on the JOIDES Resolution—An Assay*. Ocean Drilling Program. <http://dx.doi.org/10.2973/odp.tn.6.1986>
- Lourens, L.J., Hilgen, F.J., Laskar, J., Shackleton, N.J., and Wilson, D., 2004. The Neogene period. In Gradstein, F.M., Ogg, J., et al. (Eds.), *A Geologic Time Scale 2004*: Cambridge, United Kingdom (Cambridge University Press), 409–440.
- Lovell, M.A., Harvey, P.K., Brewer, T.S., Williams, C., Jackson, P.D., and Williamson, G., 1998. Application of FMS images in the Ocean Drilling Program: an overview. In Cramp, A., MacLeod, C.J., Lee, S.V., and Jones, E.J.W. (Eds.), *Geological Evolution of Ocean Basins: Results from the Ocean Drilling Program*. Geological Society Special Publication, 131(1):287–303. <http://dx.doi.org/10.1144/GSL.SP.1998.131.01.18>
- Luciani, V., and Giusberti, L., 2014. Reassessment of the early–middle Eocene planktonic foraminiferal biomagnetostratigraphy: new evidence from the Tethyan Possagno section (NE Italy) and western North Atlantic Ocean ODP Site 1051. *Journal of Foraminiferal Research*, 44(2):187–201. <http://dx.doi.org/10.2113/gsjfr.44.2.187>
- Manheim, F.T., and Sayles, F.L., 1974. Composition and origin of interstitial waters of marine sediments, based on deep sea drill cores. In Goldberg, E.D. (Ed.), *The Sea (Volume 5): Marine Chemistry: The Sedimentary Cycle*: New York (Wiley), 527–568.
- Martini, E., 1971. Standard Tertiary and Quaternary calcareous nannoplankton zonation. In Farinacci, A. (Ed.), *Proceedings of the Second Plankton Conference, Roma 1970*: Rome (Edizioni Tecnoscienza), 2:739–785.
- Mazzullo, J.M., Meyer, A., and Kidd, R.B., 1988. New sediment classification scheme for the Ocean Drilling Program. In Mazzullo, J., and Graham, A.G. (Eds.), *Technical Note 8: Handbook for Shipboard Sedimentologists*. Ocean Drilling Program, 44–67. <http://dx.doi.org/10.2973/odp.tn.8.1988>
- Mikkelsen, N., 1990. Cenozoic diatom biostratigraphy and paleoceanography of the western equatorial Indian Ocean. In Duncan, R.A., Backman, J., Peterson, L.C., et al., *Proceedings of the Ocean Drilling Program, Scientific Results*, 115: College Station, TX (Ocean Drilling Program), 411–432. <http://dx.doi.org/10.2973/odp.proc.sr.115.157.1990>
- Munsell Color Company, Inc., 1994. *Munsell Soil Color Chart* (revised edition): Newburgh, MD (Munsell Color).
- Murray, R.W., Miller, D.J., and Kryc, K.A., 2000. *Technical Note 29: Analysis of Major and Trace Elements in Rocks, Sediments, and Interstitial Waters by Inductively Coupled Plasma–Atomic Emission Spectrometry (ICP–AES)*. Ocean Drilling Program. <http://dx.doi.org/10.2973/odp.tn.29.2000>
- Norris, R.D., Wilson, P.A., Blum, P., and the Expedition 342 Scientists, 2014. *Proceedings of the Integrated Ocean Drilling Program, 342*: College Station, TX (Integrated Ocean Drilling Program). <http://dx.doi.org/10.2204/iodp.proc.342.2014>
- Okada, H., and Bukry, D., 1980. Supplementary modification and introduction of code numbers to the low-latitude coccolith biostratigraphic zonation (Bukry, 1973; 1975). *Marine Micropaleontology*, 5:321–325. [http://dx.doi.org/10.1016/0377-8398\(80\)90016-X](http://dx.doi.org/10.1016/0377-8398(80)90016-X)
- Olsson, R.K., Hemleben, C., Berggren, W.A., and Huber, B.T. (Eds.), 1999. Atlas of Paleocene planktonic foraminifera. *Smithsonian Contributions to Paleobiology*, 85. <http://dx.doi.org/10.5479/si.00810266.85.1>
- Ouda, K., and Aubry, M.-P. (Eds.), 2003. The upper Paleocene–lower Eocene of the Upper Nile Valley: Part 1, Stratigraphy. *Micropaleontology*, 49(Supplement 1). <http://www.jstor.org/stable/i369931>
- Pearson, P.N., 1995. Planktonic foraminifer biostratigraphy and the development of pelagic caps on guyots in the Marshall Islands group. In Haggerty, J.A., Premoli Silva, I., Rack, F., and McNutt, M.K. (Eds.), *Proceedings of the Ocean Drilling Program, Scientific Results*, 144: College Station, TX (Ocean Drilling Program), 21–59. <http://dx.doi.org/10.2973/odp.proc.sr.144.013.1995>
- Pearson, P.N., Olsson, R.K., Hemleben, C., Huber, B.T., and Berggren, W.A., 2006. Atlas of Eocene planktonic foraminifera. *Special Publication - Cushman Foundation for Foraminiferal Research*, 41.
- Perch-Nielsen, K., 1985a. Cenozoic calcareous nannofossils. In Bolli, H.M., Saunders, J.B., and Perch-Nielsen, K. (Eds.), *Plankton Stratigraphy*: Cambridge, United Kingdom (Cambridge University Press), 427–554.
- Perch-Nielsen, K., 1985b. Mesozoic calcareous nannofossils. In Bolli, H.M., Saunders, J.B., and Perch-Nielsen, K. (Eds.), *Plankton Stratigraphy*: Cambridge, United Kingdom (Cambridge University Press), 329–426.
- Petrizzo, M.R., Falzoni, F., and Premoli Silva, I., 2011. Identification of the base of the lower-to-middle Campanian *Globotruncana ventricosa* Zone: comments on reliability and global correlations. *Cretaceous Research*, 32(3):387–405. <http://dx.doi.org/10.1016/j.cretres.2011.01.010>
- Premoli Silva, I., and Sliter, W.V., 1999. Cretaceous paleoceanography: evidence from planktonic foraminiferal evolution. In Barrera, E., and Johnson, C.C. (Eds.), *The Evolution of Cretaceous Ocean–Climatic System*. Special Paper - Geological Society of America, 332:301–328.
- Rider, M.H., 1996. *The Geological Interpretation of Well Logs* (2nd edition): Caithness, Scotland (Whittles Publishing).
- Robaszynski, F., and Caron, M., 1979. Atlas de foraminifères planctoniques du Cretace moyen (Mer Boreale et Tethys) (Volumes 1 and 2). *Cahiers de Micropaléontologie*.
- Robaszynski, F., and Caron, M., 1995. Foraminifères planctoniques du Crétacé: commentaire de la zonation Europe–Méditerranée. *Bulletin De La Societe Geologique De France*, 166:681–692.
- Robaszynski, F., Caron, M., Gonzales-Donoso, J.-M., Wonders, A.A.H., and the European Working Group on Planktonic Foraminifera, 1984. Atlas of Late Cretaceous globotruncanids. *Revue de Micropaleontologie*, 26(3–4):145–305.
- Roth, P.H., 1978. Cretaceous nannoplankton biostratigraphy and oceanography of the northwestern Atlantic Ocean. In Benson, W.E., Sheridan, R.E., et al., *Initial Reports of the Deep Sea Drilling Project*, 44: Washington, DC (U.S. Government Printing Office), 731–759. <http://dx.doi.org/10.2973/dsdp.proc.44.134.1978>
- Ruddiman, W.F., Cameron, D., and Clement, B.M., 1987. Sediment disturbance and correlation of offset holes drilled with the hydraulic piston corer: Leg 94. In Ruddiman, W.F., Kidd, R.B., Thomas, E., et al., *Initial Reports of the Deep Sea Drilling Project*, 94: Washington, DC (U.S. Government Printing Office), 615–634. <http://dx.doi.org/10.2973/dsdp.proc.94.111.1987>
- Schlumberger, 1989. *Log Interpretation Principles/Applications*: Houston (Schlumberger Education Services), SMP-7017.
- Schlumberger, 1994. *IPL Integrated Porosity Lithology*: Houston (Schlumberger Wireline Testing), SMP-9270.

- Scott, G.H., Bishop, S., and Burt, B.J., 1990. Guide to some Neogene Globotulids (Foraminiferida) from New Zealand. *New Zealand Geological Survey Paleontological Bulletin*, 61.
- Serra, O., 1984. *Fundamentals of Well-Log Interpretation* (Volume 1): *The Acquisition of Logging Data*. Amsterdam (Elsevier).
- Serra, O., 1986. *Fundamentals of Well-Log Interpretation* (Volume 2): *The Interpretation of Logging Data*. Amsterdam (Elsevier).
- Serra, O., 1989. *Formation MicroScanner Image Interpretation*: Houston (Schlumberger Education Services), SMP-7028.
- Shipboard Scientific Party, 1995. Explanatory notes. In Flood, R.D., Piper, D.J.W., Klaus, A., et al., *Proceedings of the Ocean Drilling Program, Initial Reports*, 155: College Station, TX (Ocean Drilling Program), 47–81. <http://dx.doi.org/10.2973/odp.proc.ir.155.104.1995>
- Shipboard Scientific Party, 2003. Explanatory notes. In Tréhu, A.M., Bohrmann, G., Rack, F.R., Torres, M.E., et al., *Proceedings of the Ocean Drilling Program, Initial Reports*, 204: College Station, TX (Ocean Drilling Program), 1–102. <http://dx.doi.org/10.2973/odp.proc.ir.204.102.2003>
- Sissingh, W. 1977. Biostratigraphy of Cretaceous calcareous nannoplankton. *Geologie en Mijnbouw*, 57:433–440.
- Spezzaferri, S., 1994. Planktonic foraminiferal biostratigraphy and taxonomy of the Oligocene and lower Miocene in the oceanic record: an overview. *Palaeontographica Italia*, 81.
- Stow, D.A.V., 1977. Late Quaternary stratigraphy and sedimentation on the Nova Scotian outer continental margin [Ph.D. dissertation]. Dalhousie University, Canada.
- Strelnikova, N.I., 1974. *Diatomei Posdnego Mela (Zapadnaya Sibiri)*. Doklady Akademii Nauk SSSR, 8.
- Tauxe, L., Tucker, P., Petersen, N.P., and Labrecque, J.L., 1983. The magnetostratigraphy of Leg 73 sediments. *Palaeogeography, Palaeoclimatology, Palaeoecology*, 42(1–2):65–90. [http://dx.doi.org/10.1016/0031-0182\(83\)90039-1](http://dx.doi.org/10.1016/0031-0182(83)90039-1)
- Toumarkine, M., and Luterbacher, H., 1985. Paleocene and Eocene planktic foraminifera. In Bolli, H.M., Saunders, J.B., and Perch-Nielsen, K. (Eds.), *Plankton Stratigraphy*: Cambridge, United Kingdom (Cambridge University Press), 87–154.
- Vasiliev, M.A., Blum, P., Chubarian, G., Olsen, R., Bennight, C., Cobine, T., Fackler, D., Hastedt, M., Houpt, D., Mateo, Z., and Vasilieva, Y.B., 2011. A new natural gamma radiation measurement system for marine sediment and rock analysis. *Journal of Applied Geophysics*, 75:455–463. <http://dx.doi.org/10.1016/j.jappgeo.2011.08.008>
- Wade, B.S., Houben, A.J.P., Quaijtaal, W., Schouten, S., Rosenthal, Y., Miller, K.G., Katz, M.E., Wright, J.D., and Brinkhuis, H., 2012. Multiproxy record of abrupt sea-surface cooling across the Eocene–Oligocene transition in the Gulf of Mexico. *Geology*, 40(2):159–162. <http://dx.doi.org/10.1130/G32577.1>
- Wade, B.S., Pearson, P.N., Berggren, W.A., and Pälike, H., 2011. Review and revision of Cenozoic tropical planktonic foraminiferal biostratigraphy and calibration to the geomagnetic polarity and astronomical time scale. *Earth-Science Reviews*, 104(1–3):111–142. <http://dx.doi.org/10.1016/j.earscirev.2010.09.003>
- Wentworth, C.K., 1922. A scale of grade and class terms for clastic sediments. *Journal of Geology*, 30(5):377–392. <http://dx.doi.org/10.1086/622910>